



저작자표시-비영리-변경금지 2.0 대한민국

이용자는 아래의 조건을 따르는 경우에 한하여 자유롭게

- 이 저작물을 복제, 배포, 전송, 전시, 공연 및 방송할 수 있습니다.

다음과 같은 조건을 따라야 합니다:



저작자표시. 귀하는 원저작자를 표시하여야 합니다.



비영리. 귀하는 이 저작물을 영리 목적으로 이용할 수 없습니다.



변경금지. 귀하는 이 저작물을 개작, 변형 또는 가공할 수 없습니다.

- 귀하는, 이 저작물의 재이용이나 배포의 경우, 이 저작물에 적용된 이용허락조건을 명확하게 나타내어야 합니다.
- 저작권자로부터 별도의 허가를 받으면 이러한 조건들은 적용되지 않습니다.

저작권법에 따른 이용자의 권리는 위의 내용에 의하여 영향을 받지 않습니다.

이것은 [이용허락규약\(Legal Code\)](#)을 이해하기 쉽게 요약한 것입니다.

[Disclaimer](#)

Doctoral Thesis

LASER SURFACE MODIFICATION FOR OPTICAL AND JOINING APPLICATIONS

Keunhee Lee

Department of Mechanical Engineering

Graduate School of UNIST

2020

LASER SURFACE MODIFICATION FOR OPTICAL AND JOINING APPLICATIONS

Keunhee Lee

Department of Mechanical Engineering

Graduate School of UNIST

LASER SURFACE MODIFICATION FOR OPTICAL AND JOINING APPLICATIONS

A thesis/dissertation
submitted to the Graduate School of UNIST
in partial fulfillment of the
requirements for the degree of
Doctor of Philosophy

Keunhee Lee

12/10/2019 of submission

Approved by



Advisor

Hyungson Ki

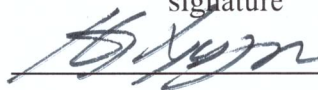
LASER SURFACE MODIFICATION FOR OPTICAL AND JOINING APPLICATIONS

Keunhee Lee

This certifies that the thesis/dissertation of Keunhee Lee is approved.

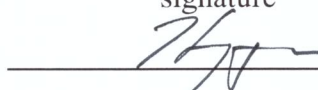
12.10. 2019 of submission

signature



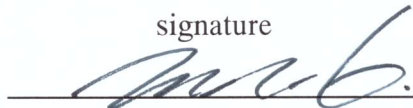
Advisor: Hyungson Ki

signature



Heungjoo Shin : Thesis Committee Member #1

signature



Jaesung Jang : Thesis Committee Member #2

signature



Jaeseon Lee : Thesis Committee Member #3

signature



Jun Choi : Thesis Committee Member #4

ABSTRACT

Recently, a variety of laser-based surface modification methods have been applied to the industry. Laser has many good characteristics of surface modification. A laser is an electromagnetic wave and has a constant beam size. Laser beam is changed to the shape of beam suitable for processing through the optics and is used in the process. The laser beam is eventually irradiated only to the desired area on the surface of the specimen, and the surface is changed by the laser beam. Using lasers, it is very useful to process only the required area and to allow fine controls. Various methods, such as hardening, cladding, micro-machining, annealing, etc., are included in laser surface modification. Recently, laser annealing process was applied to the semiconductor industry at Samsung. The application of laser surface modification technology is considered a natural stream, because it has advantages over other technologies. It is a chemically clean process, easy to control process variables and can be operated by remote control, so we can benefit a lot from using lasers. The laser surface modification is very straightforward and easy to apply in various ways. This research suggests different ways of using lasers to change the surface of material, and direction for applying changed properties.

In this dissertation, laser surface modification technology is used for optical and joining applications. The first chapter is about the motivation of this research and will describe the processes associated with laser surface modification used and the materials used and include the background of next chapters. Chapter 2 describes the graphenization of Diamond-like carbon using laser annealing and pulsed laser deposition. Diamond-like carbon film is deposited on glass using pulsed laser deposition and coated films is thermally changed through laser annealing. By measuring the transmittance and electrical conductivity of annealed films, we will identify the possibility of being used as transparent conductive films. Chapter 3 will describe how to improve the results obtained in chapter 2. The laser surface treatment used in this chapter is micromachining. The thin film on the surface is fabricated by picosecond laser and removed. Through the etching and patterning process of annealed films, we will describe how to improve electrical conductivity and transmittance. Based on the measurement results, the electrical conductivity and transmittance after patterning and etching process are predicted through a simple calculation. Chapter 4 describes laser induced periodic surface structures (LIPSS) using stainless steel as a material with femtosecond laser. This structure is feature that appears on a surface found only under certain process conditions and is associated with the electric field of the laser. This structure consists of a very small gaping pattern similar to the wavelength of a laser is used for various applications. In this chapter, the reflectance change is obtained depending on the surface geometry, including the surrounding process conditions in which LIPSS occurs. With reflectance from various process conditions, we can change the stainless-steel surface by adjusting the reflectance of the surface as desired. Chapter 5 deals with the coupling of copper materials using laser surface modification.

Copper has very high reflectance for lasers of commonly used near-infrared. Thus, the pattern is fabricated on the copper surface to reduce the reflectance so that absorption rate for laser beam can be increased. Coupling on patterned surface occur in lower energy than on the normal copper surface.

This research presents new attempts to change the optical and electrical properties of material surface and various perspectives using laser applying the optical changes of the surface to the joining applicatons.

CONTENTS

ABSTRACT.....	i
CONTENTS.....	iv
LIST OF FIGURES	vii
LIST OF TABLES	xii
NOMENCLATURE	xiii
I. INTRODUCTION	1
1.1. Motivation.....	1
1.2.1. Graphene	3
1.2.1.1. Current states of study of graphene formation by laser processing.....	3
1.2.1.2. Analysis of graphene	4
1.2.1.3. Diamond-like carbon (DLC)	5
1.2.1.4. Laser annealing.....	6
1.2.2. Laser induced Periodic Surface Structure (LIPSS).....	6
1.2.2.1. Current state of LIPSS formation	8
1.2.2.2. Lack of studies on LIPSS	11
II. TANSSPARENT CONDUCTIVE FILMS WITH CONTROLLABLE SHEET RESISTANCE ON GLASS SUBSTRATES BY LASER ANNELING OF DIAMOND-LIKE CARBON FILMS	12
2.1. Introduction.....	12
2.2. High speed fabrication (1 m/s) of line-shape transparent conductive films using a circular laser beam.....	14
2.3. Large-scale laser fabrication using a line beam (beam width : 15 mm)	18
2.4. Conclusion	19

III. OPTIMIZATION OF TRANSPARENT CONDUCTIVE FILMS USING PICOSECOND LASER PATTERNING AND ETCHING	20
3.1. Introduction.....	20
3.2. Fabrication of optical transparent conductive films for patterning and doping	21
3.3. Finding optical patterning and doping conditions.....	25
3.4. Prediction model for sheet resistance and transparency after patterning and doping	28
3.5. Experimental verification.....	34
3.6. Conclusion	38
IV. FEMTOSECOND LAER PATTERNING BASED ON THE CONTROL OF SURFACE REFLECTANCE	39
4.1. Introduction.....	39
4.2. Experimental setup.....	40
4.3. Result and discussion	42
4.4. Conclusions.....	52
V. ENHANCED COUPLING EFFICIENCY IN LASER WELDING OF PURE COPPER WITH CHANGES OF SURFACE MODIFICATION AND REFLECTANCE BY FEMTOSECOND LASER MICROMACHINING	53
5.1. Introduction.....	53
5.2. Experimental setup.....	55
5.3. Results and discussion	57
5.3.1. Reduction of reflectance of copper surface.....	57
5.3.2. Welding of copper.....	60
5.4. Conclusions.....	70

VI. CONCLUSIONS AND FUTURE WORK	71
6.1. Conclusions.....	71
6.2. Future work.....	72
REFERENCES	73
ACKNOWLEDGEMENTS	80

LIST OF FIGURES

Figure 1. Raman spectrum of graphene and graphite [7].....	5
Figure 2. phase diagram for amorphous carbon [8].....	6
Figure 3. Laser annealing process.....	6
Figure 4. Fabrication of line-shaped transparent conductive films by laser annealing of DLC films with a circular top-hat beam (beam diameter 200 μm , laser power 110 W, scanning speed 1 m/s). (a) Schematic drawing of the overall experimental procedure for fabricating line-shaped transparent conductive films (b) Deposited line-shaped DLC patterns on a borosilicate glass substrate. Film thickness and width are 510 nm and 140 μm , respectively. (c) Optical microscope image of a deposited line-shaped DLC film on glass. (d) Optical microscope image of the top surface of a laser-annealed film (e) Optical microscope image of the underside of the film obtained by setting the image focal plane at the bottom of the annealed specimen shown in Figure 4d. The horizontal blue line located below the specimen shows that the DLC film became transparent (f,g) XPS results of the DLC film (shown in Figure 4c) for C 1s and O 1s. (h) Raman spectrum of the transformed film measured at the location shown in Figure 4d (i,j) XPS results of the transformed film (shown in Figure 4d and e) for C 1s and O 1s. (k) Transmittance versus wavelength measured at the location shown in Figure 4d.	13
Figure 5. Controllable sheet resistance and transparency (beam diameter: 200 μm). (a) Sheet resistance and transmittance (at 550 nm) versus $I_0 t_i^{1/2}$ for seven different film thicknesses, where I_0 is laser intensity and t_i is laser interaction time (b) Relationship between sheet resistance and transmittance. The black solid line shows the Beer-Lambert law. (c, d) Effect of laser power on Raman spectrum and transmittance for 510 nm thick DLC films that were annealed at 1 m/s. Red lines show the result showcased in Figure 4.....	16
Figure 6. Fabrication of a large-scale transparent conductive film with a 15 mm wide line beam (laser power 1830 W, scanning speed 75 mm/s). (a) Schematic drawing of the overall experimental procedure for fabricating a large-area transparent conductive film. The film size is 15 mm \times 15 mm. (b) Deposited DLC film on a fused silica substrate. The film is almost black and non-conducting. (c) Laser-annealed film on a fused silica glass substrate. The film is transparent and conducting. (d) Transmittance versus wavelength.	19
Figure 7. A schematic figure showing the overall procedure used in this study. A DLC film deposited on a fused silica glass substrate was annealed by a line laser beam and transformed into a transparent conductive film. A picosecond laser was used to fabricate patterns on the film surface to increase the	

optical transparency and a chemical doping process was employed to increase the electrical conductivity of the film. 22

Figure 8. (a) Raman spectrum of a DLC film deposited at room temperature (before annealing), (b) Raman spectrum of a DLC film deposited at 900 °C (before annealing), (c) Measured sheet resistance and optical transparency (@ 550 nm) of annealed DLC films. 22

Figure 9. OM images (top row), SEM images (middle row), and Raman spectra (bottom row) of transparent conductive films annealed with 460, 545, 650, 770, 920 W, from left to right, respectively (annealing speed: 0.1 m/s). Corresponding sheet resistance and transmittance values are shown together. (Room-temperature deposited DLC films were used.). 24

Figure 10. Sheet resistance vs. film thickness 25

Figure 11. (a) OM and (b) SEM images of the line patterns fabricated on the transparent conductive films (shown in Fig. 3(c)) using 25 different patterning conditions. 26

Figure 12. (a) From the line patterning result shown in Fig. 5, a narrowed-down process window (red box) was identified and five more experiments were additionally conducted (small white circles). (b) Patterning results corresponding to the nine conditions. The result shown in the blue box was found to be the optimal patterning condition. (c) Magnified image of the optimal line pattern. 27

Figure 13. % reduction of sheet resistance after doping by (a) HNO₃ and (b) HCl. 27

Figure 14. (a, b) Schematic drawings of the films with circular and square patterns, (c, d) Unit cells identified from the left figures. 29

Figure 15. (a) Schematic drawings showing how the electrical resistance of a unit cell (R_{unit}) was calculated for circular and square patterns by breaking down the unit cell into smaller regions ($R_{\text{unit}} = R_1 + R_2 + R_1$) (b) Electrical circuit representation of the entire film constructed by connecting the electrical resistance of a unit cell in series and in parallel. 30

Figure 16. Prediction maps for sheet resistance and optical transparency of transparent conductive films after patterning and doping for (a) circular patterns and (b) square patterns 33

Figure 17. Prediction maps for the figure-of-merit of transparent conductive films after patterning and doping for (a) circular patterns and (b) square patterns. 34

Figure 18. (a) Optical microscope images of the films at different stages. The left black figure is the

image of a DLC film, the middle ones are annealed films ($\sim 25\%$ transparency), and the right ones are the films after laser patterning and chemical doping. (b) Transmission spectra of the films at different stages. (c) Films at the three corresponding stages were placed on a paper with printed colored lines, showing that the transparency improved after laser annealing and laser patterning. 36

Figure 19. Schematic view of the experimental setup 41

Figure 20. SEM images of the fabricated patterns arranged in terms of laser fluence (vertical axis) and scanning speed (horizontal axis). 42

Figure 21. Magnified images of the patterns shown in Figure 20(a)–(d). From (a) to (d), the scanning speed changes from 5.53 to 1.83 to 0.61 and to 0.2 mm/s, all at the same laser fluence of 0.963 cm^2 . 43

Figure 22. Contour lines showing the surface reflectance (at 550 nm) of the fabricated surfaces..... 45

Figure 23. Change in reflectance spectra according to (a) scanning speed and (b) laser fluence. 46

Figure 24. (a) Original design of the multi-faceted ball (b) A picture of a multi-faceted ball fabricated on stainless steel by implementing 22 surface reflectance values. The diameter of the ball is 20 mm. It is noteworthy that in part (a), the reflectance level is shown based on a grayscale, and the gray level cannot accurately represent the actual reflectance. 47

Figure 25. Pictures of multi-faceted balls fabricated under different shielding environments. 48

Figure 26. (Top row) SEM images showing the surface morphology at the locations indicated by the red points in Figure 25, obtained with, from left to right, no shield gas, nitrogen, argon, and helium shielding gases. (Middle row) Images of a single line fabricated under each shielding condition shown above. (Bottom row) Magnified images of the regions inside the red boxes above. (All results were obtained with the same condition of 5.09 J/cm^2 and 5.53 mm/s .) 49

Figure 27. SEM images of generated structures, surface colors of the patterned surfaces, and the corresponding reflectance values at 550 nm. All patterns were fabricated using a laser fluence of 5.09 J/cm^2 and four different scanning speeds (5.53 , 1.83 , 0.61 , and 0.2 mm/s). From top to bottom, air, nitrogen, argon, and helium shield gases were used 50

Figure 28. XPS spectra ((a) Fe 2p and (b) O 1s) of the patterned surfaces fabricated under four different shield gas environments. (conditions: 5.09 J/cm^2 and 5.53 mm/s). 51

Figure 29. Pictures of multi-faceted balls viewed from different viewing angles for each shield gas

condition (air, nitrogen, argon, and helium). For each shielding condition, the left and right figures were images obtained from 40° to the left and right sides, respectively..... 52

Figure 30. Schematic view of experimental setup. (a) femtosecond laser patterning process for the fabrication of the copper surface with the low reflectance. (b) observation of the surface during the welding process using a high speed camera and the welding process starting from the surface obtained in (a). 55

Figure 31. SEM images of fabricated copper surface. The color of the boxes indicates the classification of the surface structure. Structures with red checks are the conditions used in the experiment. 57

Figure 32. (a) SEM images of patterned area (b) color images of patterns according to reflectance. .. 59

Figure 33. High speed camera images according to processing conditions..... 60

Figure 34. High-speed camera images of (a) a patterned surface and (b) a surface after passing through patterned area for seven reflectance levels (3, 5, 7, 11, 15, 21, 32 and 47%) at 1800 W and 150 mm/s (c) Relationship between reflectance and dimensions ((c) width, (d) length and (e) area) of melt pool in (a) and (b)..... 61

Figure 35. Variation of bead width according to reflectance of pattern. (P = 1800W, v = 150 mm/s).. 63

Figure 36. Top and bottom view of welded copper surface using 3% of reflectance pattern and power of 1800 W and scanning speed of (a) 150 mm/s, (b) 200 mm/s and (c) 300 mm/s 64

Figure 37. High-speed camera images taken at intervals of 0.4 ms from the area where melt ejection occurs..... 64

Figure 38. (a) cross-section image of the results using different reflectance values (3%, 21%, and 47%) under the same process conditions (1800 W, 200 mm/s) (b) cross-section images at different positions (1 cm, 2 cm, and 3 cm) under the same reflectance (47%) and process conditions (1800W, 200 mm/s) 65

Figure 39. (a) graphs showing measurements of (a-1) bead width, (a-2) penetration depth and (a-3) area over distance from pattern. (b) graphs showing changes in (b-1) bead width, (b-2) penetration depth, (b-3) area as the reflectance of patterns changes. 67

Figure 40. . A Top view of results using welding process conditions of 1800 W and 200 mm / s. (a) welding results obtained by fabricating patterns with reflectance of 3%, 21% and 47% only at the

beginning of the weld. (b) welding results obtained by machining patterns with reflectances of 3%, 21%,
and 47% at 2 cm intervals..... 69

LIST OF TABLES

Table 1. Predicted and measured properties of the fabricated films (units: $R_{s,f}$ (Ω/sq), T_f (%)) 37

NOMENCLATURE

Chapter I

Λ : Period

Λ_{SPP} : Period of surface plasmon polariton

Λ_{LSFL} : Period of low specific frequency laser induced periodic surface structure

Λ_{HSFL} : Period of high specific frequency laser induced periodic surface structure

ϵ : Permittivity

λ : Wavelength of laser

n : Refractive index

Chapter II

R_s : Sheet resistance

R : Electrical resistance

W : Width of the film

L : Length of the film

I_0 : Intensity of laser

t_i : Interaction time

I_D : Intensity of D peak (Raman spectrum)

I_G : Intensity of G peak (Raman spectrum)

I_{2D} : Intensity of 2D peak (Raman spectrum)

L_a : Domain size

λ : Wavelength of laser

Chapter III

R_a : Roughness of the film

T : Transmittance

P : Laser power

r_A : Ratio of the ablated pattern area to the unit cell area

D : Diameter of a circular pattern

l : One-side length of a square pattern

d : Horizontal and vertical distance between patterns

T_0 : Original transparency

T_f : Effective film transparency with patterns

R_{unit} : Electrical resistance of a unit cell

R_1, R_2 : Electrical resistance of smaller regions in the unit cell

$R_{s,0}$: Sheet resistance of the original transparent conductive film

R_f : Electrical resistance of the entire patterned film

W_f : Width of the whole film

L_f : Length of the whole film

$R_{s,f}$: Effective sheet resistance of the whole film

π : the ratio of the circumference of a circle to its diameter

a, b, c : fitting coefficients

σ_{DC} : DC conductivity

σ_{op} : Optical conductivity

Z_0 : the impedance of free space

Chapter IV

Φ : Fluence

v : Scanning speed

R : Reflectance

I. INTRODUCTION

1.1. Motivation

Recently, lasers have been applied to various industries in a future-oriented way. The biggest advantage of lasers is that they can irradiate energy with a high power in a very small area. A variety of machining techniques have been introduced in recent years using lasers. Lasers have continuous waves and pulsed lasers, both of which utilize their respective strengths and are used in other areas. Continuous wave laser is mainly used for thermal change of material, and the areas used mainly are welding and annealing process. Pulsed lasers have pulses with some repetition rate. Currently, femtosecond lasers are used mainly, and many studies are underway. These ultrafast lasers have the advantage of minimizing thermal effects around the areas examined because of their very short interaction with the material. Ultrafast lasers are mainly used in the micro-machining field.

Our laboratory has femtosecond laser, picosecond laser, and fiber laser. Using these three types of lasers, various experiment could be used to study many subjects. Although these lasers can be applied to many applications, many experiments have been carried out especially with ultrafast lasers. Ultrafast lasers can be applied in many areas. The laser can vary the properties of the beam by using optics. First, laser can be used for small-scale processes by making the beam size in units of μm using objective lens. Since the peak power is very high due to short pulse duration, it is easy to ablate the materials. For these reasons, pulsed laser is mainly used for micro-machining. Laser micro-machining includes patterning, cutting, and drilling etc. The ultrafast lasers in the laboratory is connected to the computer and works with the stage and is designed to allow processing in various ways through several optics. We tried fabricating various materials and got results that could feel the benefits of ultrafast laser. Coating was also possible using the application of Pulsed laser. This coating process is called Pulsed Laser Position (PLD). Plasma plume occurs when ablation occurs on the surface of a substance in a vacuum. This plume is attached to the surface of the substrate to create a thin film over the surface of the substrate. If a substance can be ablation with a laser, the thin film of the desired substance can be created on the substrate. As such, most of the processes using Pulsed laser address the phenomena that occur on the surface of an object. Currently, various electronic devices such as smart phones and tablet PCs are being developed in the industry. These electronic devices require many parts and technologies, but the technology for displays is very important. Recently, the attention of flexible displays from Samsung shows how important these technologies are. Display has several complex technologies. For example, there are a coating of a clear electrode and a patterning of electrodes. Laser can be used to coat and pattern this material. However, many of these areas are going on in chemical ways, which, if carried out using lasers, may have a large initial cost, but may have many advantages due to the significant

increase in process efficiency. Therefore, we have studied how lasers can be joined into optical areas such as transparent electrodes.

Firstly, the research was conducted to make transparent electrodes. Graphene is drawing attention as a new material that can replace ITOs that are commonly used as transparent electrodes. Graphene is a substance made of only carbon. The amorphous carbon was coated on the glass using the PLD system. We tried to change this coating to graphene by heating it with a laser. Graphene with carbon coating is covered in Chapter 2, which refers to a paper written by the author, published in *Acta materialia* [1].

Secondly, studies have been conducted on how to improve the patterning and properties of transparent electrodes produced. Patterning was carried out using a pulsed laser. Patterning the results of the first topic improved the transmittance of films and through the doping process, we improved the electrical conductivity was improved. The optimization of the film is covered in Chapter 3, referenced by the author's paper, which was published in *Applied Surface Science* [2].

The third was the study of Laser Induced Periodic Surface Structure (LIPSS). If the preceding topics were related to transmittance, in this topic it was about reflectance. Using a pulsed laser, the variation in the reflectivity of the shape of the surface was considered under various process conditions. Among surface features, LIPSS was also observed. Differences in reflectance caused differences in contrast between surface shapes, which were used to obtain drawings on the surface of a substance. LIPSS-based surface reflectance control is discussed in Chapter 4, referring to the author's paper, which was published in *Applied Surface Science* [3].

The Fourth is the combination of the reflectivity covered in the third state and the new subject, welding. Copper has been chosen as the subject matter for this subject. Copper is a highly reflective material. Reflections on laser beams are also high, making it difficult to weld or process materials. To solve this problem, the third topic, the change in reflectivity according to surface geometry, was used to reduce the surface reflectivity of copper. We have identified how the welding process is different by the reflectivity lowered by the patterns formed on the surface. This topic is currently being prepared for paper submission.

1.2. Background

1.2.1. Graphene

Graphene is one of the isotopes of carbon and is a two-dimensional structure in which carbon atoms converge. Each carbon atom has a hexagonal grid and appears to be located at the tip of the hexagon. This shape is also called honeycomb structure. A thin film consisting of the thickness of one atom and 0.2 nm in thickness, it is incredibly thin and has high physical and chemical stability stones. The reason graphene is getting attention is because of the following outstanding characteristics. Graphene has a very high peak electronic mobility of 200,000 cm²/Vs, a high thermal conductivity of ~5000 W/m, K, and a young coefficient of ~1.0 Tpa. Also, since it consists of one layer, the absorption to visible light was very low, resulting in a transmission rate of 97.7% for light with a wavelength of 550 nm. It is 100 times better than copper and can move electrons 100 times faster than single-crystal silicon, which is usually used for semiconductors. Its strength is 200 times stronger than steel, has twice as much thermal conductivity as diamonds, and its elasticity is excellent. In addition, graphene does not lose its electrical properties even when stretched or bent. With this characteristic, graphene is becoming the next-generation new material. Graphene is applied to various industries such as display, secondary battery, solar cell, etc. as it is the most outstanding new material among existing materials such as strength, thermal conductivity, and electronic mobility. It is very suitable for use as a transparent electrode material due to its transparent and high electrical conductivity. Currently, technology has been developed to make large-scale graphene films that can be used as transparent electrodes. However, the transfer process is essential and there is a reduction in the efficiency of the process. Although it is more vulnerable in terms of industrial and mass production compared to current ITOs, it will be an excellent replacement if it is addressed.

1.2.1.1. Current states of study of graphene formation by laser processing

Qian et al got graphene through the laser exfoliation of highly ordered pyrolytic graphite (HOPG) [4]. The PLD system was used, and the laser was irradiated on the HOPG and graphene coated on the silicon substrate. This obtained coating was found to consist of several layers of graphene by Raman analysis, SEM and TEM analysis. Yu et al obtained graphene from silicon carbide (SiC). Using SiC as q-switcher, the heat during switching caused graphene to form on the SiC surface. The formed graphene consisted of 10 to 40 layers and had an even lower absorption rate and low dependence of wavelength.

Park et al. formed a graphene using laser-induced physical vapor deposition (LCVD) [5]. . When the thin nickel film was irradiated with the laser in CH₄ and H₂ environments, graphene was formed on nickel foil. Since the formed graphene existed on nickel foil, the transferring process to insulating

substrate was necessary to be utilized in practical application. The transferred graphene was either single layer or multiple layers. The number of layers of graphene was very sensitive to scan speed, and the slower the scan speed was, the more layers of graphene were found to form. Fan et al. described the technique in which graphene patterns were directly formed on SiO₂/Si substrate through single-step LCVD process [6]. Firstly, they coated a thin layer of nickel (400 nm) on the SiO₂/Si substrate. And under the environmental conditions of CH₄ and H₂, lasers were irradiated on the nickel film and graphene formed on the thin nickel film. The remaining nickel layer was removed by nickel etchant and only the graphene remained on the SiO₂/Si substrate. The single layer of graphene was dominant in the central part of the irradiated area, and the more towards the edge, the more layers were found to increase.

Xiong et al. formed a graphene pattern directly on the insulating substrate and this method was called laser direct writing [7]. First, they deposited Ni/C thin film on top of glass substrate, then irradiating laser to form graphene. Multi-layer graphene was formed at 800 nm beam size and 500 μm/s speed using femtosecond laser (120 fs, 100 MHz) in ambient environment at room temperature. Remaining Ni/C film without laser irradiation needed to be removed. The generated pattern has electrical conductivity of 205 ohm/sq and transmittance at 550 nm of 94.3%. Wei et al introduced the method of forming graphene on silicon substrate [8]. . They used poly (methyl methacrylate) (PMMA) as a source of carbon to make graphene. First, they coated PMMA on top of silicon wafers and covered them with quartz wafers. The reason why it is covered with quartz wafers is to prevent carbon atoms from evaporating and dispersing into the atmosphere when the laser is irradiated, so that the concentration of carbon is kept high. Laser beams were focused on silicon wafers and irradiated under high purity nitrogen gas conditions. As a result, it was confirmed through Raman analysis that two to three layers of graphene were produced when laser was irradiated for five minutes. If irradiated longer than five minutes, the number of layers of graphene increased, forming at least four layers of graphene. Wei et al described in 2013 another way how to produce graphene directly on the quartz substrate [9]. . A photoresist S-1805 was spin coated on the quartz substrate, then another quartz substrate was placed on the top surface. The laser was irradiated by focusing on the photoresist located between two quartz substrates. The irradiated laser caused the temperature to rise and carbon atoms extracted from photoresist. Extracted carbon atoms formed graphene structure. Graphene had fewer layer as the irradiation time was longer, and after five minutes of irradiation, the monolayer of graphene was obtained.

1.2.1.2. Analysis of graphene

Graphene is a thin layer of carbon. The thickness of graphene is only a few nanometers, so it is very difficult to measure. At present, TEM is used to determine the number of layers of graphene and

make accurate measurements. However, the TEM measurement requires the preparation of the necessary specimens. Raman measurements are generally used because the results may be unsuitable for TEM measurements. Currently, many studies have conducted graphene analysis using Raman spectroscopy. Thus, analysis using Raman spectroscopy is also a very reliable result. Raman measurements of typical carbon materials, such as graphite and graphene, give the peaks shown in Figure 1. Representative peaks are D, G, and 2D. Graphene structure can be analyzed using the ratio of these peaks. The ratio of D-Peak and G-Peak can identify defects in the structure, and the ratio of 2D Peak and G-Peak can identify the number of layers of graphene.

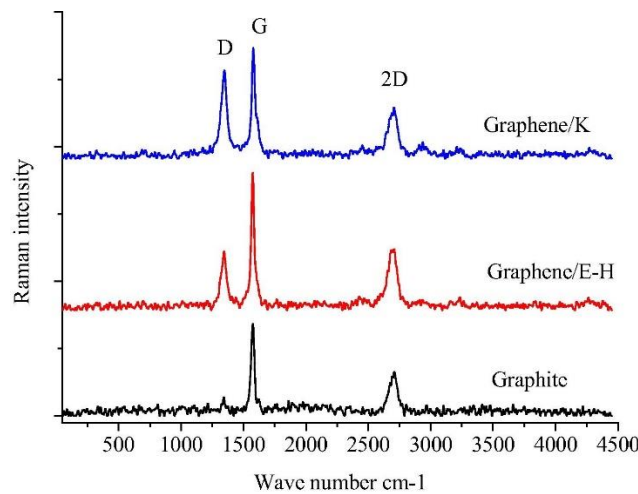


Figure 1. Raman spectrum of graphene and graphite [10]

1.2.1.3. Diamond-like carbon (DLC)

Diamond like carbon (DLC) can be deposited using pulsed laser deposition technique. In Figure 2, DLC exists in a variety of forms, of which the ideal material called tetrahedral amorphous carbon (ta-C) is the hardest and consists purely of sp^3 coupled carbon atoms. However, the actual DLC contains at least a little sp^2 binding. The deposition technique using pulsed laser is to ablate graphite targets in a vacuum chamber. In vacuum state, when laser is irradiated on target, target material is rapidly evaporated, ionized and plasma plume is formed by high photon energy. This plasma plume reaches the substrate with high kinetic energy and becomes deposition. In general, the heat treatment process is carried out in order to absorb the deposited DLC film more well into the substrate. However, during this heat treatment, some sp^3 bonds will be converted into sp^2 bonds, which will reduce the material properties of the DLC. We decided to use this point to add laser annealing method to the existing DLC film deposition method and study how to produce graphene on the substrate without going through the transferring process directly on the substrate.

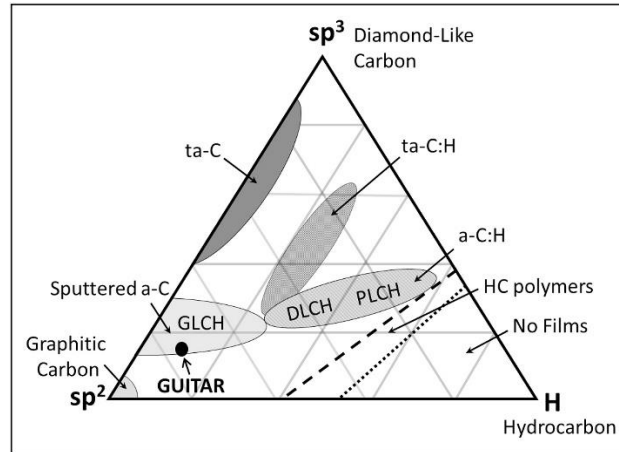


Figure 2. phase diagram for amorphous carbon [11]

1.2.1.4. Laser annealing

Annealing is a process in which the surface is heated and cooled to deform the material surface. Laser annealing refers to annealing performed using a laser, which can be heated quickly to self-cooled, and the process can be carried out in the atmosphere. When using a Forge method to heat the substrate, the hot substrate takes a long time to cool and the heat of the substrate affects the surface. However, because laser annealing quickly heats and cools only the surface, an efficient process can be made.

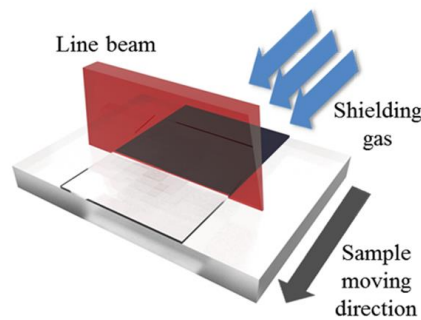


Figure 3. Laser annealing process

1.2.2. Laser induced Periodic Surface Structure (LIPSS)

LIPSS is shown through the complex physical processes of inter and intrapulse. After the laser is absorbed by an object, the energy is transferred to the solid grid system by thermal fluid and by mechanical or chemical effects. This phenomenon can affect periodic surface relief through ablation of materials. Due to the reaction between pulses and various mechanisms, the theory of LIPSS is not

currently available and many aspects are still debatable.

LIPSS was first discovered by Birnbaum in 1965. Using the ruby laser beam, the laser was irradiated on the surface of the polished Germanium to create parallel grooves. LIPSS is largely divided into two types: low specific frequency LIPSS (LSFL) and high specific frequency LIPSS (HSFL). LSFLs generally appear mainly on semiconductors and metals in a direction perpendicular to the incident laser beam polarization, and LIPSS period ($\Lambda/2 < \Lambda < \lambda$) with values near the incident wavelength. LSFL is divided into two parts in detail. LSFL, whose LIPSS period is approximately similar to incident wavelengths, is produced by the interaction of electromagnetic waves scattered on the rough surface with the laser beam and Surface Plasmon Polaritons (SPP). LIPSS literature often states that SPP wavelengths are directly related to the LSFL period ($\Lambda_{SPP} = \Lambda_{LSFL}$). The period of SPP in the standard surface plasmon model of the metal-air interface against vertical incident light can be represented as $\Lambda_{LSFL} = \Lambda_{SPP} = \lambda \times \text{Re}[(+1)/\epsilon^3]$ with respect to permittivity, ϵ . When the number of laser pulses is small, the period of LSFL can coincide with the period of SPP because the depth of the LIPSS on the surface is shallow. However, once deep LIPSSs are formed, it is difficult to simply express the SPP period as above. Multi-pulse feedback phenomena also have a significant effect on LSFL formation, and standard surface plasmon models should always be carefully checked and applied. The second LSFL type is observed in dielectrics. These LSFL structures are generally parallel to the polarization of incident laser beam, and the LSFL period relates to the refractive index of the dielectric material, $\Lambda_{LSFL} = \lambda/n$ ($n = \epsilon^{1/2}$). This structure is related to Radiation Remnant (RR) in Transparent Materials by Sipe theory.

In the case of HSFL having a period very small than the wavelength of incident laser, usually appearing in fluence near threshold, and mostly produced in short pulsation of femtosecond and picosecond. The HSFL direction is shown both vertically and horizontally in the direction of incident laser polarization, depending on the substance. HSFL is divided into two types depending on the depth of LIPSS curve. The first type is usually found in dielectrics and semiconductors, with the formation of narrow LIPSSs of several tens of nanometers in width. Initially, it starts with individual nano-cracks, and LIPSS can reach a depth of hundreds of nanometers. In this first type, the depth-period ratio (A) will have a value greater than 1. Some authors call these nanostructures deep-subwavelength leaves. And in the case of translucent materials, LIPSS represents a period of $\Lambda_{LSFL} = \lambda/2n$.

On the other hand, the gravitational pull of the second type LIPSS is smaller than 1 with a shallow ten of nanometers of depth than the first type, with periods close to the range of 100 nm or less. This shallow HSFL is usually observed on metal surfaces such as Ti, Ni and surface oxidation, or recomposals of shallow melt layers induced by lasers are involved in its formation. But at present the two

types of HSFL are not distinguished in the literature and the origins of HSFL are debatable. HSFL is formed mainly by irradiation of ultrafast laser pulses and is large in relation to the direction of linear laser polarization and has a low limit periods ,50-100 nm. These three features place the preference of the super-fast energy deposition mechanism on the sample surface as the source of HSFL. The lower limit is determined by the heat diffusion effect, and too small-scale part is removed during the transfer of energy from the excited electrons to the surrounding solid grid. HSLF is not adequately explained by Sipe Theory for the theoretical explanation of the absorbed light energy.

LIPSS can be formed on the surface by a single laser pulse but a distinct and well-aligned LIPSS is generally formed by multiple laser pulses. When a laser beam is firstly irradiated on the surface of materials, the first pulse produces a rough surface that enables energy coupling to the next laser pulse. The specific frequency of a roughness allows better absorption of radiation. During repeated exposures, specific spatial frequency is required to form grids such as LIPSS patterns through positive feedback. In the formation of LIPSS, which may already be caused by a single laser pulse or multiple pulses, the feedback process is as follows. The Intrapulse effects include temporary changes in the optical properties of solids, stimuli in surface-scattered electromagnetic waves (SEW), nonlinear effects, or spatial non-bacterial absorption.

1.2.2.1. Current state of LIPSS formation

In a paper written in 2008, Vorobyev et al. used fs-laser (65 fs, 800 nm) to form LIPSS on the aluminum surface to describe the change in the optical properties of the metal [12]. Laser was examined on the aluminum surface using X-Y stage, and the result was found to show a variety of colors. In case of gold, surface structures of nanostructures and micro-scale appeared, although not LIPSS on the surface, when scan was carried out using a flux of 0.16 J/cm², scanning speed of 1 mm/s and a retraction rate of 100 kHz. The surface was always confirmed to be gold, with no change in color depending on the angle. This is thought to be due to the shape of the irregular surface and the size of the periodic part on a micro-scale. The surface of aluminum produced in this experiment was formed with LIPSS having periods close to ~540 nm and the color changed according to the angle. And they describe that the period of LIPSS is controlled by laser's angle of incidence, wavelength, and real part of the effective reaction index. In addition, In 2008, Vorobyev et al. described the results of their experiments on the graphite phenomenon of Platinum using femtosecond lasers (800 nm, 65 fs, 1 kHz) [13]. Using a fluence of 8.1 J/cm². The results of the experiment confirmed that the microstructure with a period of 100 μm was formed, and that irregular nanostructure was formed on its surface. Measurement of the reflections on this surface showed that 50-80% of the reflections from the machining field were less than 5% in the overall wavelength range after laser irradiation. It was also confirmed that the measurement of

absorptance increases by up to 95%, which is consistent with the results of the reflectance measurement.

Dusser et al described LIPSS formation and color change using fs-laser (150 fs, 800 nm, 5 kHz) is described on the surface of the stainless steel [14]. It also describes how the color of the LIPSS structure varies depending on pulse energy, processing speed, direction of polarization and angle of observation, and how to measure that color. Shammim Ahsan el al. controlled the irradiation conditions of the femtosecond laser beam (786.5 nm, 183 fs) to indicate color on the stainless-steel surface [15]. The monochromatic and multicolored stainless-steel surfaces were obtained by Micro/nano grating and microhole. The multi-colored stainless-steel surface on the sample surface showed different colors depending on the angle of incidence and indicated the dependence of metal colors on the angle of incidence. Korolkov et al. formed nanostructures (LIPSS) in Ni/Cu foils using femtosecond laser [16]. In this paper, the term femtosecond laser nanostructuring (FLN) was used instead of LIPSS. A femtosecond laser (744 nm, 110 fs, 10 Hz) was used and Ni/Cu bilayer foils were used as a material. Ni/Cu foils used here were deposited using CVD. An experiment was conducted in the energy density area of 50-300 mJ in various mediums (air, distilled water, ethanol, benzene) using linearly polarized beams to obtain nanostructures. The reason for the formation of FLN in a liquid was to create a two-dimensional structure that is not affected by polarization. As a result, nanostructure with a period of 400-450 nm was obtained in the air, and nanostructure with a period of 370-390 nm in the water. But in other conditions besides air, it was not linear grating but irregular nanostructure. In this paper, we tested whether an anti-reflective coating can be created on a polymer using FLN of these metals. For Anti-reflective coating, the period of grating should not exceed half of the incident wavelength, so they thought that using the 400-450 nm period obtained from this paper and they produce an anti-reflective coating in the near-IR area. Yao et al. formed LIPSS on the surface of the stainless steel 301L using femtosecond laser (800 nm, 90 fs, 1 kHz) [17]. After finding the optimal LIPSS shape condition by adjusting the laser irradiation conditions, we applied different patterns and changed the angle of the incident light to observe the color change of the stainless-steel surface. There was certainly no mention of the period and depth of LIPSS, and only the results of experiments using optimal conditions are described. A. A. Ionin et al. used femtosecond lasers (744 nm, 100 fs, 10 Hz) to make color making on top of smooth silicon wafers (Al, Cu, Ti) [18]. For Si, at the process conditions of 0.27 J/cm² and 9-13 pulse counts, the p-polarized beam was joined at 15 degrees to obtain the diffractive surface nanorelief. The LIPSS's period was about 970 nm, slightly larger than the incident laser wavelength. This shows that the period has increased more than the conditions when vertically joining the company. The experimental results confirmed that, in the case of silicon wafers, the optimum LIPSS is formed when the flux is in the range of 0.2 to 0.4 J/cm². G. Li et al. used femtosecond laser (120 fs, 800 nm, 1 kHz) to present color to aluminum [19]. Under the laser conditions, the temperature of 5.1 mJ/cm² was tested with a pulse overlap -7%, 33%, 93%, and 99% using 50 μm of beam diameter. Depending on each

condition, gold, white, gray, and black colors were obtained. Zhigui Ou et al. formed LIPSS on top of Pure Cu (99.95%) using femtosecond laser (800 nm, 1 kHz, 35 fs) to generate color changing according to angle [20]. In this paper, there was a reference to the change of LIPSS period according to the conditions of the laser process. As the peak flux increased, it was stated that the LIPSS period decreased, and when we looked at the SEM photography, only an uneven portion of the period was measured by the measuring instrument even under the conditions in which LIPSS was formed. Guoqiang et al. experimented on the change of LIPSS period with wavelength over the surface of the stainless steel by using femtosecond laser (240-2600 nm, 104 fs, 1 kHz) and color change according to polarizing direction, incident light, and reflective light [21]. The irradiated laser wavelength and LIPSS period are proportional to the linear relationship, and the incident light and reflective light are adjusted to show different colors.

In 2014, Long et al. formed a colorless, hydrophobic LIPSS on the Copper (99.99%) surface, using picosecond laser (1064 nm, 10 ps, 203.6 kHz) [22]. The formation of LIPSS was observed according to the number of pulses and the fluence, and it was verified that LIPSS was formed under certain conditions ($N = 509$, $F = 0.43\text{J}/\text{cm}^2$), and the contact angles were measured for hydrophobic testing. Calvani et al. used LIPSS by femtosecond laser (800 nm, 3 mJ, 100 fs) horizontally polarized at high vacuum chamber ($<10^{-7}$ mbar) to increase diamond absorptance in the range of visible light and infrared wavelengths. The horizontal polarized laser beam focused vertically on the diamond surface and the diamond target was moved using an X-Y stage along two directions on the optical axis [23]. The period of LIPSS that was formed this way was much smaller than the wavelength of the laser used at 170 nm. The spectral photometry in the 200-2000 nm wavelength range showed a significant increase in visible light and infrared absorption over 80% compared to less than 40% of untreated samples. Granados et al. formed LIPSS using femtosecond laser (130 fs, 400 nm, 1 kHz) on the diamond surface, and recognized the photonic properties of this structure through simulation and described their usability potential [24]. Various LIPSS structures were tried to identify the different LIPSS structures on the diamond surface using the laser process conditions (fluence). The area where LIPSS of type LSFL was generated was the flow rate in the range of 2 to 6 J/cm^2 and the scan rate between 100 and 300 $\mu\text{m}/\text{s}$, where the measured period of the structure was 400 nm. At 100 $\mu\text{m}/\text{s}$ scanning speed the HSFL structure appeared and morphological irregularities appeared, degrading the optical quality of the structure. For high fluence exceeding 6 J/cm^2 , strong ablation occurred, with HSFL structure accounting for the majority of the area. It has been shown that the total number of photons colliding at a specific location on the diamond surface to create a high quality LSFL structure remains fairly constant in the range of 2 to 6 J/cm^2 . The photon characteristics of this generated structure and its potential as an anti-reflection coating of Raman laser are described. Hohm et al. investigated 5 to 10 NIR femtosecond pulse sequences to confirm that LIPSS is formed under atmospheric conditions on the surface of silica [25].

When 10 pulses were investigated, LSFL with a period between 460 and 900 nm in silica and a direction parallel to the laser beam polarization was observed at a flux of not less than 6 J/cm². At 6 J/cm² and below, HSFL with a period of 170 to 450 nm was formed in a shape perpendicular to the polarization. In Fused silica, the double femtosecond pulse experiment, which indicates the optical behavior of the material changing from dielectric to metal-like, showed that the periods of LIPSS showed great dependencies on the degree of optical excitation. He et al. found a controllable method for making nanostructures much lower than the diffraction limit [26]. Using femtosecond lasers (395 nm, 38 fs, 80 MHz), sufficient laser fluences (0.01 to 0.02 J / cm²) or peak intensity (2.7×10^{11} to 5.4×10^{11} W / cm²) were added to the glass surface to act as metal and to form a nanostructure due to interference with the laser incident surface. Multiple nanogrooves with 180 nm periods and 120 nm periods of nanowires were created, and based on the same mechanism a single nanostructure, 60 nm wide nanogroove and 40 nm wide nanowires were obtained. Numerical calculations including high-speed pulse propagation, field distribution and temperature rise were consistent with the phenomena observed in the experiment.

1.2.2.2. Lack of studies on LIPSS

In most cases, periodic leaves were created on the surface by irradiating femtosecond lasers on the metal, and changes in the color of the surface by diffraction were mainly made. Using LIPSS, the color shown through periodic surface structure is called structural color, and many papers experimented with various materials, and showed results. In general, LIPSSs in vertical direction of polarizing light using linear polarized beam are produced on the surface and color variations are indicated according to the angle of incidence of light for grating. Depending on the direction of polarization and the angle of incidence of light, the color will be changed by diffraction, and there was also a paper that arranged these according to the angle. There was a limit to the fact that these papers used LIPSS at a certain interval using a wavelength of laser. Among the phenomena that form LIPSS on the surface are single pulses and double pulses. Single pulse, as is known, appears under certain conditions under which the LIPSS is formed by adjusting the number of pulses and the fluence. The method using double pulse showed different dependence on the polarizing of the first pulse and the second pulse depending on the medium, and in the case of metal or semiconductor, the second polarizing was affected and in the case of dielectric, the dependence on the first polarizing. It is thought that the number of cases is insufficient, and LIPSS formation under various incident conditions will be possible.

II. TRANSPARENT CONDUCTIVE FILMS WITH CONTROLLABLE SHEET RESISTANCE ON GLASS SUBSTRATES BY LASER ANNEALING OF DIAMOND-LIKE CARBON FILMS

2.1. Introduction.

Graphene is arguably one of the most promising materials for many challenging applications due to its unique and exceptional properties [27-29]. With a rare combination of transparency in the visible range [30] and high electrical conductivity, for example, graphene is considered a next generation material for transparent conductive films and many researchers around the world are working to develop an efficient and cost effective method for producing large-area transparent conductive films based on graphene [31-33]. As of today, the most popular method of fabricating transparent conductive graphene films seems to be chemical vapor deposition. In this method, a graphene film is generally grown on a catalytic metal surface, which needs to be transferred to an actual substrate in a separate procedure [34-36]. For example, Bae et al. fabricated a large-scale, 30 inch graphene film by transferring a CVD grown film on a polyethylene terephthalate (PET) substrate by using a roll-to-roll method [31].

Recently, laser-based methods have been studied for fabricating graphene films, such as laser exfoliation of highly ordered pyrolytic graphite (HOPG) [4], laser-based epitaxial growth of graphene on silicon carbide [37], laser-induced chemical vapor deposition (LCVD) [5, 6, 38], and laser direct writing of graphene [7-9, 39]. In each of these methods, a high-density, high-precision optical energy at a selected wavelength is used as an energy source to thermally transform or evaporate the given carbon source. For instance, Xiong et al. developed a femtosecond laser based nanofabrication process for making graphene patterns on insulating substrates using a co-sputtered Ni/C thin film under ambient conditions [7].

Here, we report a simple and fully-scalable laser-based method for fabricating large-scale, graphene-based transparent conductive films with customizable sheet resistance on glass substrates using amorphous carbon as the carbon source. In this study, a DLC film was first deposited on a glass substrate, which was then annealed by a 2 kW continuous-wave laser in a shielding gas environment to prevent oxidation. The laser power and beam scanning speed were calculated based on the beam size to obtain the optimal process condition. By the annealing process, the sp^3 bonds in the film are transformed to sp^2 bonds, and graphene is formed from amorphous carbon. This method is fast and transfer free, and also is fully scalable with an adoption of a higher power laser and appropriate beam shaping optics. Due to its simplicity, high throughput, and cost effectiveness, this is a type of method that is preferred by industries. We believe that this study for the first time demonstrated the possibility of the laser-based

method for the fabrication of large-area transparent film heaters and transparent electrodes and it has a potential to become a new class of method in this field.

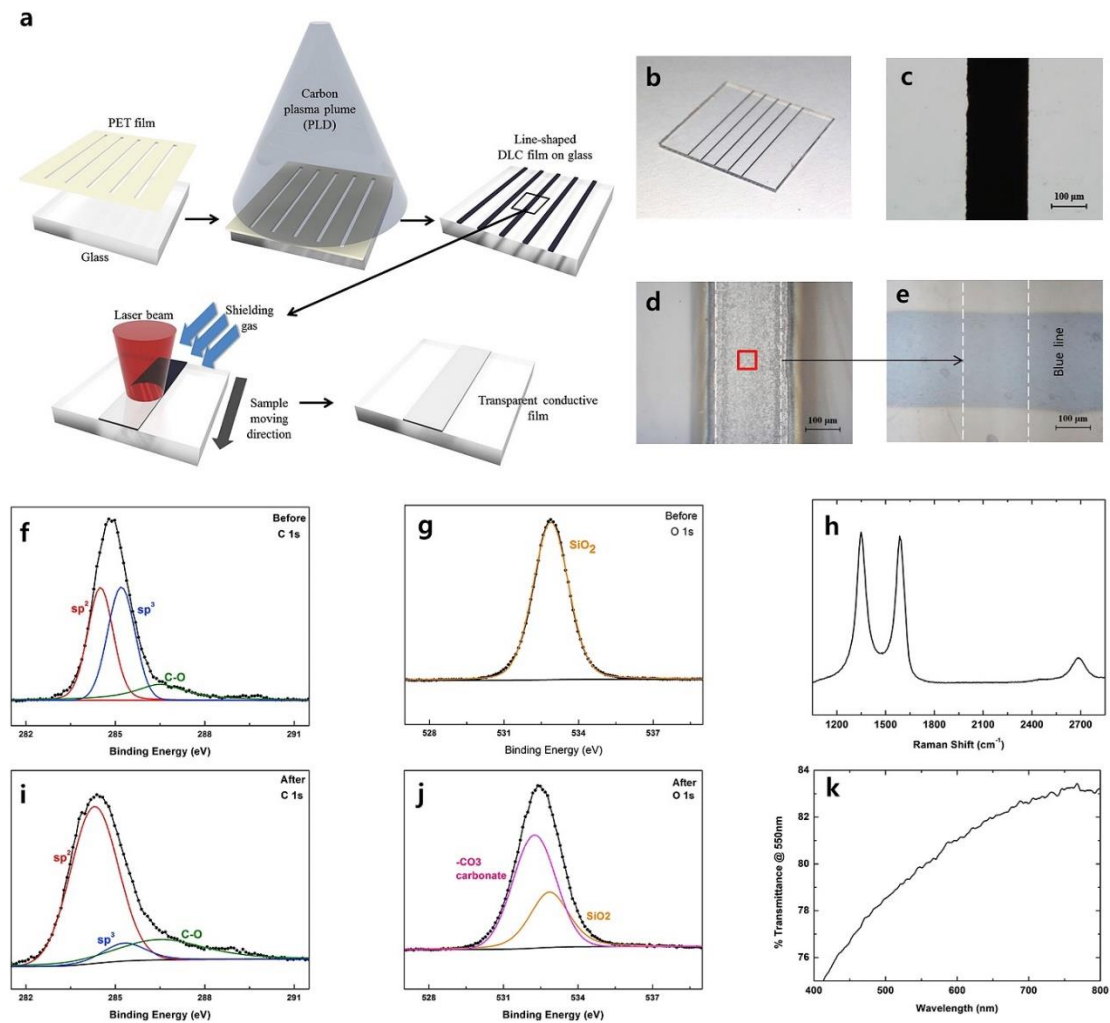


Figure 4. Fabrication of line-shaped transparent conductive films by laser annealing of DLC films with a circular top-hat beam (beam diameter 200 μm , laser power 110 W, scanning speed 1 m/s). (a) Schematic drawing of the overall experimental procedure for fabricating line-shaped transparent conductive films (b) Deposited line-shaped DLC patterns on a borosilicate glass substrate. Film thickness and width are 510 nm and 140 μm , respectively. (c) Optical microscope image of a deposited line-shaped DLC film on glass. (d) Optical microscope image of the top surface of a laser-annealed film (e) Optical microscope image of the underside of the film obtained by setting the image focal plane at the bottom of the annealed specimen shown in Figure 4d. The horizontal blue line located below the specimen shows that the DLC film became transparent (f,g) XPS results of the DLC film (shown in Figure 4c) for C 1s and O 1s. (h) Raman spectrum of the transformed film measured at the location shown in Figure 4d (i,j) XPS results of the transformed film (shown in Figure 4d and e) for C 1s and O 1s. (k) Transmittance versus wavelength measured at the location shown in Figure 4d.

2.2. High speed fabrication (1 m/s) of line-shape transparent conductive films using a circular laser beam

Figure 4a schematically shows the process of fabricating a line-shaped transparent conductive film. In this study, two lasers were used for the whole process: a 6 W picosecond laser for depositing DLC on a glass substrate and a 2 kW fiber laser for the annealing of DLC. First, a DLC film was deposited on a borosilicate glass substrate using pulsed laser deposition (PLD), where a 355 nm wavelength picosecond laser (Coherent Talisker 355-4) was used as an energy source for ablating a graphite target. The pulse width and the repetition rate of the laser are 10–15 ps and 200 kHz, respectively. The PLD process was performed in a vacuum chamber at room temperature and a pressure of $\sim 10^{-5}$ Torr. High purity graphite (99.999%) was used as the target material. To obtain a uniformly-annealed transparent conductive film by using a circular laser beam with a small beam diameter, we fabricated line-shaped DLC film patterns that have a width smaller than the beam diameter. For this process, a 50 μm thick PET film with line-shaped hole patterns (140 μm wide) was fabricated by the picosecond laser and was used as a disposable mask for the deposition process. Before deposition, glass substrates were cleansed in an ultrasonic bath using deionized water, acetone and IPA. The laser beam was focused at the target surface, which was rotating inside a vacuum chamber to obtain uniformly deposited films. Figure 4b shows line-shaped DLC films deposited on a glass substrate, and Figure 4c is a magnified image of one of the DLC patterns in Figure 4b. Here, the film thickness can be controlled by changing deposition time and laser power.

Once a DLC film was prepared, it was placed on a linear motion stage and annealed by a continuous-wave fiber laser with a top-hat intensity profile and a wavelength of 1070 nm. The beam diameter was 200 μm . In this way, the entire line-shaped DLC film can be annealed uniformly as the linear stage moves along the film length direction at a constant velocity. Here, by changing the laser power and the scanning speed, the temporal and spatial temperature profile in the DLC film can be controlled. Note that the glass is transparent to the 1070 nm light, so only the DLC absorbs energy from the laser beam and gets annealed without affecting the glass substrate much. Also, to prevent oxidation of carbon at elevated temperatures, a helium gas was injected to the interaction region through a nozzle. After the annealing process was finished, sheet resistance, optical transmittance, Raman spectra and XPS spectra were investigated. Sheet resistance R_s was calculated as $R_s = R \times (W/L)$, where R is the electrical resistance measured by a multi-meter (Fluke-114), and W and L are the width and length of the film. Electrodes at the ends of the line-shaped films were made by using silver paste. The optical transmittance of the annealed film was measured at the center of the film (50 $\mu\text{m} \times 50 \mu\text{m}$ area) by using a UV-Vis micro-spectrometer (CRAIC, Microspectra 121) for a wavelength range from 300 to 800 nm with a $\times 15$ objective lens. The transmittance of a bare glass specimen was measured to be used as a

reference.

In order to identify the transformed carbon structures, Raman spectroscopy was conducted using a WiTec alpha 300R Raman system with a 532 nm excitation wavelength (2.33 eV) and a laser power of 0.1 mW. The laser spot size was ~ 640 nm. Measurements were conducted at the center of the film, and 10 measurement values were accumulated to get one result using the WiTec control program. The obtained Raman spectra were analyzed by using the OriginPro 8 software.

Changes in chemical bonding before and after the annealing process were investigated using XPS. The XPS analysis was conducted using a K-alpha spectrometer (Thermo Fisher) which has aluminum $K\alpha$ with a pass energy of 50 eV, a measuring spot size of 0.2 mm and an energy step size of 0.1 eV. C1s and O1s spectra were analyzed. The peaks were fitted using the XPSPEAK software after the background was subtracted appropriately.

We observed that under proper process conditions the DLC film (which is nearly black in color) became transparent and the degree of transparency was found to depend on the process parameters. Also, the transformed films were found to be electrically conducting, implying that graphenization had taken place during the annealing process. When experimented with a 510 nm thick DLC film and a focused beam diameter of 200 μm , we obtained a sheet resistance of ~ 2050 Ω/sq and a transmittance of 80% (at 550 nm) at a laser power of 110 W and a scanning speed of 1 m/s. In Figure 4d and e, optical micrographs of upper side and underside of the transformed film are shown respectively. These pictures were obtained by setting the image focal plane at the top and bottom of the specimen, respectively, and they represent the exactly same area of the film. In Figure 4d, the surface morphology of the film can be seen and Figure 4e shows its transparency. In Figure 4e, a transparent plastic plate with a blue horizontal line printed on its top surface was placed below the film.

Figure 4h and k show the Raman spectrum and transmittance of the film, which were measured at the location shown as a red square in Figure 4d. In Figure 4h, three peaks are shown at 1349 cm^{-1} (the D band), 1589 cm^{-1} (the G band), and 2686 cm^{-1} (the 2D band) with a 2D-to-G intensity ratio (I_{2D}/I_G) ratio of 0.17 and a D-to-G intensity ratio (I_D/I_G) of 1.05. Note that I_D/I_G is an indicator of structural defects [40] and I_{2D}/I_G identifies the number of graphene layers [41]. Therefore, it is believed that the graphene formed from the laser annealing of DLC is multilayer graphene with a large amount of structural defects.

Figure 4f, g, i and j are X-ray photoelectron spectroscopy (XPS) results before and after the annealing process. As shown in Figure 4f and i, the C1s spectra show that the portion of sp^3 bonds decreased from 43.1% to 8.1% while the portion of sp^2 bonds increased from 43.6% to 70.7%, which

indicates that the ta-C structure of carbon had transformed to the graphitic structure due to the laser annealing process. Figure 4g and j are the O1s spectra of the film before and after the annealing process respectively. Before the annealing, the peak comes entirely from the glass substrate (SiO_2 at ~ 533 eV) because the DLC film does not contain oxygen. After the annealing, a carbonate ($-\text{CO}_3$) peak was observed as well as a SiO_2 peak. Note that borosilicate glass contains many elements other than SiO_2 , and we believe that carbonate was formed as the glass was partially melted and reacted with carbon.

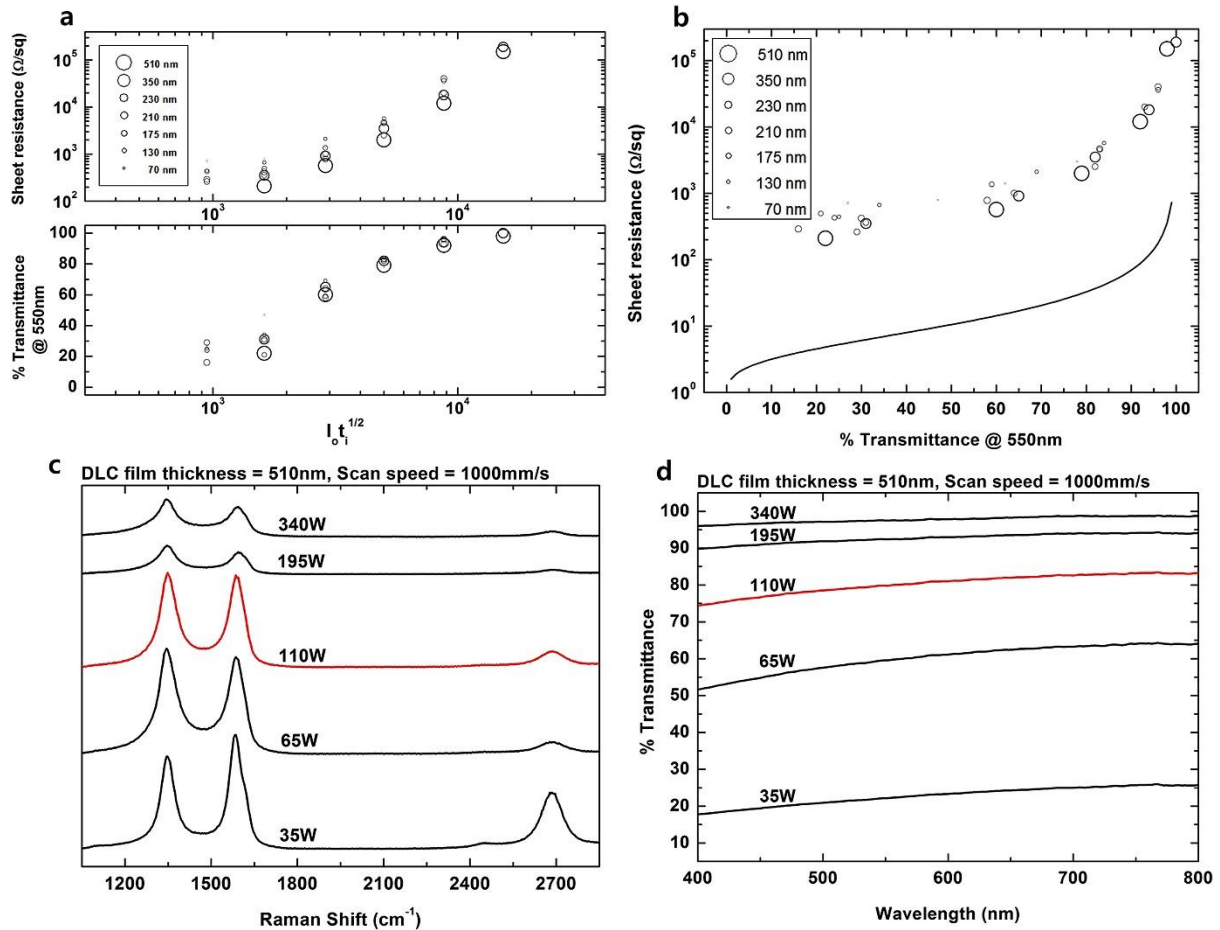


Figure 5. Controllable sheet resistance and transparency (beam diameter: $200 \mu\text{m}$). (a) Sheet resistance and transmittance (at 550 nm) versus $I_0 t_i^{1/2}$ for seven different film thicknesses, where I_0 is laser intensity and t_i is laser interaction time (b) Relationship between sheet resistance and transmittance. The black solid line shows the Beer-Lambert law. (c, d) Effect of laser power on Raman spectrum and transmittance for 510 nm thick DLC films that were annealed at 1 m/s. Red lines show the result showcased in Figure 4.

Figure 5 shows how sheet resistance and transmittance can be controlled as the process parameters are varied. In Figure 5a, sheet resistance and transmittance versus $I_0 t_i^{1/2}$ are shown for seven different

film thicknesses (70, 130, 175, 210, 230, 350 and 510 nm), where I_0 is the laser intensity (laser power divided by the beam area) and t_i is the interaction time (beam diameter divided by the beam scanning speed). In this experiment, the interaction time was fixed at 2×10^{-4} s (i.e., scanning speed is fixed at 1 m/s), and the operating condition was controlled by the laser power. Note that Kim and Ki showed that $I_0 t_i^{1/2}$ is a parameter that is proportional to the surface temperature during a laser heating process and can be interpreted as the degree of laser heating [42]. From this viewpoint, we can learn that sheet resistance and transmittance both increase as the surface temperature increases regardless of the film thickness. Apparently, the surface temperature will determine the kind of transformation that carbon undergoes, and is an important parameter in any laser annealing process as shown in the figure. The effect of film thickness is also shown in the figure: at the same surface temperature, both sheet resistance and transmittance seem to increase as the film thickness decreases, although sheet resistance seems to be affected more by the film thickness.

Figure 5b presents sheet resistance versus transmittance for all the data shown in Figure 5a along with the Beer-Lambert law [36] shown as a black solid line. As clearly shown, the relationship is similar to the Beer-Lambert law but the sheet resistance is higher by two orders of magnitude at the same transmittance. At $\sim 80\%$ transmittance, the minimum attainable sheet resistance seems to be $\sim 2050 \Omega/\text{sq}$, and as the transmittance increases beyond this value, sheet resistance increases rapidly. At $\sim 100\%$ transmittance, for example, the sheet resistance can be made larger than $10^5 \Omega/\text{sq}$ and we observed that the film can be virtually insulating when the $I_0 t_i^{1/2}$ value is increased further. Note that this relationship between sheet resistance and transmittance (as predicted by the Beer-Lambert law) implies that the increase in sheet resistance at very high transmittance is caused by the decrease in film thickness at high laser power, which was also verified by our experiment. As the laser power increases, more carbon atoms are vaporized and the annealed film thickness decreases. Using this characteristic, we can fabricate transparent conductive films with designed sheet resistance values.

Figure 5c and d present the Raman spectra and transmittance of the transformed films that were annealed using five different laser powers (35, 65, 110, 195 and 340 W). Film thickness and scanning speed were fixed at 510 nm and 1 m/s, respectively. The red lines show the result discussed in Figure 4. As shown clearly, the 2D peak is strongest at the lowest laser power of 35 W (where I_{2D}/I_G ratio is around 0.53), and becomes weakened as the laser power increases. The domain size (L_a) is estimated to be 14–23 nm according to $L_a = (2.4 \times 10^{-10}) \lambda^4 (I_D/I_G)^{-1}$, where λ is the Raman laser wavelength (532 nm) [43]. On the other hand, transmittance increases as the power increases and becomes close to 100% when the laser power is 340 W.

2.3. Large-scale laser fabrication using a line beam (beam width : 15 mm)

In order to demonstrate the scalability of the presented method, a beam-shaping diffractive optical element that can produce a $187.5 \mu\text{m} \times 15 \text{ mm}$ line beam was used to fabricate a $15 \text{ mm} \times 15 \text{ mm}$ film. Here, the size of the film was limited by the capacity of the PLD equipment, which can deposit uniformly thick films up to that size. In this case, unlike the circular beam experiment, the beam shape was close to Gaussian in the narrow side ($187.5 \mu\text{m}$), and the beam area is 89.5 time larger than the $200 \mu\text{m}$ circular beam. In this experiment, fused silica substrates were used. After the annealing process, optical transmittance was measured at the center of the film using a UV-Vis-NIR spectrometer (Agilent, Cary 5000), and a four-point probe system (AIT CMT-CR2000N) was used to measure electrical resistance.

Figure 6a schematically shows the process of fabricating a large-area transparent conductive film. Because the laser power is not enough to achieve the same sheet resistance and transparency as the result in Figure 6 because of the 89.5 times larger laser beam area, we chose a process condition that will lead to the smallest sheet resistance at 80% transparency (at 550 nm). For this, a 250 nm thick DLC film was first deposited and then annealed at a laser power of 1830 W (which is the maximum achievable power) and a scanning speed of 75 mm/s. Figure 6b and c respectively show the film before and after the annealing process. As shown, an initially opaque film became transparent and the measured sheet resistance was found to be $\sim 22 \text{ k}\Omega/\text{sq}$.

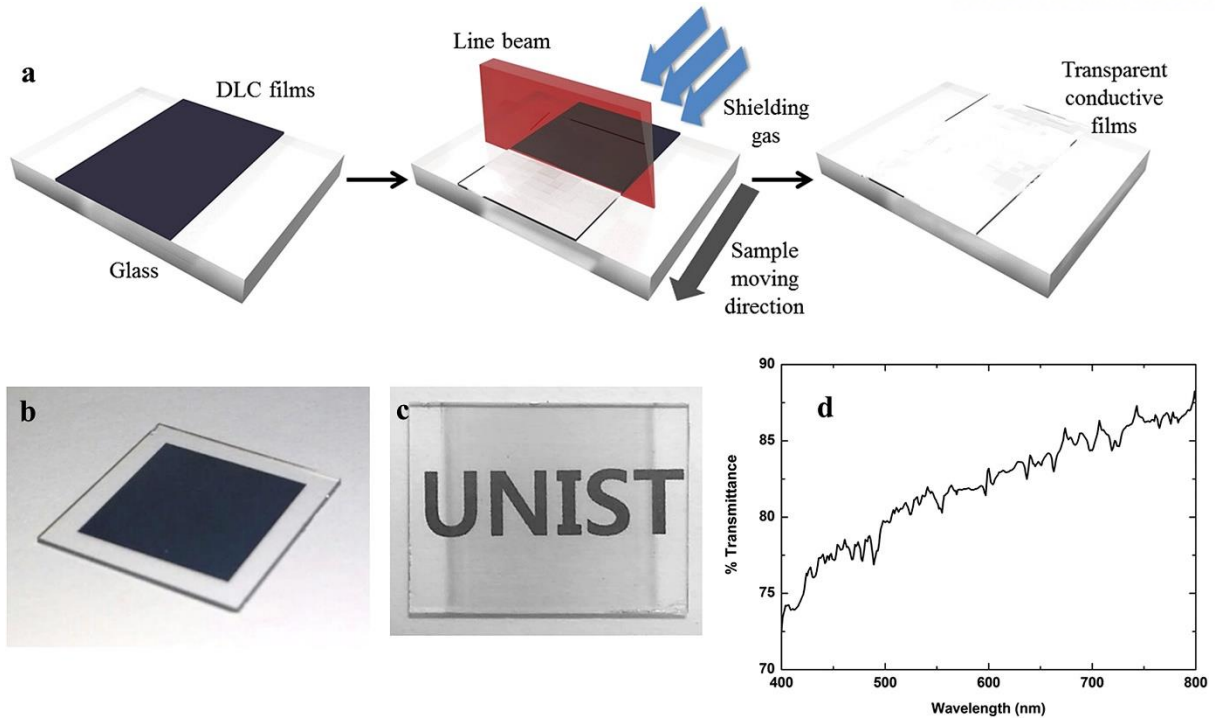


Figure 6. Fabrication of a large-scale transparent conductive film with a 15 mm wide line beam (laser power 1830 W, scanning speed 75 mm/s). (a) Schematic drawing of the overall experimental procedure for fabricating a large-area transparent conductive film. The film size is 15 mm \times 15 mm. (b) Deposited DLC film on a fused silica substrate. The film is almost black and non-conducting. (c) Laser-annealed film on a fused silica glass substrate. The film is transparent and conducting. (d) Transmittance versus wavelength.

2.4. Conclusion

We have demonstrated a laser-based method for rapidly fabricating graphene-based transparent conductive films on glass substrates by the laser annealing of DLC films in a shielding gas environment. The sp^3 bonds in the DLC films were significantly reduced and transparent conductive films were formed. The produced films seem to consist of multi-layer graphene with a large amount of defects. We demonstrated that films with a sheet resistance value as low as $\sim 2050 \Omega/\text{sq}$ at 80% transparency can be directly fabricated on glass without introducing a catalyst and a film transfer process. We also showed that sheet resistance can be controlled by changing the experimental parameters. Unlike other laser-based methods, this method was designed for fabricating large-scale films and the processing speed is fast. With further research and development, e.g., the use of the nanopatterning and chemical doping technique [44], we believe that the film quality could be much improved.

III. OPTIMIZATION OF TRANSPARENT CONDUCTIVE FILMS USING PICOSECOND LASER PATTERNING AND ETCHING

3.1. Introduction

Since graphene was discovered, researchers have tried to fabricate high-quality graphene films to replace indium tin oxide (ITO) because of its high optical transparency and low electrical resistance, but improving the transmittance while keeping low enough sheet resistance turned out to be a very challenging task. For graphene-based transparent conductive films, optical transparency and electrical conductivity are inversely proportional to each other, which is one of the reasons why improving the film quality is difficult.

For this reason, extensive research has been carried out to enhance the quality of graphene films using a number of different approaches, such as chemical doping, mixing with metallic materials, and reduction of graphene oxide. Kim et al. employed AuCl_3 doping to enhance the conductivity of transparent graphene and its sheet resistance was reduced by 77% [45]. Guens et al. [46] suggested a novel approach to improve the conductivity of graphene films by using a layer-by-layer doping process. Each layer was doped with AuCl_3 and four layers were stacked layer by layer to Exhibit $54 \text{ } \Omega/\text{sq}$ at 85% transmittance. Zhu et al. [47] fabricated transparent, flexible conducting films by using a metallic grid and graphene hybrid film. They reported that the sheet resistance of the fabricated transparent electrodes was as low as $3 \text{ } \Omega/\text{sq}$ with the transmittance at $\sim 80\%$. Lee et al. [48] developed hybrid electrodes by spin-coating silver nanowires onto graphene films to improve the performance. There were also attempts to develop hybrid films using graphene and carbon nanotubes [49, 50]. Recently, Voiry et al. [51] reported that 1–2 s pulses of microwaves could reduce graphene oxide into pristine graphene.

Another promising method for film property enhancement is the combined patterning and doping process. Recently, Choi et al. [44] reported a method of improving the optical transparency of graphene films substantially using nanopatterning and chemical doping. They fabricated hexagonal nanopatterns on the film surface to increase the optical transmittance and then restored the deteriorated electrical conductivity by chemical doping. Although their approach showed encouraging results, however, it is difficult to find optimal processing conditions that lead to the best results.

In this article, we propose a map-based approach for predicting the effect of patterning and doping, where all possible combinations of initial film conditions and the degrees of patterning are systematically accounted for, so that optimal film and processing conditions can be easily obtained from

the maps. For experimental verification, we utilized a laser-based method to fabricate graphene-based transparent conductive films directly on fused silica glass substrates, which was recently proposed by the authors [1]. In this method, a diamond-like carbon (DLC) film was deposited on a fused silica substrate using picosecond laser pulsed laser deposition, which was then annealed by a high-power fiber laser to be transformed to a transparent conductive film [1]. For patterning and doping, we chose film conditions of high electrical conductivity and low optical transparency to maximize the processing efficiency, and using a picosecond laser ablation process, circular or square patterns were fabricated and then chemical doping by nitric acid was performed. In this way, an original film with a sheet resistance of 578 Ω/sq and a transparency of 25% was transformed to a film with 2823 Ω/sq and 80.6%, which agreed well with predicted values.

3.2. Fabrication of optical transparent conductive films for patterning and doping

In this study, transparent conductive films were fabricated by a laser-based method, which was recently developed by the authors [1]. First, a 250 nm thick DLC film was deposited on a fused silica glass substrate by pulsed laser deposition (PLD) using a 355 nm picosecond laser (Coherent Talisker 355-4) (See Figure 7(a)). This laser had a maximum power of 6 W, a pulse width of 10–15 ps, and a repetition rate of 200 kHz. As the substrate, a fused silica glass wafer was used after cleaning in an ultrasonic bath using deionized water, acetone and IPA. High purity graphite (99.999%) was used as a target material, and the deposition was carried out inside a vacuum chamber that was maintained at $\sim 10^{-5}$ Torr. In this study, we tested two different deposition temperatures, room temperature and 900 °C in order to fabricate DLC films with different sp^2 and sp^3 fractions. As well known, DLC films deposited at higher temperatures have higher sp^2 contents (therefore, lower sp^3 contents), and we wanted to know whether the initial sp^2 content of the film could affect the quality of the annealed film. The Raman spectra of DLC films deposited at room temperature and 900 °C were measured using a confocal Raman imaging system (WiTec alpha300 R) and shown in Figure 8(a), (b), respectively. As shown in the figures, the center of the G peak was changed from 1523 cm^{-1} to 1564 cm^{-1} as the deposition temperature was increased from room temperature to 900 °C, which indicates that the sp^2 fraction also increased [52].

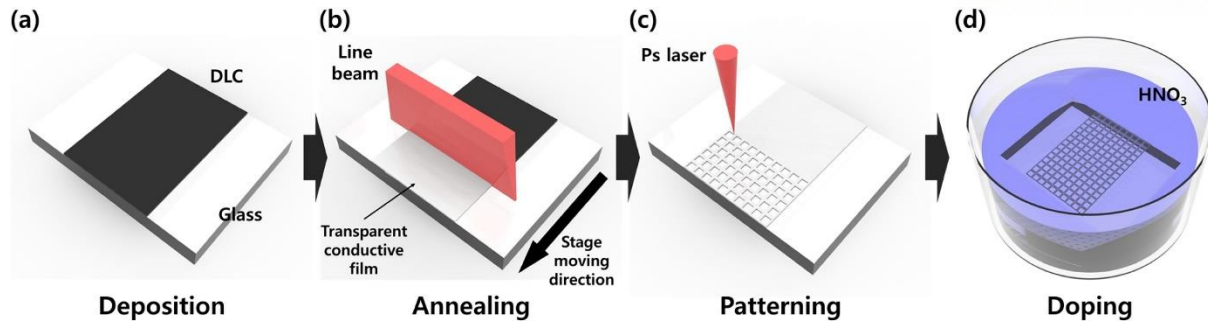


Figure 7. A schematic figure showing the overall procedure used in this study. A DLC film deposited on a fused silica glass substrate was annealed by a line laser beam and transformed into a transparent conductive film. A picosecond laser was used to fabricate patterns on the film surface to increase the optical transparency and a chemical doping process was employed to increase the electrical conductivity of the film.

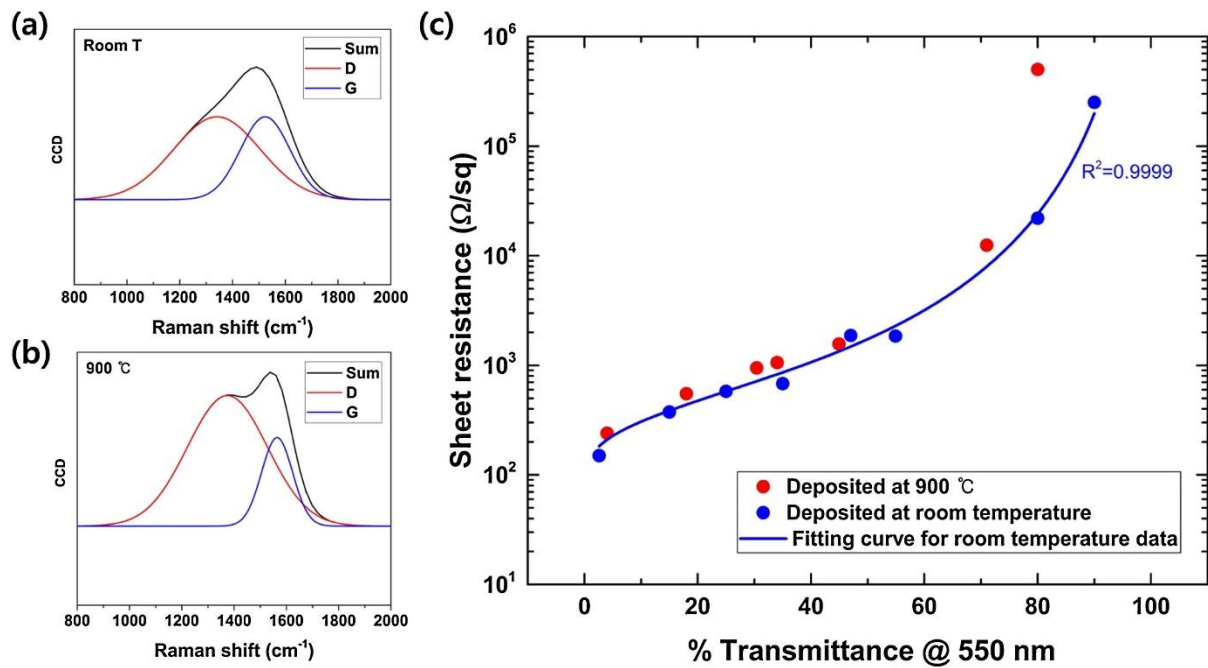


Figure 8. (a) Raman spectrum of a DLC film deposited at room temperature (before annealing), (b) Raman spectrum of a DLC film deposited at 900 °C (before annealing), (c) Measured sheet resistance and optical transparency (@ 550 nm) of annealed DLC films.

The deposited DLC films were black in color and electrically insulating. In order to obtain transparent conductive films, a continuous-wave (CW) 2 kW multi-mode fiber laser (IPG YLS 2000) was used as a heat source to anneal the DLC film into a transparent conductive film (Figure 7(b)). The fiber laser had a wavelength of 1070 nm and a circular top-hat intensity distribution, but we employed a beam shaping homogenizer to obtain a 15 mm × 0.1875 mm line beam. Using this line shape, the entire specimen can be evenly annealed by moving the specimen at a constant speed on a linear stage (Figure 7(b)). To avoid surface oxidation, helium was used as a shielding gas during the annealing process.

In this study, a total of 15 transparent conductive films were fabricated by using eight room-temperature deposited DLC films and seven 900 °C deposited films. Annealing was conducted at a constant annealing speed of 0.1 m/s for all specimens, but the laser power was varied to obtain films with different properties. For both types of DLC films, laser powers of 460, 545, 650, 770, 920, 1550, 1850 W were used and 1095 W was additionally used for the room-temperature deposited DLC films. After annealing, optical transparency was measured by a UV-Vis micro-spectrometer (CRAIC, Microspectra 121), and sheet resistance was calculated from the electrical resistance measured by a multi-meter (Fluke-114). For measuring electrical resistance, the electrodes were mounted with silver paste at both ends of the film. Fig. 2(c) shows the measured optical transparency (at 550 nm) and sheet resistance values of all 15 samples, where blue and red data points respectively denote the DLC films deposited at room temperature and 900 °C. Note that films annealed with higher laser powers become more transparent but electrically less conductive. As shown in the figure, sheet resistance increases as the optical transmittance of the film is improved, which is the behavior of graphene films, but the sheet resistance is much higher than good quality graphene films due to defects in the films.

One thing to note from Figure 8(c) is that the quality of the films obtained by annealing 900 °C deposited DLC films was slightly worse although they contained more sp² bonds before annealing. The main reason of this is believed to be the crystallite size (L_a) of the graphitic layer domain of the original DLC films, which is expressed as $L_a = (2.4 \times 10^{-10})\lambda^4(I_D/I_G)^{-1}$, where λ is the Raman laser wavelength (532 nm) and I_D/I_G is the D-to-G intensity ratio [43]. In Figure 8(a), (b), the I_D/I_G ratios for room-temperature and 900 °C deposited DLC films are 1.000 and 1.475, respectively, so the corresponding crystallite sizes are 19 and 13 nm. In other words, although the DLC films deposited at higher temperatures have higher sp² fractions, there are more defects, which lead to worse transparent conductive films after annealed by a laser. We believe that these defects are closely related to the high deposition temperature. In this study, therefore, we chose the room-temperature deposition condition for DLC films. The blue solid line shown in Figure 8(c) is the fitting curve for blue data points.

Figure 9 shows optical microscope (OM) images, scanning electron microscope (SEM) images, and Raman spectra of transparent conductive films which were annealed with, from left to right, 460, 545, 650, 770 and 920 W. As shown, the surface morphology was very non-uniform when low laser powers were used, and became smoother and finer as the laser power (and also transparency) increased. Because the main purpose of this study is to improve the quality of annealed films by means of laser patterning and chemical doping, good surface quality is critical and a film with a transparency of at least 25% should be used. In this study, therefore, we chose the film condition shown in Figure 9(c) for the film property optimization. Note that the roughness (R_a) of the film corresponding to this condition was measured to be ~ 88 nm.

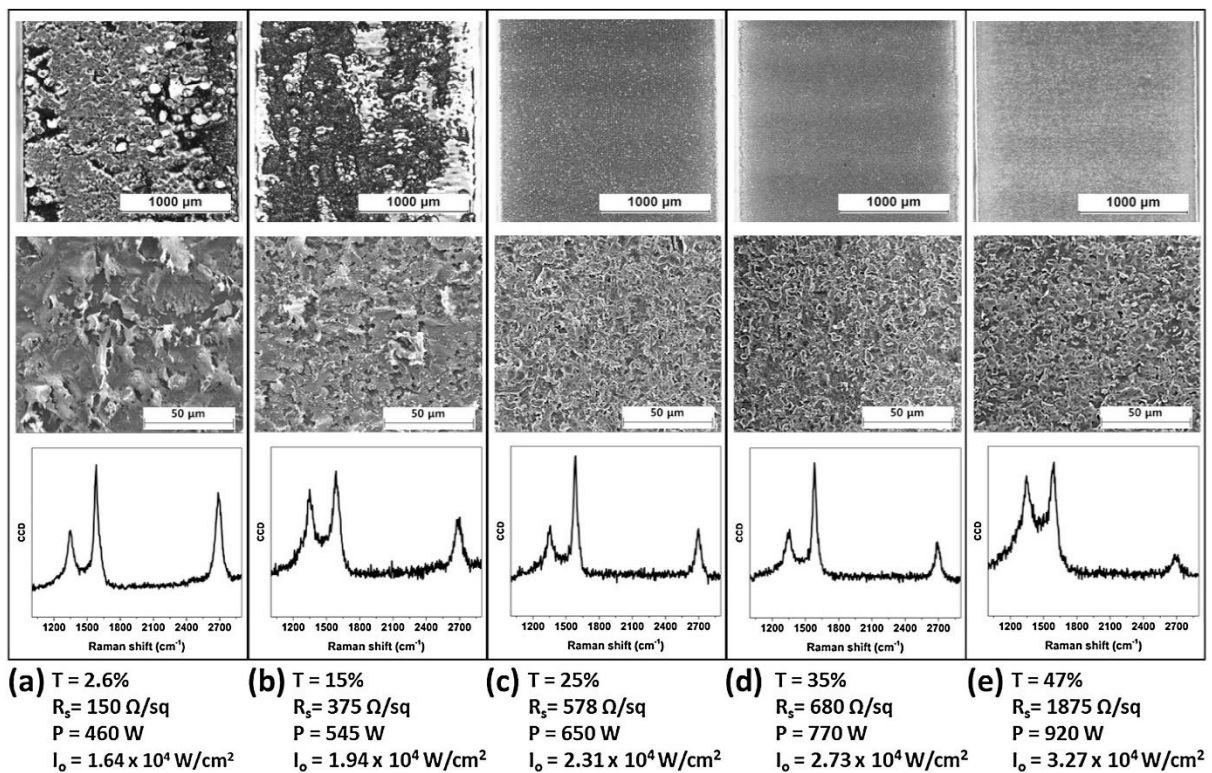


Figure 9. OM images (top row), SEM images (middle row), and Raman spectra (bottom row) of transparent conductive films annealed with 460, 545, 650, 770, 920 W, from left to right, respectively (annealing speed: 0.1 m/s). Corresponding sheet resistance and transmittance values are shown together. (Room-temperature deposited DLC films were used.).

Figure 9 also shows the Raman spectra of the annealed films corresponding to each power condition, and as shown, the quality of graphene became worse as the laser power increased. This explains why the sheet resistance increased as the laser power increased. Also, judging from the Raman spectra, the obtained graphene appeared to be multilayer graphene with a small crystallite size.

Figure 10 presents the sheet resistance versus the film thickness, which was measured five times for each film and average values were used in the figure. As shown, as the sheet resistance increased (or as the laser power increased), the film thickness decreased. We believe that more film was ablated (or evaporated) away by the laser beam at higher laser powers, resulting in thinner films.

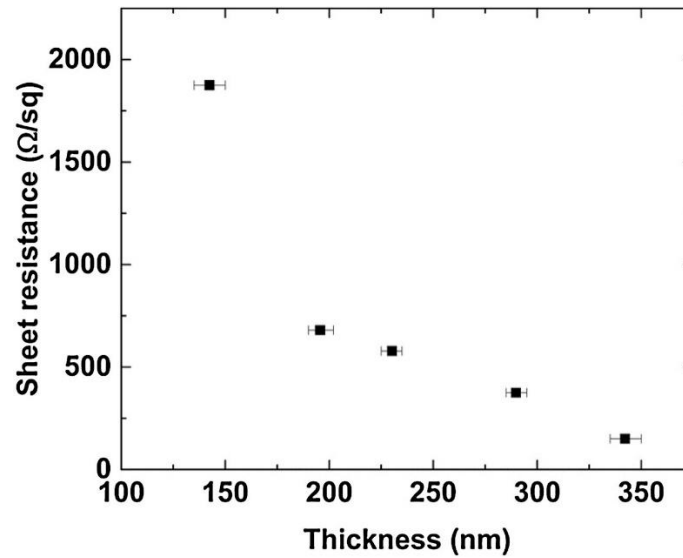


Figure 10. Sheet resistance vs. film thickness

3.3. Finding optical patterning and doping conditions

In order to enhance the optical transparency by laser patterning, the picosecond laser (Coherent Talisker 355-4) was used with a 3-D motorized stage. The laser beam had a Gaussian energy distribution with a focused beam diameter of 7 μm. An annealed transparent conductive film on a fused silica glass substrate (that shown in Figure 9(c)) was placed on a porous chuck, and only the film was selectively removed by the laser ablation process. For precise laser patterning, an optimal process condition must be determined. We first selected five laser power levels (0.01, 0.032, 0.1, 0.32, and 1 W) and five scanning speed levels (0.1, 0.32, 1, 3.16, and 10 mm/s), and a total of 25 conditions were used to fabricate line patterns on annealed films, as shown in Figure 11. Here, the pulse repetition rate was fixed at 200 kHz for all cases. As shown, due to excessive laser energies, higher three power levels (1, 0.32, 0.1 W) resulted in thermal damages in the film around the fabricated lines regardless of the beam scanning speed and were unsuitable for patterning films. From the result, it appeared that the optimal condition existed in a process window bounded by 0.032 W, 0.1 W and 0.32 mm/s, 1 mm/s. As shown in Figure 12, we tested five more conditions inside the narrowed-down process window, and determined the optimal process condition of 0.032 W and 0.56 mm/s.

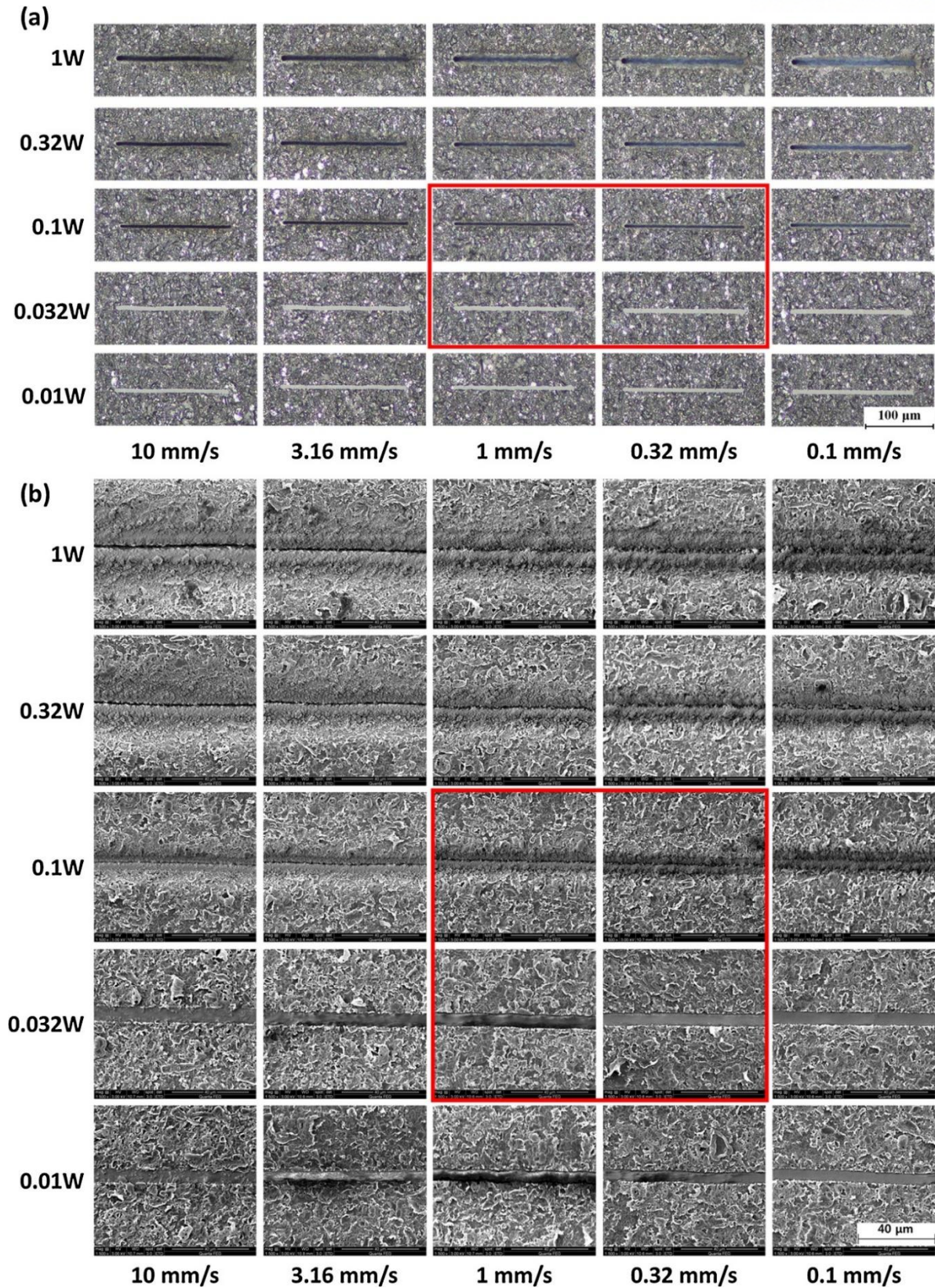


Figure 11. (a) OM and (b) SEM images of the line patterns fabricated on the transparent conductive films (shown in Fig. 3(c)) using 25 different patterning conditions.

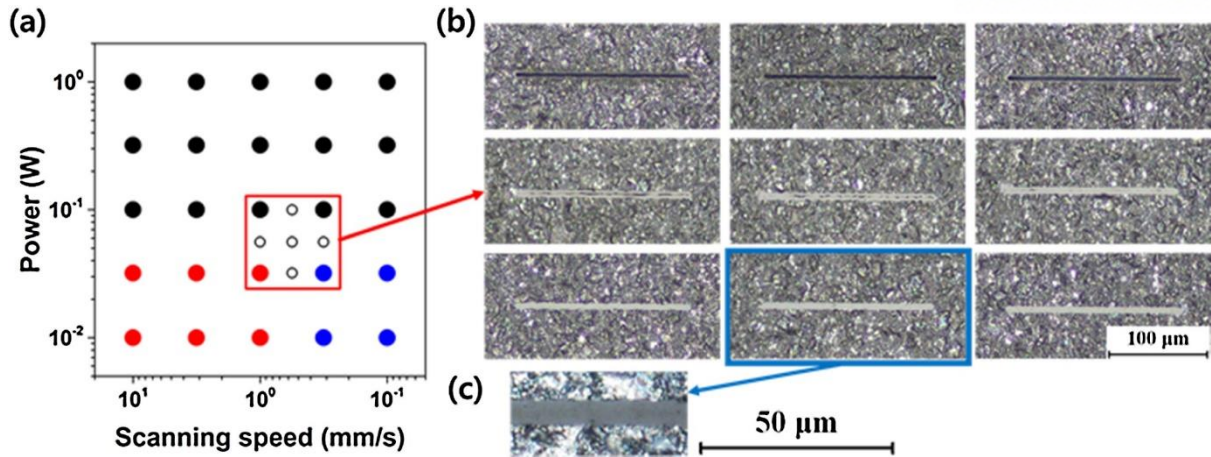


Figure 12. (a) From the line patterning result shown in Fig. 5, a narrowed-down process window (red box) was identified and five more experiments were additionally conducted (small white circles). (b) Patterning results corresponding to the nine conditions. The result shown in the blue box was found to be the optimal patterning condition. (c) Magnified image of the optimal line pattern.

After patterning, chemical doping was performed to improve the electrical conductivity which was deteriorated by the patterning process. In this study, we tested two different dopants, HNO_3 (60 wt%) and HCl (35 wt%), and to find the optimal doping time, several different doping times were tried. After doping, the films were rinsed using DI water and nitrogen gas. Figure 13 shows the % reduction in sheet resistance plotted versus doping time for two different acids. As shown, when doped by HNO_3 for 10 min, the reduction in sheet resistance was maximum at $\sim 27\%$, so this was identified as the optimal doping condition for this study.

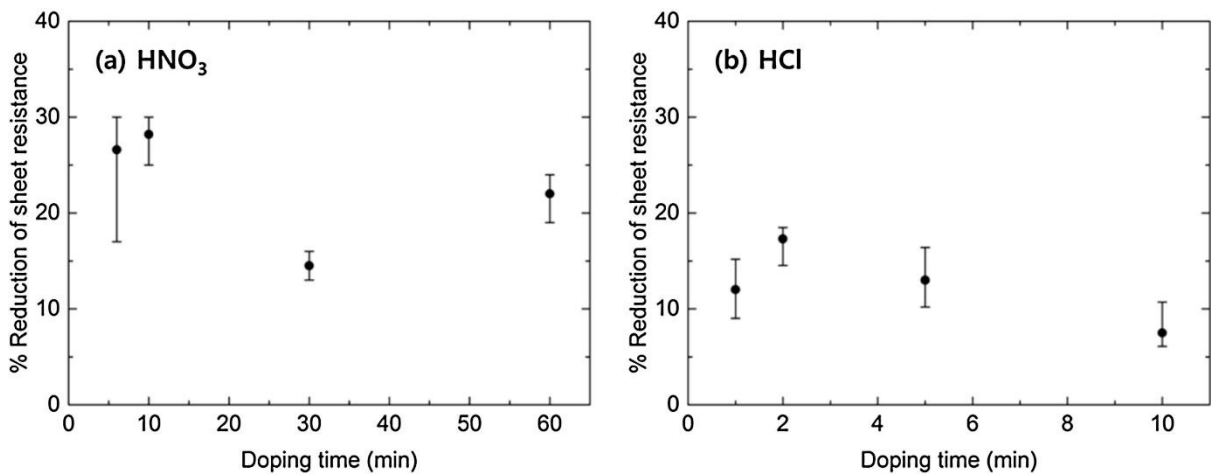


Figure 13. % reduction of sheet resistance after doping by (a) HNO_3 and (b) HCl .

3.4. Prediction model for sheet resistance and transparency after patterning and doping

The aim of this study was to obtain prediction models for sheet resistance and optical transparency of transparent conductive films after laser patterning and chemical doping. In this section, we will show how prediction maps can be constructed by taking into account all film conditions and patterning degrees. Although this approach is not limited by pattern shapes, we considered only circular and square patterns for the sake of simplicity.

Figure 14(a), (b) show schematic drawings of conductive films with circular and square patterns, respectively. For each pattern, a unit cell is shown by a dashed square in Figure 14(c), (d), which is repeated on the entire film. In this study, we defined the area ratio r_A as the ratio of the ablated pattern area to the unit cell area, which is calculated as

$$r_A = \begin{cases} \frac{\pi D^2 / 4}{d^2} & \text{for circular patterns} \\ r_A = \frac{l^2}{d^2} & \text{for square patterns} \end{cases} \quad (1)$$

where D is the diameter of a circular pattern, l is the one-side length of a square pattern, and d is the horizontal and vertical distance between patterns. Assuming that transparency of the ablated region is 100% and letting the original film transparency be T_0 , the effective film transparency with patterns (T_f) can be calculated as follows:

$$T_f = 1 \cdot r_A + T_0(1 - r_A) = (1 - T_0)r_A + T_0 \quad (2)$$

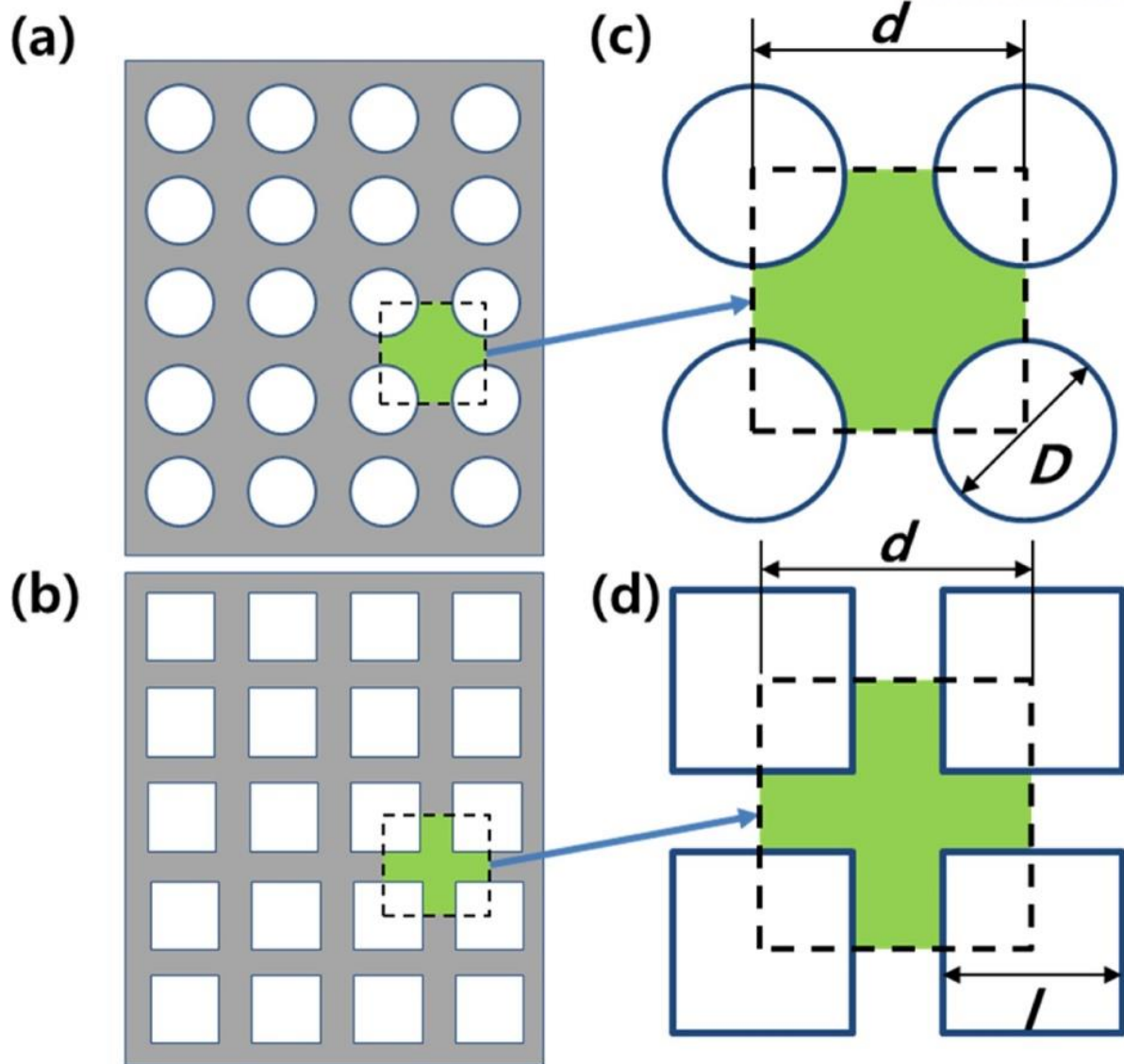


Figure 14. (a, b) Schematic drawings of the films with circular and square patterns, (c, d) Unit cells identified from the left figures.

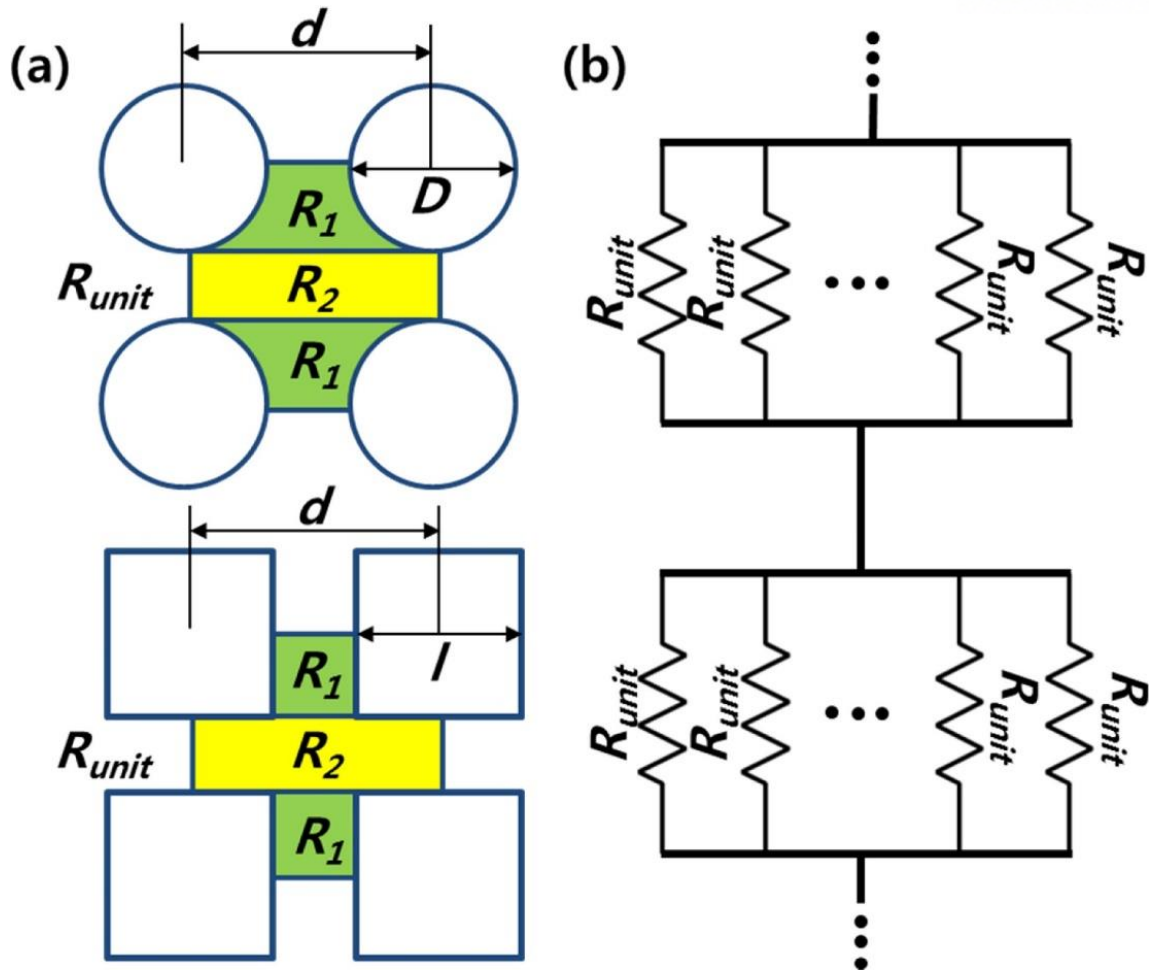


Figure 15. (a) Schematic drawings showing how the electrical resistance of a unit cell (R_{unit}) was calculated for circular and square patterns by breaking down the unit cell into smaller regions ($R_{unit} = R_1 + R_2 + R_1$) (b) Electrical circuit representation of the entire film constructed by connecting the electrical resistance of a unit cell in series and in parallel.

As shown from Eq. (2), the transparency of patterns films is linearly proportional to the area ratio r_A .

Figure 15(a) shows how the electrical resistance of a unit cell ($R_{unit} = R_1 + R_2 + R_1$) was calculated by breaking down the non-patterned area into three regions for both pattern types. For each region, the electrical resistance (R) was calculated from the sheet resistance of the transparent conductive film ($R_{s,0}$) by using the relation between them for a rectangular domain, i.e.,

$$R = R_{s,0} \frac{L}{W} \quad (3)$$

where W and L are the width and length of the domain. For example, for the circular pattern in Figure 15(a), R_2 can be calculated easily as

$$R_2 = R_{s,0} \frac{d-D}{d} \quad (4)$$

Because of its non-rectangular shape, however, R_1 for the circular pattern should be integrated by splitting the region into horizontal strips as

$$R_1 = \frac{R_{s,0}}{2} \int_0^{\pi/2} \frac{D \cos \theta}{d - D \cos \theta} d\theta = \frac{R_{s,0}}{2} \ln \left(\frac{2d \tan^{-1} \left(\frac{\sqrt{d+D}}{\sqrt{d-D}} \right)}{\sqrt{d^2 - D^2}} - \frac{\pi}{2} \right) \quad (5)$$

and, then

$$R_{unit} = 2R_1 + R_2 \quad (6)$$

Once R_{unit} is calculated, the electrical resistance of the entire patterned film (R_f) can be calculated by viewing the film as an electrical circuit constructed by connecting the unit cells in series and in parallel, as shown in Figure 15(b). If the width and the length of the whole film are W_f and L_f , respectively, then it is as though there are W/d unit cells horizontally and L/d unit cells vertically. Therefore, the electrical resistance of the whole patterned film (R_f) is

$$R_f = \frac{R_{unit}}{\frac{W_f}{d}} \times \frac{L_f}{d} = R_{unit} \times \frac{L_f}{W_f} \quad (7)$$

and comparing with Eq. (3), we can learn that the effective sheet resistance of the whole patterned film ($R_{s,f}$) is the same as the electrical resistance of the unit cell, R_{unit} . Finally, we can express $R_{s,f}$ in terms of the area ratio r_A of circular patterns (Eq. (1)) as

$$R_{s,f} = R_{s,0} \times \left(\frac{2 \tan^{-1} \left(\frac{\sqrt{\pi + 2\sqrt{r_A}}}{\sqrt{\pi - 2\sqrt{r_A}}} \right)}{\sqrt{1 - 4\frac{r_A}{\pi}}} - 2\sqrt{\frac{r_A}{\pi}} - \frac{\pi}{2} + 1 \right) \quad (8)$$

Because

$$\frac{D}{d} = 2\sqrt{\frac{r_A}{\pi}} \quad (9)$$

from Eq. (1).

In the case of square patterns, R_1 and R_2 are both rectangles, and are easily written as

$$R_1 = R_{s,0} \frac{l}{d-l} \quad (10)$$

$$R_2 = R_{s,0} \frac{d-l}{d} \quad (11)$$

and the sheet resistance of the patterned film is calculated in terms of r_A as

$$R_{s,f} = R_{s,0} \times \frac{1 - \sqrt{r_A} + r_A}{1 - \sqrt{r_A}}, \text{ where } \frac{l}{d} = \sqrt{r_A} \quad (12)$$

Note that for both optical transparency (Eq. (2)) and sheet resistance (Eqs. (8) and (12)) of the patterned films are expressed by using the properties of the annealed film ($R_{s,0}$ and T_0) and only one additional parameter, r_A .

Here, in order to construct prediction maps for the laser-fabricated transparent conductive films, the relationship between sheet resistance ($R_{s,0}$) and optical transparency (T_0) shown as a blue line in Figure 8(c) was used in this study. The blue fitting curve was mathematically expressed as

$$R_{s,0} = \frac{a}{(\ln T_0)^3} + \frac{b}{(\ln T_0)^2} + \frac{c}{\ln T_0} \quad (13)$$

where $a = -215.55$, $b = 86.67$ and $c = -626.06$. Note that, from the Beer-Lambert law, the sheet resistance of graphene is theoretically given as $R_s \sim 1/\ln T_0$ [36]. But, the graphene films used in this study were not pure graphene sheets and contained a lot of defects. Therefore, the curve was up-shifted, and we employed a third-order polynomial of $1/\ln T_0$ for curve fitting.

Using Eqs. (2), (8), (12), (13) and the measured optimal doping efficiency of $\sim 27\%$, we constructed prediction maps for the sheet resistance and optical transparency of transparent conductive films after laser patterning and doping, as shown in Figure 16. In each figure, the x- and y-axes represent the area ratio (r_A) and the optical transmittance (at 550 nm) of the patterned film (T_i). A dotted line

extended from an initial transparency value (y-axis value where r_A is zero) shows how transparency is improved as the degree of patterning increases along the line. Note that the transparency is linearly proportional to r_A , so the effect of area ratio on transparency is shown as (dotted) lines. Also, colored contours indicate the predicted sheet resistance at the given point. For example, if a film initially having a transparency of 25% and a sheet resistance of 578 Ω/sq (which was identified as the optimal film condition in this study) is ablated by 73% using circular patterns and doped by HNO_3 for 10 min, the resulting film is expected to have a sheet resistance of 4448 Ω/sq and a transparency of 80%, which is denoted as a red arrow in Figure 16(a). Also, if the same film is removed by 73% ($r_A = 0.73$) using square patterns, followed by 10 min doping by HNO_3 , a film of 2579 Ω/sq and 80% transparency is expected, as shown by a red arrow in Figure 16(b).

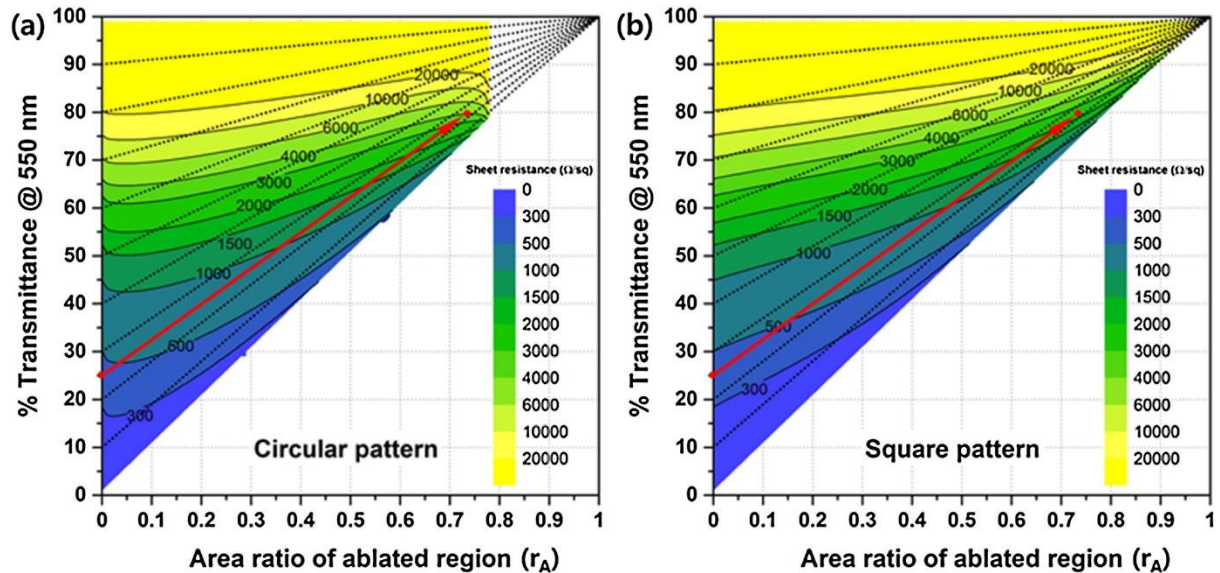


Figure 16. Prediction maps for sheet resistance and optical transparency of transparent conductive films after patterning and doping for (a) circular patterns and (b) square patterns

From the maps, we can also notice that, at 80% transparency, the minimum sheet resistance of the films processed by patterning and doping is 739 Ω/sq when an original film of 1% transparency and 119 Ω/sq is ablated using square patterns. As shown in Figure 9, however, this film surface is too rough and not suitable for laser patterning.

In this study, we also constructed figure-of-merit maps for circular and square patterns and presented in Figure 17. The only difference between Figure 16, Figure 17 is that colored contours

in Figure 17 represent predicted figure-of-merit values. As well known, the figure of merit indicates the performance of transparent conductive films [46, 53] and is expressed as

$$\frac{\sigma_{DC}}{\sigma_{Op}} = \frac{Z_0 / 2(0.73R_{s,f})}{\frac{1}{\sqrt{T_f}} - 1} \quad (14)$$

where σ_{DC} is DC conductivity, σ_{Op} is optical conductivity, Z_0 is the impedance of free space ($377 \Omega/\text{sq}$), and the number 0.73 represents the amount of sheet resistance decreased by the optimal doping process (27%) used in this study. As shown in Figure 17(a), the largest figure-of-merit for circularly patterned films is 1.59, where the patterned and doped film has a sheet resistance of $407 \Omega/\text{sq}$ and a transparency of 60%. For square patterns, the largest value is 2.18 and the corresponding sheet resistance and transparency are $17138 \Omega/\text{sq}$ and 99%, respectively. For the process shown by a red arrow in Figure 16 ($2579 \Omega/\text{sq}$ and 80%), the expected figure of merit is 0.65.

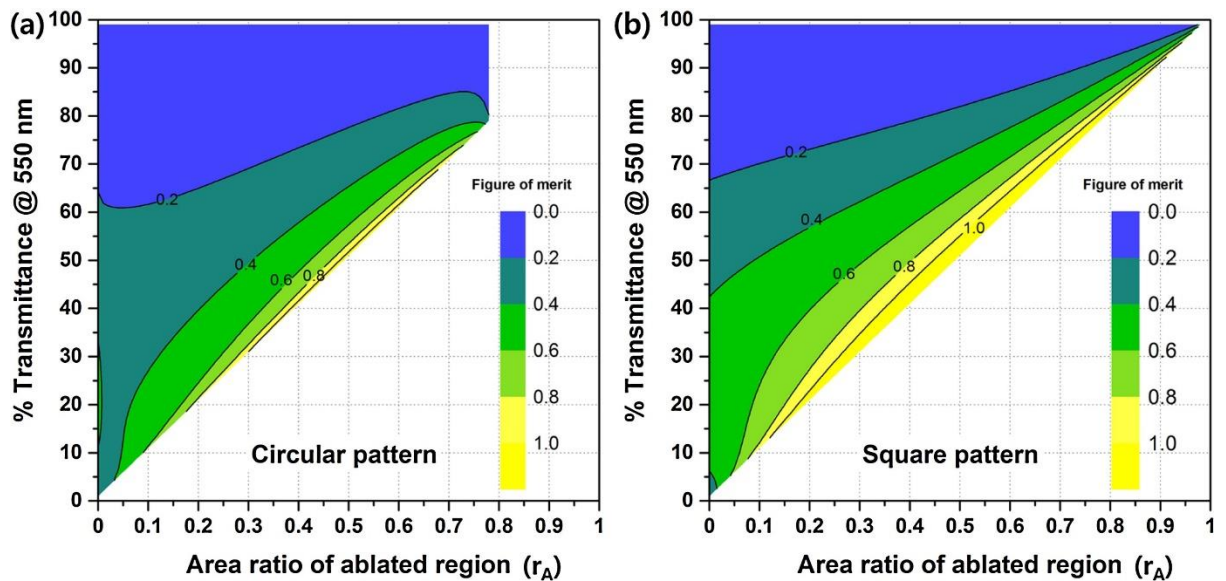


Figure 17. Prediction maps for the figure-of-merit of transparent conductive films after patterning and doping for (a) circular patterns and (b) square patterns.

3.5. Experimental verification

In order to experimentally verify the prediction maps described in the previous section, we fabricated two types of films using the process conditions shown by the red arrows in Figure 16(a), (b).

For patterning and doping, the optimal condition found in Section III (0.032 W and 0.56 mm/s, 10 min doping by HNO_3) was used (See Figure 7(c), (d)). For the patterning process, each pattern was fabricated by employing a hatching scheme, i.e., drawing lines repeatedly in one direction using a 3-D motorized stage. The size of the film used for patterning was $2 \text{ mm} \times 6 \text{ mm}$, and the thickness of the film was around 230 nm.

Figure 18(a) shows the optical microscope images of the film surfaces at three different stages during the fabrication procedure. The left figure is the DLC film, which is black and completely opaque, the middle two figures are the annealed transparent conductive films, which exhibit $\sim 25\%$ transparency and $\sim 578 \Omega/\text{sq}$ sheet resistance, and the right two figures are the images of the films after laser patterning and chemical doping. The patterned film images (both circular and square patterns) show that picosecond laser patterning with the optimal ablation condition produced very precise patterns. In Figure 18(b), the transmission spectra of the films after annealing, patterning, and doping are presented, and as shown, the optical transmittance was improved significantly by the patterning process, but was not altered by the doping process. In Figure 18(c), the films at the corresponding three stages were placed on a paper with printed colored lines to demonstrate how the transparency changed due to annealing and laser patterning. As shown, the original DLC films on the left is completely opaque, the middle annealed film shows a small degree of transparency ($\sim 25\%$), and the right one is fairly transparent.

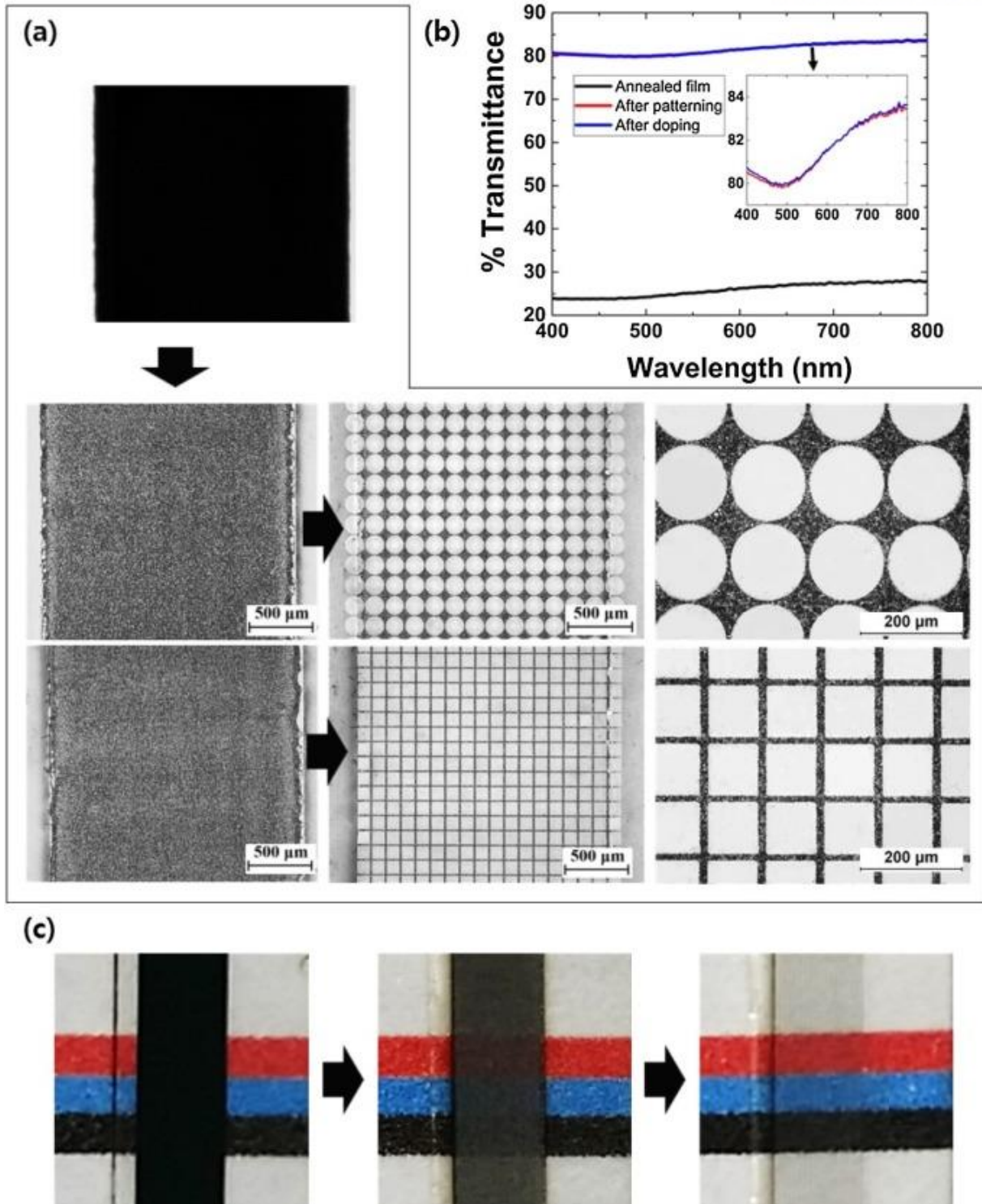


Figure 18. (a) Optical microscope images of the films at different stages. The left black figure is the image of a DLC film, the middle ones are annealed films ($\sim 25\%$ transparency), and the right ones are the films after laser patterning and chemical doping. (b) Transmission spectra of the films at different stages. (c) Films at the three corresponding stages were placed on a paper with printed colored lines, showing that the transparency improved after laser annealing and laser patterning.

We measured the sheet resistance and optical transparency of the two films after patterning and then after doping again, and summarized the measurement data together with the predicted values in Table 1(a). In the case of the square-patterned film, measured sheet resistance and transparency were 3910 Ω /sq and 80.5% after patterning, and 2823 Ω /sq and 80.6% after doping. As for the film with circular patterns, measured sheet resistance and transparency were 6300 Ω /sq and 79.1% after patterning, and 4640 Ω /sq and 79.3% after doping. For both films, transparency was much more accurately predicted (0.6–1.1%) than the sheet resistance (3.4%–10.7%). This is because, while transparency is a function of ablated area ratio only, sheet resistance is more critically affected by the quality (or sharpness) of the fabricated patterns. Due to the same reason, sheet resistance of the square-patterned film was less accurately predicted because long sharp lines are much more difficult to fabricate using lasers.

Table 1. Predicted and measured properties of the fabricated films (units: $R_{s,f}$ (Ω /sq), T_f (%))

			Square patterns			Circular patterns		
			Predicted	Measured	Error	Predicted	Measured	Error
25%	After patterning	$R_{s,f}$	3532	3910	10.7%	6093	6300	3.4%
		T_f	80	80.5	0.6%	80	79.1	1.1%
	After doping	$R_{s,f}$	2579	2823	9.5%	4448	4640	4.3%
		T_f	80	80.6	0.7%	80	79.3	0.9%
45%	After patterning	$R_{s,f}$	5567	6144	10.4%	7385	7377	0.1%
		T_f	80	80.8	1%	80	81	1.2%
	After doping	$R_{s,f}$	4064	4611	13.5%	5391	5460	1.3%
		T_f	80	80.6	0.75%	80	81.2	1.5%
55%	After patterning	$R_{s,f}$	7308	7550	3.3%	9365	9141	2.3%
		T_f	80	79.8	0.25%	80	80.5	0.63%
	After doping	$R_{s,f}$	5335	5685	6.2%	6836	6851	0.2%
		T_f	80	80.2	0.25%	80	80.3	0.38%

For additional verification examples, we conducted two more tests using the annealed films with 45% and 55% transparency conditions and listed the results in Table 1(b) and (c). As shown, the obtained results were reasonably good.

As summarized in Table 1, square patterns are more effective than circular patterns in terms of enhancing the transmittance because more film is removed. Note that, when it comes to the design of ideal patterns, it should have as large an ablation area as possible, and at the same time, it should be nondirectional.

3.6. Conclusion

In this study, we proposed a map-based approach for predicting sheet resistance and optical transparency of graphene-based transparent conductive films after patterning and doping. This approach is very systematic such that the overall effect of the two processes can be efficiently predicted considering all possible combinations of the initial film condition and the area ratio of ablated region. Although we validated the method using transparent conductive films fabricated by laser annealing and picosecond laser patterning was used, the proposed approach can be applied to virtually all types of transparent conductive films and patterning methods.

IV. FEMTOSECOND LAER PATTERNING BASED ON THE CONTROL OF SURFACE REFLECTANCE

4.1. Introduction.

Nanopatterns fabricated on the surface of a structure can change the reflection behavior, as the incident light undergoes complex interactions with the patterns. To modify the reflectance of a surface, periodic grating structures must be created on the surface, and their periods should lie in the wavelength range of visible light. Although conventional methods, such as mechanical fabrication, chemical etching, coating, and lithography [54-57], have been used for these purposes, they are generally very complex to implement and have clear imitations owing to the small feature sizes of the reflectance-modifying patterns. With an intrinsic advantage in small-scale precision pattern fabrication, laser patterning has been extensively used to create reflectivity-modified surfaces. For example, Jwad et al. developed a single-spot oxidation method for creating structural colors on titanium by using a nanosecond laser and fabricated color images using the developed method [58]. Veiko et al. also developed a method of laser-induced coloration for metals based on the diffraction effect, in which a nanosecond fiber laser was employed to create small-scale periodic structures [59].

Although many laser patterning methods exist, the LIPSS has been the primary method for changing the reflection behavior of surfaces, because of its intrinsic capability of fabricating nanopatterns beyond the diffraction limit. LIPSS patterns are regularly-spaced nanoscale surface ripples aligned perpendicular to the polarization of a laser beam (sometimes not perpendicular to the polarization of a laser beam when LIPSSs are generated on microstructures with height gradients [60] or depending on the material and process conditions [61]) and can be easily created by a femtosecond laser. These patterns appear in a wide variety of materials, such as metals [62], semiconductors [63], and dielectrics [64]. The LIPSS can be formed by a picosecond laser [65]; however, most of the LIPSS studies are conducted by using a femtosecond laser. Long et al. fabricated LIPSS-based functional copper surfaces combined with structural colors and superhydrophobicity by using a picosecond laser [65]. Li et al. reported the modification of aluminum surfaces by femtosecond laser pulses with different pulse overlap ratios. They generated several colors by varying the pulse overlap [66]. Yao et al. fabricated ripples with a sub-wavelength period on 301 L stainless steel by using a femtosecond laser, and they demonstrated the possibility of decorating the same region with two or more types of ripples with different orientations [67]. Ou et al. fabricated rippled copper surfaces using a femtosecond laser and demonstrated that the colorizing effect of angle dependence can be achieved with an out-of-focus method [68]. Calvani et al. studied the optical properties of femtosecond-laser surface-textured diamond and reported a significant increase in the visible and infrared absorption (more than 80%) compared to

untreated specimens (less than 40%) [23]. Iwase et al. reported that the sub-wavelength gratings were fabricated on the surface of nickel without the formation of ripples using the interference of two p-polarized femtosecond laser beams at a 45° angle of incidence [69].

Among other materials, stainless steel has been frequently used for studying LIPSS, because of its corrosion resistance and wide adoption in various industries, including jewelry and ornaments: the modification of the stainless steel surface using LIPSS could be an effective way of expressing color and contrast. Li et al. studied the femtosecond laser color marking on stainless steel using different laser wavelengths, and found that the surface color gradually changes from blue to red because of the elongation of the diffracted light wavelengths [70]. Dusser et al. demonstrated the possibility of achieving specific color patterns on stainless steel by the control of nanostructure orientation using femtosecond laser pulses [14].

Although the LIPSS has been studied extensively for decades, a systematic study on how the reflectance of LIPSS-patterned surfaces varies on a large process window is yet to be explored, especially for stainless steel. In this study, we investigated the effect of process parameters on the reflectance of LIPSS patterns fabricated on stainless steel and developed a reflectance map. Using the map, we developed a laser-patterning method that is capable of fabricating patterns with varying surface reflectance and successfully fabricated multi-faceted balls on stainless steel. This paper reports on the formation of holes under certain conditions, and how the holes are connected to produce secondary patterns and change the reflection behavior of the patterned surfaces. The effect of shield gas type on the surface oxidation and the change in the surface reflection were also investigated.

4.2. Experimental setup

Figure 19 shows a schematic of the experimental setup. In this study, a 1030 nm femtosecond laser (Pharos 15-200-PP) with a pulse duration of 220 fs and a repetition rate of up to 200 kHz was utilized. The maximum attainable laser power at the specimen surface was 10.96 W at 200 kHz, and a repetition rate of 1 kHz was chosen in this study. An f-theta lens with a focal length of 160 mm was used for beam focusing, and a motorized x-y stage was employed for pattern fabrication. With this optical setup, the focused spot diameter was 50 μm, and the attainable maximum fluence was 5.53 J/cm². To control the laser power, an attenuator was used, and the polarization direction was adjusted by a half-wave plate.

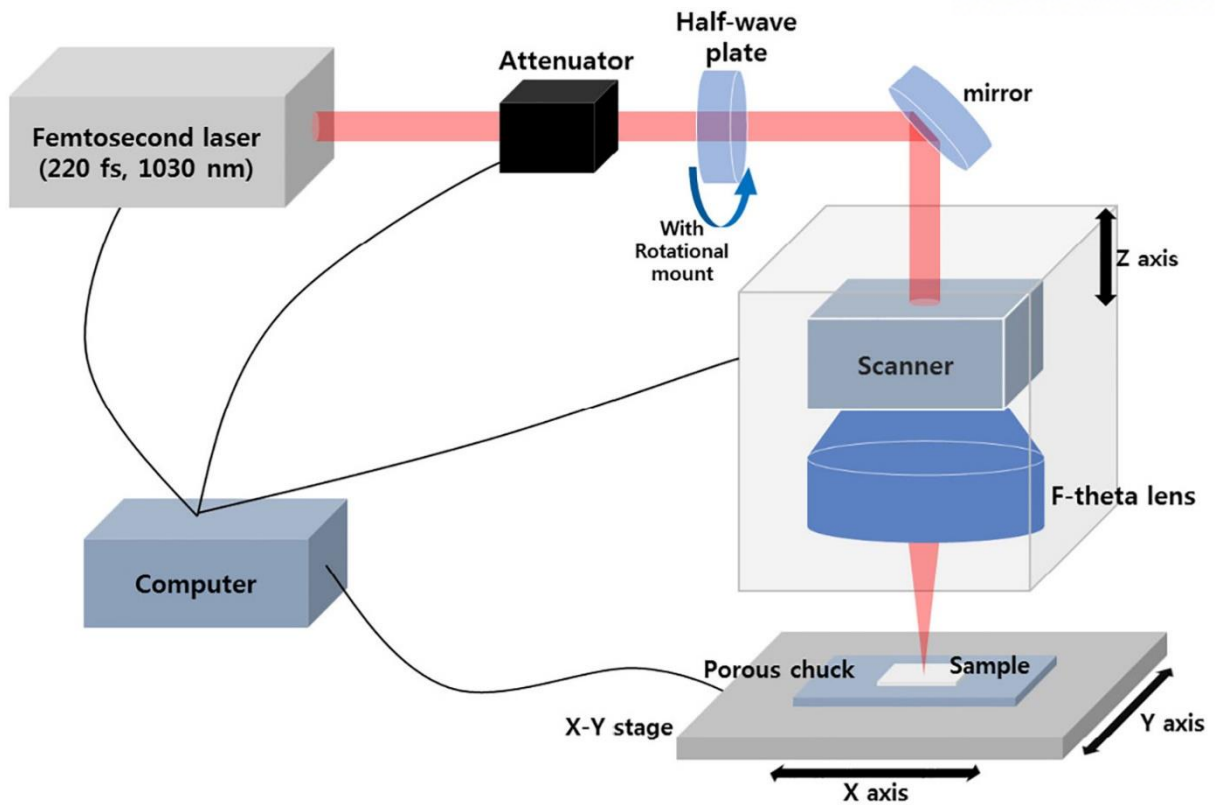


Figure 19. Schematic view of the experimental setup

In this study, 316 L stainless steel (thickness 0.5 mm) was used as the specimen material, and the beam polarization was set such that the LIPSS patterns were aligned perpendicular to the beam-scanning direction. The surface reflectance was measured at five different locations by using a UV-vis microspectrometer (CRAIC, Microspectra 121), and an averaged value was used. To observe the surface morphology, scanning electron microscopy (SEM) (FEI, Quanta 200FEG) was utilized. To investigate the effect of process parameters (laser fluence and beam scanning speed) on the surface reflectance systematically, a large process window was designed using a logarithmic scale by varying the laser fluence from 0.183 to 5.09 J/cm² and a scanning speed from 0.2 to 5.53 mm/s. The effect of shield gas on the surface oxidation was also investigated considering three types of shield gas: nitrogen, argon, and helium. Shield gas was supplied to the processing area at a rate of 50 L/min.

4.3. Result and discussion

Figure 20 presents SEM images of the patterns fabricated on stainless steel specimens, arranged in terms of laser fluence (vertical axis) and beam scanning speed (horizontal axis). As shown, fabricated patterns vary widely on the given process window as laser fluence and scanning speed are changed. Figure 20(a), the pattern corresponding to 0.963 J/cm^2 and 5.53 mm/s , shows a typical LIPSS pattern, and the period of the LIPSS was found to be approximately 950 nm , which is close to the laser wavelength (1030 nm) as expected [71]. However, the pattern shown in Figure 20(e) (corresponding to 0.183 J/cm^2 and 0.2 mm/s) also looks like LIPSS, but the lines are somewhat disconnected, and the period is only about 440 nm , which is less than half the wavelength of the incident laser.

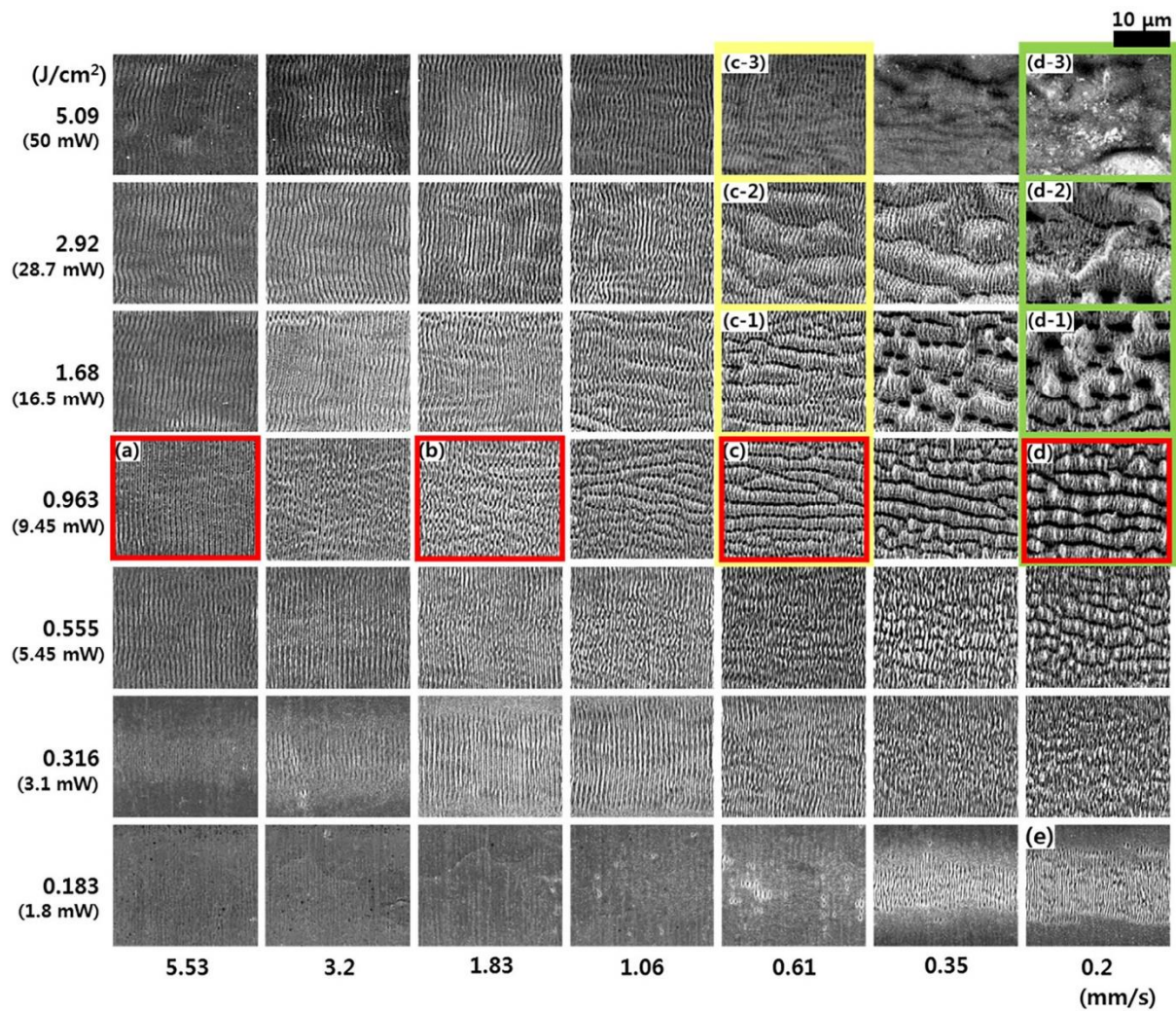


Figure 20. SEM images of the fabricated patterns arranged in terms of laser fluence (vertical axis) and scanning speed (horizontal axis).

Figure 20(a)–(d) shows how (from left to right, in red boxes) the patterns change as the scanning speed is decreased from the optimal LIPSS conditions. As shown, initially vertical LIPSS lines with a 950 nm period (Figure 20(a)) eventually become horizontal, and the width of the horizontal lines becomes wider as the scanning speed decreases (from Figure 20(a) to (d)).

To examine why these horizontal thick lines appear from vertical LIPSS lines in more detail, the four figures (Figure 20(a)–(d)) are magnified in Figure 21. In Figure 21(a), well-aligned vertical LIPSS lines are shown in the direction perpendicular to the beam polarization direction. As shown in Figure 21(b), when the scanning speed was reduced to 1.83 from 5.53 mm/s, small holes, which are deeper than the LIPSS boundary lines, were formed all over; hence, the lines became fragmented. As can be seen in the red-boxed region in Figure 20(b), the holes are aligned horizontally. However, the hole number density is not large enough; thus, the vertical LIPSS orientation is still maintained. When the scanning speed decreased further to 0.61 mm/s (Figure 21(c)), the hole number density increased significantly, and the holes were completely connected horizontally and divided the original LIPSS lines. Newly formed horizontal lines had a thickness of $\sim 2 \mu\text{m}$. As shown in Figure 21(d), with a further decrease in the scanning speed, the lines remained largely horizontal but became even thicker ($\sim 3 \mu\text{m}$). In addition, the hole number density increased even further, as shown in Figure 21(d), and the separating lines (see the region in the red box) formed from the connected holes became uniformly deep. Note that the thickness of the horizontal patterns is relatively uniform along the length direction in Figure 21(c), but in Figure 21(d), the thickness fluctuates between 1.8 and $3.2 \mu\text{m}$. The question of why the holes appear at reduced scanning speeds is beyond the scope of this study.

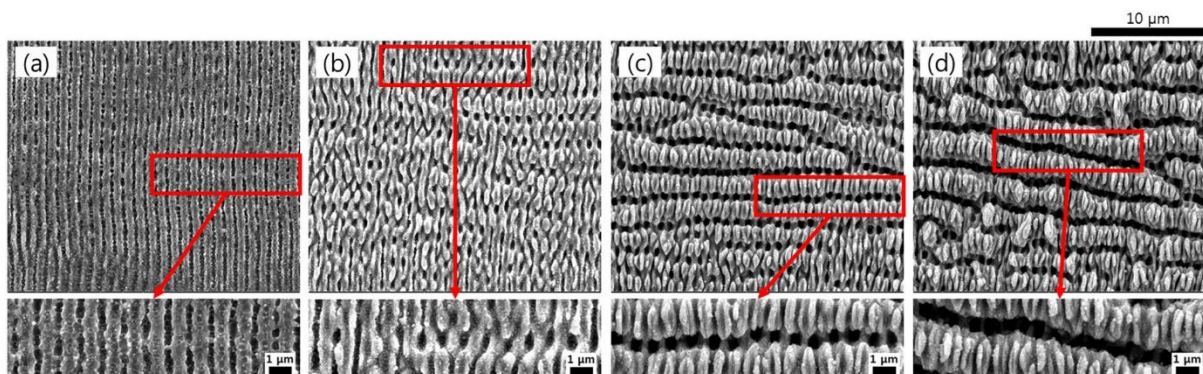


Figure 21. Magnified images of the patterns shown in Figure 20(a)–(d). From (a) to (d), the scanning speed changes from 5.53 to 1.83 to 0.61 and to 0.2 mm/s, all at the same laser fluence of 0.963 cm^2 .

In Figure 20, the images in yellow boxes show how the newly formed horizontal lines are transformed when the laser fluence increases. As shown, the thickness increased from $\sim 2 \mu\text{m}$ (at

0.963 J/cm²) to ~ 3 μm (at 1.68 J/cm²) and to ~ 5.5 μm (at 2.92 J/cm²). At the highest fluence of 5.09 J/cm², the horizontal grouping disappeared, and only vertical LIPSS lines remained.

The images in green boxes also present the change in the shape as the laser fluence increases but at a lower scanning speed of 0.2 mm/s. Similar to the images in the yellow boxes, the overall unit pattern size increased with laser fluence; however, the patterns did not remain horizontally aligned but were randomly regrouped. This non-uniformity seems to grow as the laser fluence increases; therefore, the horizontal lines cannot remain horizontal beyond a certain threshold. At 2.92 J/cm², the patterns were severely damaged, and no LIPSS-derived patterns were found. At 5.09 J/cm², the patterns were completely damaged on account of the excessive energy input.

In this study, the surface reflectance values of all the fabricated patterns (shown in Figure 20) were measured and presented as a contour plot in Figure 22. To construct the plot, reflectance values at 550 nm were used (we selected 550 nm because it is near the center of the visible spectrum). The surface reflectance of unfabricated stainless steel was measured to be 66%; however, owing to the patterns, it varied widely from 66% to 5%. Furthermore, as shown in the figure, the contour lines are mostly vertical when the laser fluence is larger than 0.183 J/cm², implying that the laser fluence minimally affects the surface reflectance. In other words, the horizontal regrouping of LIPSS patterns does not significantly affect the surface reflectance. At the lowest laser fluence of 0.183 J/cm², the surface was not greatly affected by femtosecond laser irradiation; thus, the reflection behavior was not significantly altered except at the lowest two scanning speeds (0.35 and 0.2 mm/s), where very weak LIPSS patterns were formed.

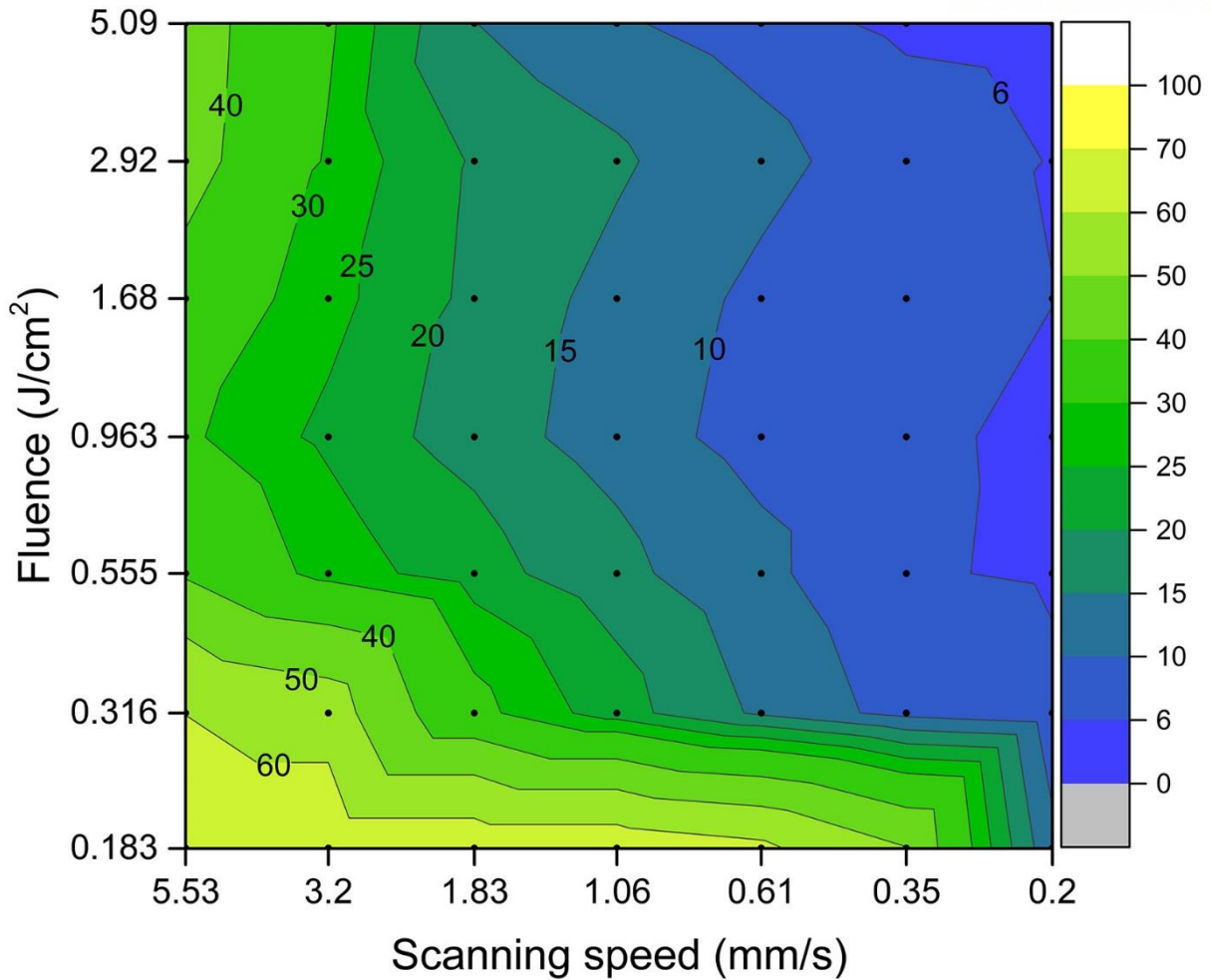


Figure 22. Contour lines showing the surface reflectance (at 550 nm) of the fabricated surfaces

Therefore, the surface reflectance varies primarily with scanning speed, as demonstrated by the vertical contour lines. As discussed earlier with Figure 20(a)–(d), an increasing number of holes are created as the scanning speed decreases. Because the holes are apparently much deeper than the initial LIPSS boundary lines, they will serve as an agent to capture light effectively. Therefore, the number density of holes is believed to be the primary factor for decreasing the surface reflectance, which explains why the contour lines are aligned vertically.

To examine the effect of scanning speed and laser fluence on the surface reflectance in more detail, the reflectance spectra of the four surfaces shown in Figure 20(a)–(d) are presented together with that of unprocessed stainless steel in Figure 23(a), and the results corresponding to a scanning speed of 0.61 mm/s (except the smallest fluence case) are shown in Figure 23(b). In both plots, the reflectance spectra from 400 to 1000 nm are presented. As shown, the reflectance increases prominently toward that of unprocessed stainless steel as the scanning speed increases (Figure 23(a)); however, it does not change much as the laser fluence increases by more than 16 times, from 0.316 to 5.09 J/cm² (Figure

23(b)). Note that in Figure 23(a), the red and black solid lines are the reflectance spectra of unprocessed stainless steel and the optimally fabricated LIPSS patterns, respectively. Overall, the reflectance increases with wavelength, and for these two cases, the increase in reflectance over the given wavelength range is greater than 25%.

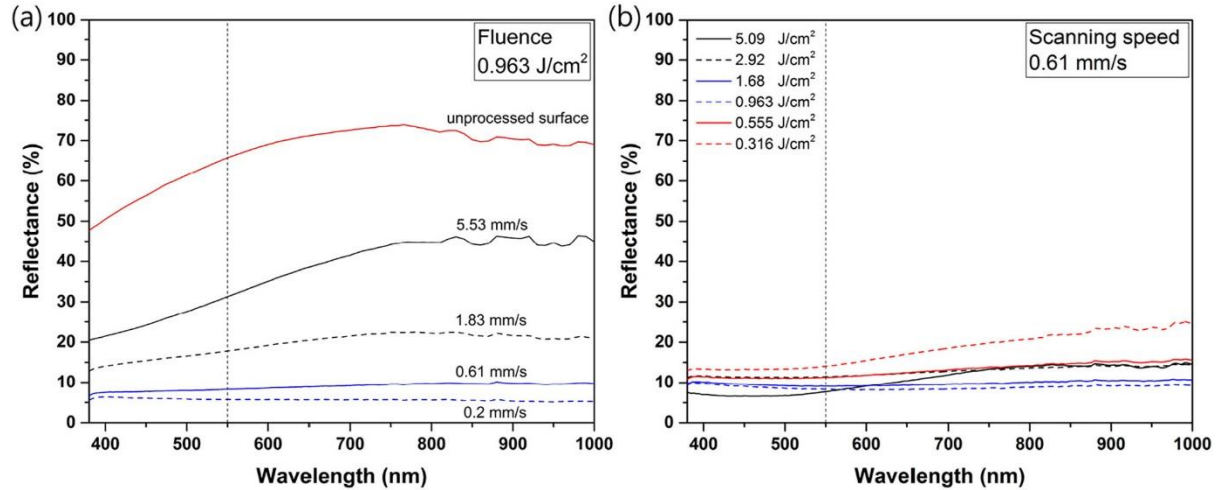


Figure 23. Change in reflectance spectra according to (a) scanning speed and (b) laser fluence.

The black dashed line in Figure 23(a) is the reflectance spectrum for Figure 20(b), where deep holes start to appear, and the light absorption capability increases substantially. In this case, the change in reflectance is less than 10%, indicating that the holes tend to reduce the wavelength dependence of the surface reflectance. As the scanning speed decreases further to 0.61 mm/s (blue solid line), the reflectance drops below 10%, and the change in reflectance becomes less than 5%. At 0.2 mm/s (blue dashed line), the reflectance spectrum curve is almost flat, and the reflectance is less than 5% over the entire wavelength range. Therefore, as more holes are formed to create horizontal patterns, both the surface reflectance and its wavelength dependence become smaller.

Using the capability of controlling the surface reflectance by varying the laser fluence and scanning speed, the authors developed a LIPSS-based laser patterning method. In this study, a multi-faceted ball was successfully fabricated on stainless steel by employing 22 surface reflectance values, and a picture taken by a camera is presented in Figure 24(b). During the fabrication, shield gas was not used. The original design of the ball is shown in Figure 24(a), and it is noteworthy that it looks somewhat different from Figure 24(b) because Figure 24(a) is based on the grayscale, while Figure 24(b) is fabricated based on the actual surface reflectance. The grayscale cannot be an exact representation of the surface reflectance because many more factors affect the surface reflectance. The multi-faceted spherical shape with a diameter of 20 mm was realized by properly choosing conditions from the surface reflectance map (Figure 22), and in Figure 24(b), reflectance values from 8% to 60% were used to pattern the ball.

Each triangular region of the ball was hatched by the laser, and the distance between the neighboring hatching lines was the width of the hatching line, which varies from one condition to another. As shown, the ball was a bit yellowish, which seems to be associated with surface oxidation or morphological change, as the patterning was conducted without a shield gas.

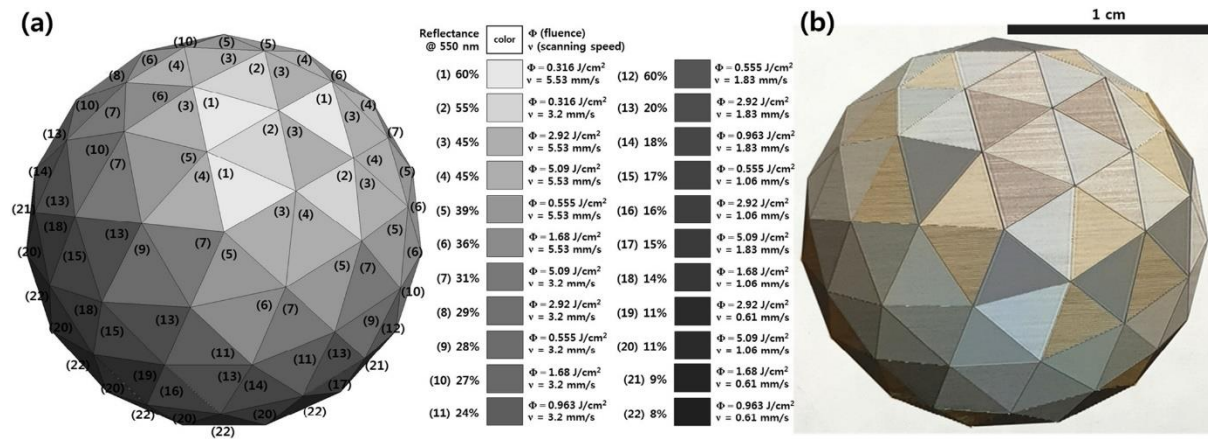


Figure 24. (a) Original design of the multi-faceted ball (b) A picture of a multi-faceted ball fabricated on stainless steel by implementing 22 surface reflectance values. The diameter of the ball is 20 mm. It is noteworthy that in part (a), the reflectance level is shown based on a grayscale, and the gray level cannot accurately represent the actual reflectance.

To study the effect of shield gas, three kinds of shield gases (nitrogen, argon, and helium) were tested, all with a flow rate of 50 L/min. Fig. 7 shows the pictures of the four patterning results obtained with nitrogen, argon, and helium gases, and the results obtained without a shield gas (Fig. 6(b)) were presented together for comparison purposes. Note that the first ionization potentials of nitrogen, argon, and helium are 14.53, 15.76, and 24.59 eV, respectively, and the ability to prevent oxidation is expected to increase in that order. For nitrogen and helium, surface oxidation was prevented effectively, and particularly in the case of helium, the yellowish color has been eliminated almost completely. Surprisingly, however, the result obtained with argon shielding is even more yellowish than the original one that was fabricated without a shield gas.

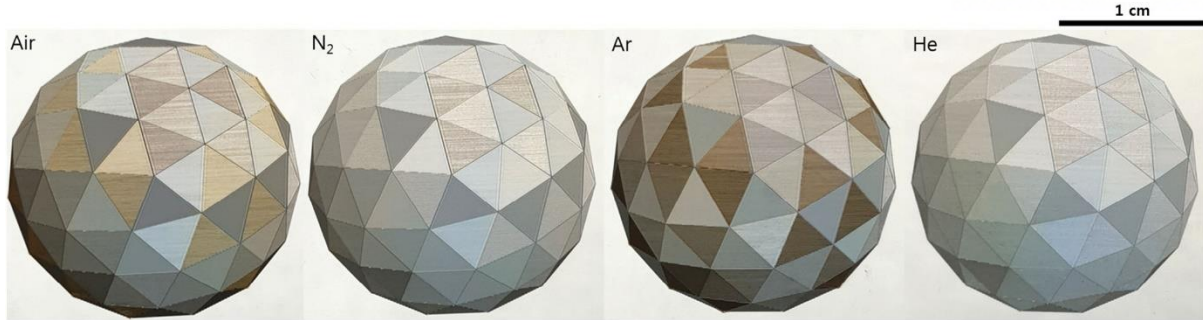


Figure 25. Pictures of multi-faceted balls fabricated under different shielding environments.

To understand why argon shielding produced the worst result, we observed the surfaces of the fabricated balls using scanning electron microscopy. Figure 26(a)–(d) are the surface SEM images of the triangular regions marked by the red points in Figure 25, which were all fabricated under the same conditions of 5.09 J/cm^2 and 5.53 mm/s . Unlike the other three cases, which exhibit clear LIPSS patterns, the surface processed with argon shielding (Figure 26(c)) was covered with dust, and the LIPSS lines looked damaged. To find the reason, a single line was fabricated for each condition as presented in Figure 26(a-1)–(d-1), and the surface morphology around the processed lines was carefully examined. We noticed that almost the entire area around the processed line was covered with dust for the argon shielding case, while the other three conditions produced fairly clean surfaces. In Figure 26(a-2)–(d-2), the magnified images of the areas shown in red boxes in Figure 26(a-1)–(d-1) are presented. We conjecture that this is partly due to the density difference of the shield gas and air: while nitrogen and helium are lighter than air and tend to float the dust particles off the surface, argon is heavier than air and can pull the flying dust particles toward the surface. Furthermore, it was reported that, in argon gas, larger particles are formed from ablation, and the dispersion of the particles is lower compared to other gases [72, 73]. Therefore, it seems that, when argon gas is used, larger particles are formed and effectively pulled down by heavy argon gas. Because the patterning of the ball was achieved by repeatedly drawing the hatching lines, the dust particles produced from one hatching line could fail the subsequent hatching lines, and this effect could accumulate as the patterning process continues.

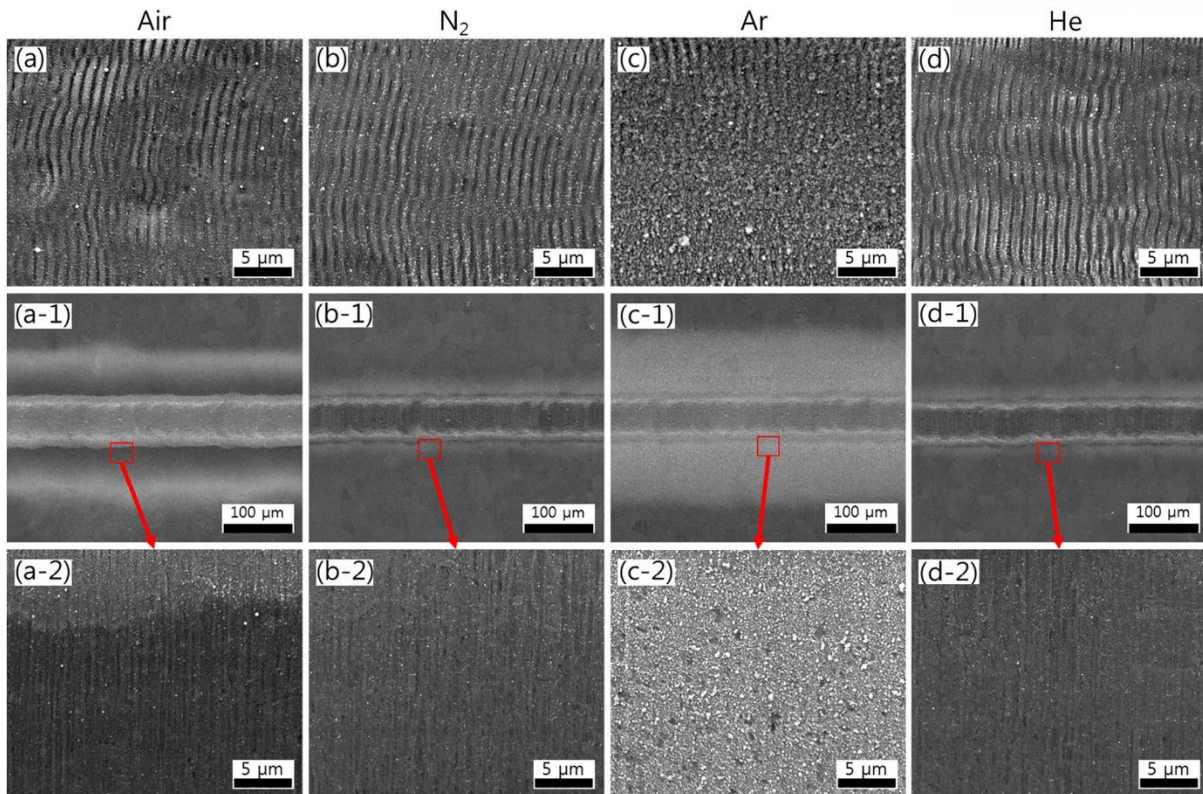


Figure 26. (Top row) SEM images showing the surface morphology at the locations indicated by the red points in Figure 25, obtained with, from left to right, no shield gas, nitrogen, argon, and helium shielding gases. (Middle row) Images of a single line fabricated under each shielding condition shown above. (Bottom row) Magnified images of the regions inside the red boxes above. (All results were obtained with the same condition of 5.09 J/cm^2 and 5.53 mm/s .)

The relationship of generated structures, surface colors of patterned surfaces, and the corresponding reflectance values (at 550 nm) is demonstrated in Figure 27. For all patterns, the employed laser fluence was 5.09 J/cm^2 , and from left to right, scanning speeds of 5.53 , 1.83 , 0.61 , and 0.2 mm/s were used. From top to bottom, the results for the different shield gases are presented. For each condition, a picture showing the surface color was taken of a $5 \text{ mm} \times 5 \text{ mm}$ region and is presented right next to the SEM image. As shown, well-shielded surfaces under nitrogen and helium environments exhibit weak and neutral colors, while no shielding (air) and argon shielding produce dark colors. Furthermore, the surface reflectance was also affected by the type of shielding, as both helium and nitrogen shield gases produced higher reflectance compared to the unshielded surfaces. Meanwhile, as expected, the argon-shielded surfaces show the lowest reflectance values. Helium shielding produced the largest reflectance regardless of the scanning speed. We believe that the variation in surface reflectance and color according to shielding type was, in part, caused by structural differences. For example, the LIPSS patterns fabricated under helium shielding were the most crisp, while the surfaces

produced under argon shielding were rough and covered with many particles, leading to a significant reduction in the reflectance induced by the scattering of light.

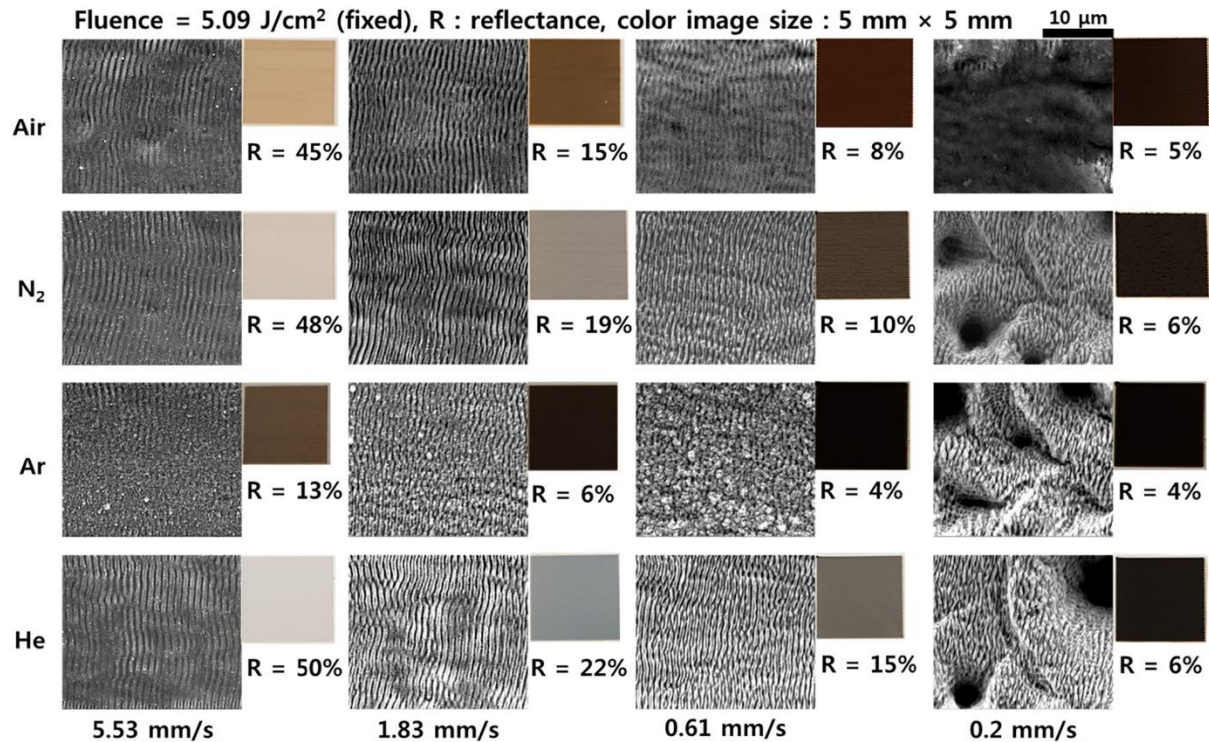


Figure 27. SEM images of generated structures, surface colors of the patterned surfaces, and the corresponding reflectance values at 550 nm. All patterns were fabricated using a laser fluence of 5.09 J/cm² and four different scanning speeds (5.53, 1.83, 0.61, and 0.2 mm/s). From top to bottom, air, nitrogen, argon, and helium shield gases were used

To study the oxidation suppression capabilities of shield gases, x-ray photoelectron spectroscopy (XPS) measurements were conducted on the four surfaces presented in the first column of Figure 27, which correspond to the condition of 5.09 J/cm² and 5.53 mm/s, and the results are presented in Figure 28. The XPS analysis was conducted on a K-alpha spectrometer (Thermo Fisher), which has an aluminum-K α source with a pass energy of 50 eV, a measuring spot size of 0.2 mm, and an energy step size of 0.1 eV. Figure 28(a) shows the Fe 2p XPS spectra of the substrates obtained by laser ablation in different shield gases. In the case of air and argon, only the Fe₂O₃ peak appeared, indicating that oxidation occurred on the surface [74, 75]. On the other hand, the Fe peak (~707 eV) was additionally identified for nitrogen and helium shielding results, which means that oxidation was partially suppressed. In the case of helium shielding, the Fe peak is larger, and the size of the Fe₂O₃ peak is reduced; thus, oxidation seems to be better prevented than in the nitrogen shielding case. Figure 28(b)

presents the XPS spectra of O 1s. As shown, the metal oxide peak is also the largest for argon shielding, as in the case of the Fe 2p spectra, implying that argon was less effective than air when it comes to shielding. The XPS results show that a large amount of oxidation took place under argon and air environments, and oxidation affected the color changes. Therefore, we can conclude that the surface darkness level is related to surface oxidation and morphological changes.

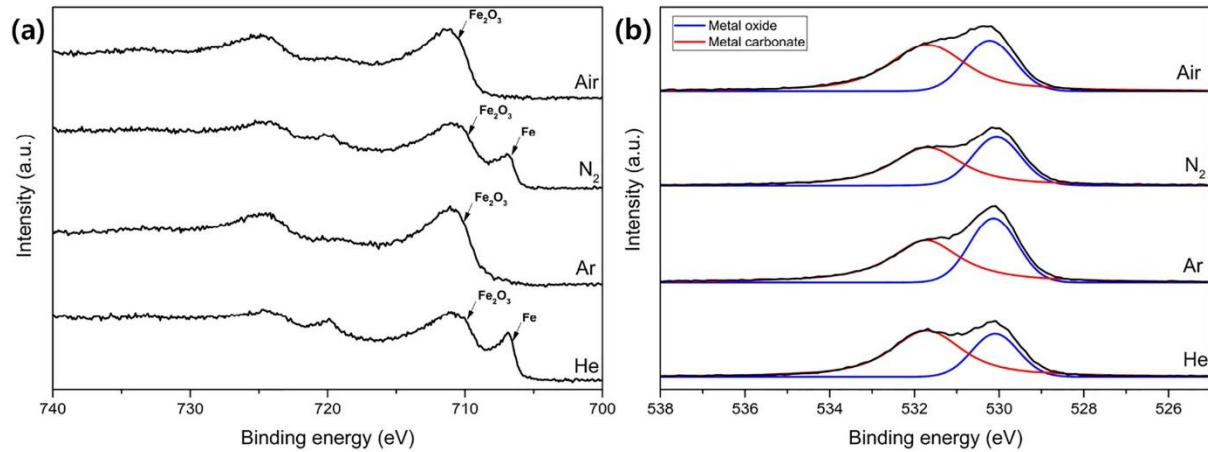


Figure 28. XPS spectra ((a) Fe 2p and (b) O 1s) of the patterned surfaces fabricated under four different shield gas environments. (conditions: 5.09 J/cm² and 5.53 mm/s).

Figure 29 presents the pictures of the four multi-faceted balls shown in Figure 25 viewed from two different viewing angles. For each shield gas condition, the fabricated ball was viewed from 40° to the left and right sides. As expected, the difference in color was observed depending on the viewing angle, because the orientation of the LIPSS lines can alter the reflection behavior of the surface. Overall, the balls fabricated under helium and nitrogen environments exhibited less dependency on the viewing angle.

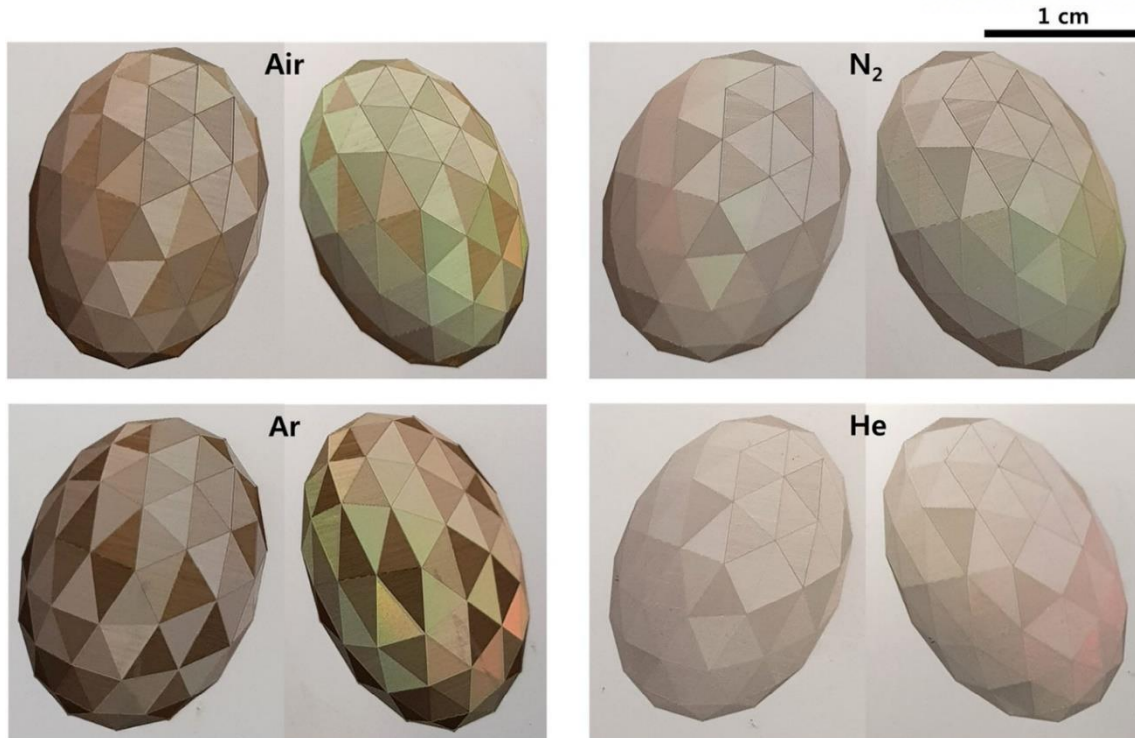


Figure 29. Pictures of multi-faceted balls viewed from different viewing angles for each shield gas condition (air, nitrogen, argon, and helium). For each shielding condition, the left and right figures were images obtained from 40° to the left and right sides, respectively.

As a final note, this study employed a low repetition rate of 1 kHz, and approximately 150 min were required to fabricate one multi-faceted ball using 22 conditions. However, the same pattern can also be constructed using a higher repetition rate. For example, when 20 kHz is used, the ball can be fabricated in approximately 8 min. Furthermore, Wang et al. recently reported the use of a cylindrical focusing lens to fabricate a large area at an extremely fast rate [76]. With this kind of method, we believe that the presented patterning method can be applied to large area patterning applications.

4.4. Conclusions

In this study, a novel femtosecond laser patterning method was successfully developed based on a systematic study of how surface morphology and reflectance change as the laser fluence and scanning speed are varied on a large process window. For stainless steel, the surface reflectance was altered nearly continuously from 66%, which is the reflectance of unprocessed stainless steel, to 5%, as the basic LIPSS pattern undergoes complicated transformations and various secondary patterns are created. This method is easy to implement and has the capability of producing elegant patterns. We believe that this method can also be applied to a variety of other materials as long as similar surface morphologies based on LIPSS can be formed.

V. ENHANCED COUPLING EFFICIENCY IN LASER WELDING OF PURE COPPER WITH CHANGES OF SURFACE MODIFICATION AND REFLECTANCE BY FEMTOSECOND LASER MICROMACHINING

5.1. Introduction

Copper is an essential material for electrical systems in various industries. In recent decades, the production and consumption of copper is growing rapidly around the world [77]. This trend has also led to advances in the processing of copper. In particular, secondary batteries have been actively researched studied recently, and the welding technology of copper is indispensable to connect internal components of batteries [78]. In the welding of copper, due to the high thermal conductivity of copper, the heat applied to the copper is easily dissipated. Furthermore, laser welding of copper is particularly difficult because of low energy absorption due to the high reflectivity for most of the wavelength. Therefore, due to the low absorption rate of copper surface to laser beam, an energy efficiency is low in the laser welding of copper and the formation of keyhole is difficult.

Many researchers have studied laser welding of copper to improve low energy efficiency. The methods are largely divided into two ways. One is the power modulation method, and the other is the modification of the surface of copper. It has been demonstrated that coupling efficiency was improved in laser welding of highly reflective materials using the power modulation method [79]. Heider et al. discussed the effect of laser power modulation on weld defects by copper welding and showed that a sinusoidal power modulation leads to a strong reduction of melt ejections and to an increase in penetration depth [80]. Heinen et al. Described laser welding of copper in lithium-ion batteries and used spatial power modulation to stabilize the welding process and show the influence of process parameters [81]. Since the power modulation method is focused on the increase in the instantaneous laser intensity, an improvement method is also needed for the laser welding of copper using a normal continuous wave.

Another promising method is the increase in the absorption rate of copper surfaces to laser beam. Engler et al. investigated the influence of the green wavelength (515 nm) and oxidized surface condition on energy coupling during heat conduction welding. The threshold power of the green laser for copper welding was lower than that of the infrared laser, with fewer melt ejection. The shape of bead appeared narrower than the infrared laser [82]. Chen et al. reported a welding method with increased absorption by spraying a nano-composite absorber over a copper surface. This method increases the efficiency of the welding process by 50% [83]. Kaierle et al. reported that the surface conditioning (oxidation and increase of roughness) of copper materials significantly increases the absorption of continuous wave

infrared laser radiation. The surface conditioning generates a reproducible coupling at the beginning of the weld seam even at low power levels [84]. Biro et al. increased absorption of pure copper surface as oxygen content in argon assist gas increased, facilitating the welding process of copper using pulsed Nd:YAG laser. However, an increase in oxygen content affects the production of oxides and the quality of the weld, and causes holes in the weld seam [85]. Daurelio et al. coated copper sheet with cupric oxide (CuO) and cuprous oxide (Cu₂O) to increase the absorption rate of laser beam to copper, and good welds was obtained accordingly [86].

As shown in the above-mentioned studies, there was no way to obtain a copper surface with very low reflectance of less than 10%, and chemical methods such as coating and surface oxidation were required. Recently, in the authors' work, a method was suggested to reduce the surface reflectance of stainless-steel with the control of the reflectance based on the processing maps using femtosecond laser patterning [3]. The lowest surface reflectance of stainless-steel was 5% using patterns method based on the laser induced periodic surface structure (LIPSS). LIPSS is a stripe pattern that occurs around a threshold fluence when a femtosecond laser is irradiated on material surface. Therefore, using this method, the surface of copper was also expected to have less than 10% reflectivity and significantly increase energy efficiency in laser welding of copper.

In this study, the variation of reflectivity of LIPSS and secondary structures fabricated on copper surface by femtosecond laser patterning was investigated and applied to laser welding. The effect of process parameters on the reflectance of patterns fabricated on the copper surface was investigated by referring to the processing map in the authors' previous work [3]. The surface of the copper specimen was patterned by a scanner to produce a surface structure with reduced reflectance on the surface of copper where welding started. The lowest of the fabricated pattern's reflectance was about 3%, and the reflectance was controllable within the range of 3 to 60%. When a pattern with a 3% reflectance was used, a keyhole was formed under a relatively low energy condition (a speed of 150 mm/s, a power of 1800 W, and a beam diameter of 187.5 μm) in the laser welding. The effect of patterning on keyhole formation at the start of welding and the change of keyhole during the welding process were investigated using the high-speed camera. The surface and cross-sectional images of welded copper specimens were also investigated.

5.2. Experimental setup

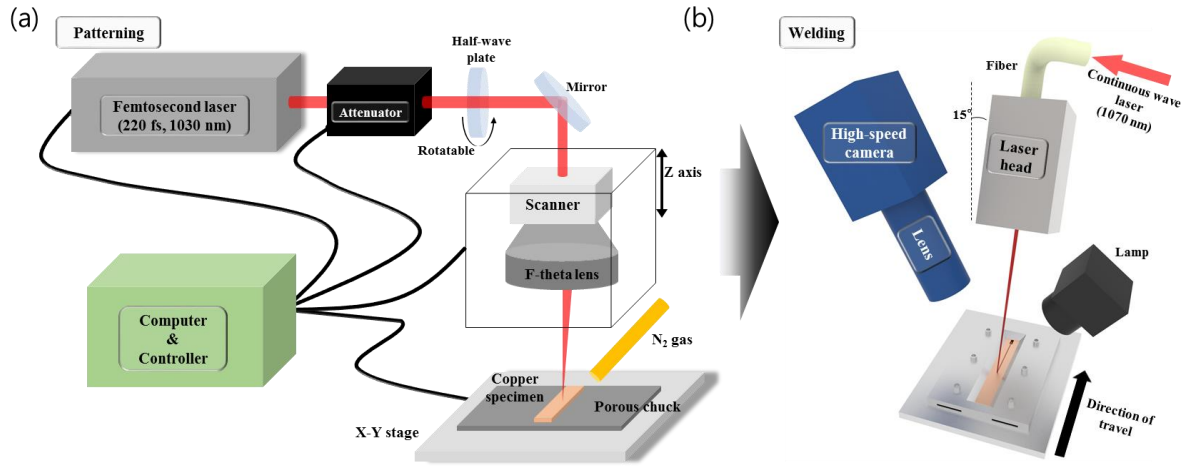


Figure 30. Schematic view of experimental setup. (a) femtosecond laser patterning process for the fabrication of the copper surface with the low reflectance. (b) observation of the surface during the welding process using a high speed camera and the welding process starting from the surface obtained in (a).

Figure 30 shows a schematic view of experimental setup. The experiment was conducted in two steps, patterning in Figure 30(a) and welding in Figure 30(b). In the patterning step, a femtosecond laser (Pharos 15-200-PP) with a wavelength of 1030 nm, a pulse duration of 220 fs, and a repetition rate of up to 200kHz was used. The maximum power of the laser was ~ 11 W at the full repetition rate (200kHz). A half-wave plate was used to control the laser polarization. It was fixed to the rotating mount to adjust the angle. The equipment for fabrication was a galvano scanner equipped with f-theta lens which has a focal length of 160 mm. The beam diameter at the focal position was about $50 \mu\text{m}$. The nitrogen gas was supplied to the process area at 50 L/min to prevent oxidation during the patterning process. Oxygen-free pure copper sheet (99.99%) was used as the specimen material, and the thickness of sheets was 1 mm. The copper specimen was fixed using a porous chuck installed on the X-Y stage, and the beam was focused on the surface before processing. To investigate the effect of process parameters on surface reflectance changes due to patterning, process window was designed using logarithmic scale by varying the laser fluence (0.316, 0.555, 0.963, 1.68, 2.92 and 5.09 J/cm^2) and a scanning speed (213.3, 118.9, 68, 39.2, 22.4, 12.8 and 7.32 mm/s). In the welding process, a continuous wave 2 kW multi-mode fiber laser (IPG YLS 2000) was used. The fiber laser had a wavelength of 1070 nm and beam profile of circular top-hat, and the maximum power on the specimen surface after passing all optics was 1800 W. Using a lens with a focal length of 300 mm, the beam diameter used in the experiment was $187.5 \mu\text{m}$. No shielding gas was used in the welding experiment. The reflectance of copper at the laser wavelength of 1070 nm was $\sim 97\%$, so the laser head was tilted to about 15° to prevent damage to the optics system. The maximum power (1800W) was only used in welding process. The specimens were moved using

linear stage, and the maximum speed was 1 m/s. In this experiment, 100, 150, 200, 300 and 400 mm/s speeds were used.

The surfaces fabricated with femtosecond laser were measured using the Scanning Electron Microscope (FEI, Quanta 200 FEG) to observe the shape of the surface. UV-vis micro-spectrometer (CRAIG, Microspectra 121) was used to measure the reflectance of each changed surface. Using a high-speed camera, the process was recorded in video at 5000 fps. In the case of video, the images were loaded and analyzed

5.3. Results and discussion

5.3.1. Reduction of reflectance of copper surface

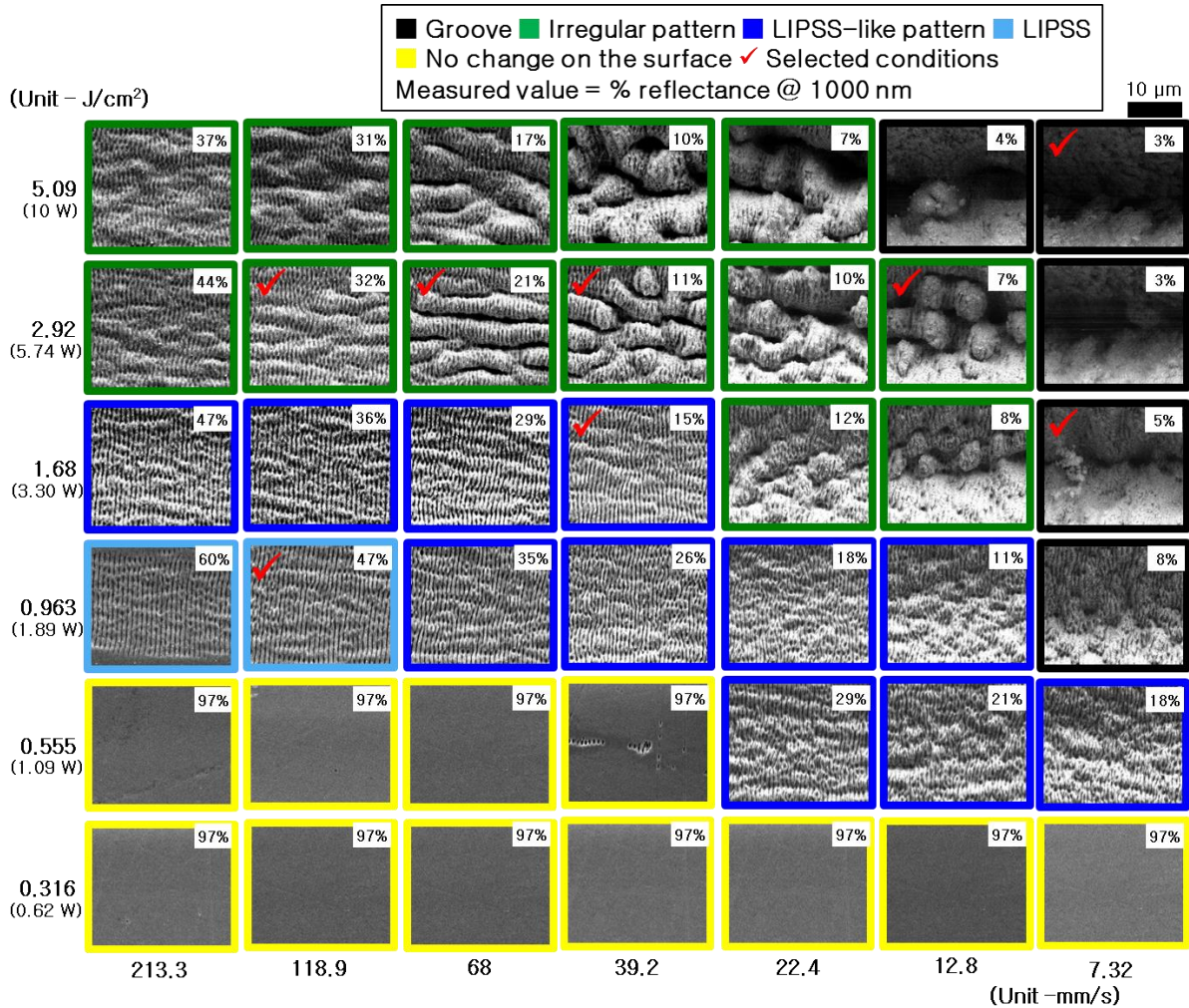


Figure 31. SEM images of fabricated copper surface. The color of the boxes indicates the classification of the surface structure. Structures with red checks are the conditions used in the experiment.

Figure 31 presents SEM images of the structures fabricated on copper specimens, arranged in terms of laser fluence (vertical axis) and beam scanning speed (horizontal axis). This experiment was designed with six fluences and seven scanning speeds. The fabricated patterns corresponding to 0.963 J/cm² and 213.3 mm/s, shows a typical LIPSS, and the period of the LIPSS was approximately ~1 µm, which is close to the laser wavelength (1030 nm).

The irregular structures were already mentioned in the authors' previous works. A similar phenomenon was found in the stainless steel [3], but there were differences. A structure in a direction perpendicular to the LIPSS direction is shown under the condition corresponding to 2.92 J/cm² and 68

mm/s. This structure has a greater period than the LIPSS. In the case of stainless steel, this structure is very evident, but in copper there has been a break in the structure. In copper, as in stainless steel, unit structures of the LIPSS adhere to each other and holes were created. The formation of holes increases the trapped light, reducing the reflectance. This phenomenon happens more irregularly as the energy going into it increases, and at low scanning and high fluence, the sharp-shaped groove was fully fabricated. In the previous paper, a very slow scanning speed was used because the repetition rate was 1 kHz. However, because the present study used a full repetition rate of 200 kHz, the copper surface was fabricated at a very high scanning speed. In the case of copper, it has very high reflectivity even for the wavelength of the femtosecond laser, 1030 nm, so that surface change is generated from higher fluence, but the fluence of the LIPSS formation is the same. However, there was a difference in the scanning speed at which the LIPSS is formed. For stainless steel, LIPSS occurred at a repetition rate of 1 kHz, a speed of 5.53 mm / s, and 0.963 J / cm². In terms of speed in order to set the distance between spots of laser, it was a very fast scanning speed of about 1 m/s. Therefore, to form the LIPSS on the surface of copper, the spacing between spots must be further reduced.

In Figure 31, the color of the box represents the classification of the surface structure and the reflectance at 1000 nm was measured for each condition. The surface reflectance of original copper was 97% at 1000 nm, and the reflectance of the fabricated surface was from 3% to 60%. The black boxes had a reflectance of less than 5% under the condition obtained by the fully fabricated groove. The light inside the groove is reflected several times on the sidewall of the groove, thereby reducing the reflectance of the surface. The sky-blue boxes are conditions in which LIPSS is formed near the threshold area. LIPSS appears in very small areas near the threshold area under conditions formed by surface plasma polariton (SPP). Blue boxes are a condition in which LIPSS is partially formed, but more energy put into the surface than the condition where LIPSS is formed, causing the LIPSS pattern to be crushed and distorted. In the conditions of the green boxes, more distortion and deformation of the pattern was made with more energy than with the blue conditions. The reflectance decreased as the portion of the deep region increased. Among the conditions obtained, eight different structures were used for laser welding of copper.

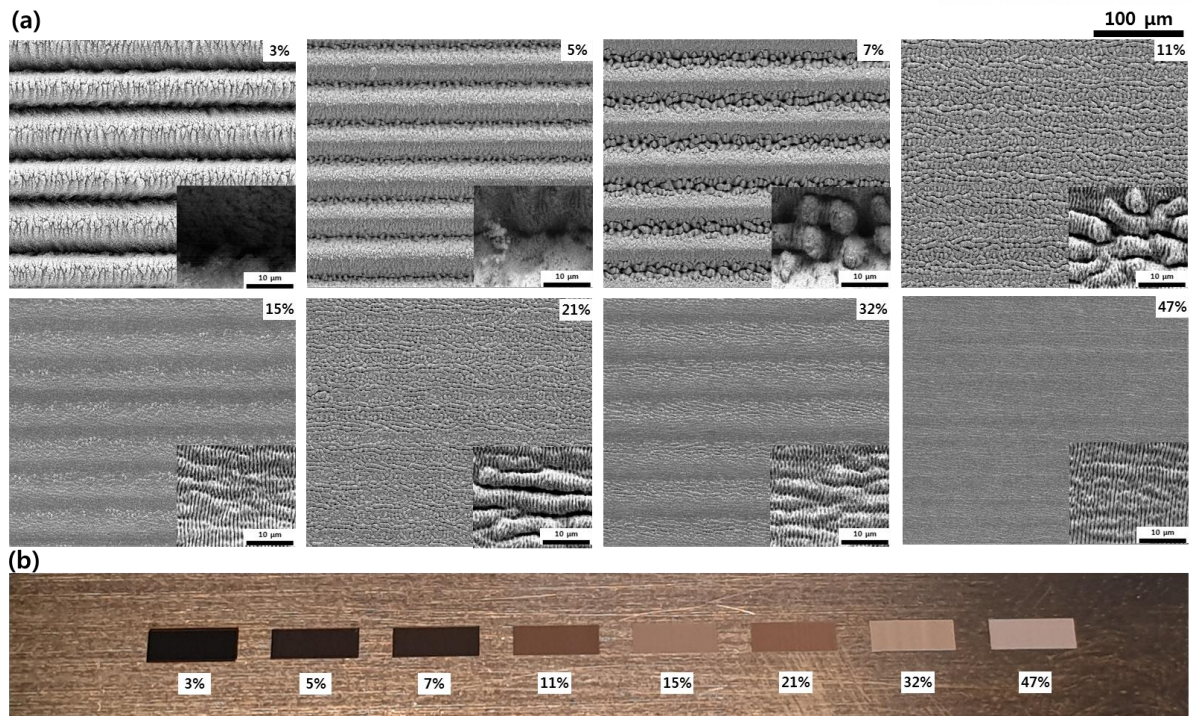


Figure 32. (a) SEM images of patterned area (b) color images of patterns according to reflectance.

Figure 32(a) shows a SEM photograph of a 2 mm x 5 mm patterned area on the copper surface. Hatches were placed in the area, and the spacing between each hatch line was set to width of one fabricated line. The spacing between the lines was not very different. It had a value between about 40 and 50 μm. However, the difference in depth of fabricated pattern on the surface was obvious. As shown in macroscopic SEM images, as the reflectance increased, the patterns became denser and shallower. This suggests that when the laser beam is irradiated, the effect of the beam trapping on the surface increases as the depth of the structure increases. Figure 32(b) shows a photograph of a processed pattern, and the difference in reflectance was clearly seen. In the patterning, since nitrogen gas was used to prevent oxidation of copper, oxidation did not occur and the color of the patterned surface did not change to an oxidized color, and the contrast was well expressed according to the reflectance. The pattern was fabricated at the start of welding on a copper specimen having a width of 3 cm, a length of 13 cm and a thickness of 1 mm. As shown in Figure 33 on the right, the specimen was fixed and used to start from the center of the pattern.

5.3.2. Welding of copper

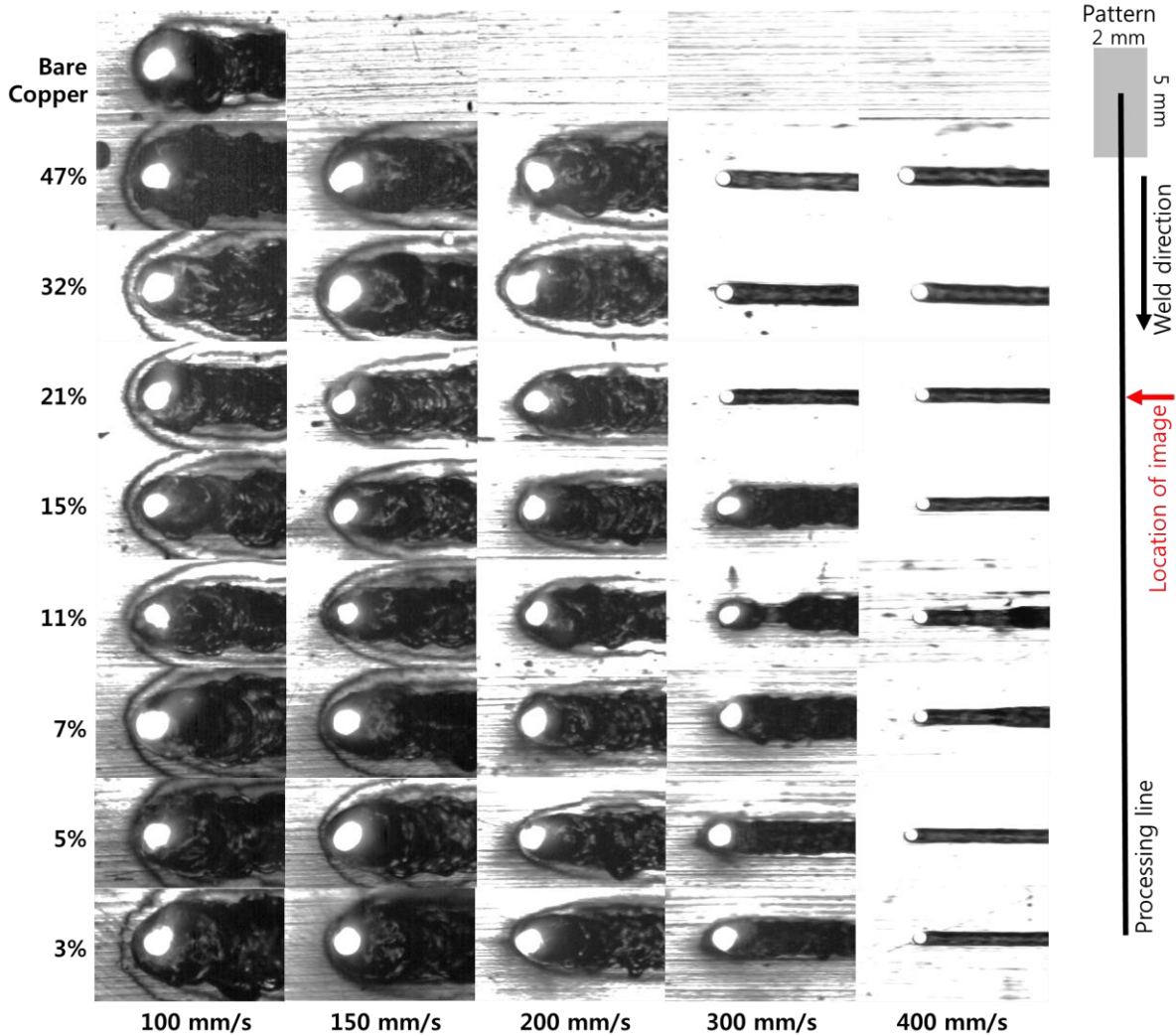


Figure 33. High speed camera images according to processing conditions.

In order to improve keyhole formation at the start of the welding, a 2 kW fiber laser was used. As shown in Figure 33 for the laser welding, five speed levels (100, 150, 200, 300, and 400 mm/s) and nine reflectance levels (3, 5, 7, 11, 15, 21, 32, and 47%) were selected and a total of 45 experimental conditions were used. A power of the fiber laser used in the experiment was fixed at 1800 W, because a keyhole formation did not occur under all power levels below 1800 for all reflectance levels. The results obtained for each condition in Figure 33 are instantaneous images of keyhole behavior welding process at one frame in the video recorded at 5000 fps using high-speed camera. In the right part of Figure 33, the schematic welding processing line is presented. The pattern was placed at the region where the laser beam was firstly irradiated on the surface of copper, and the welding was carried out in a total length of 9 cm. First, in Figure 33, experiments were conducted on bare copper surfaces, and a keyhole was

formed at speed levels below 100 mm/s, but a laser beam coupling to the copper surface did not occur at higher speed levels than 100 mm/s. At 100 mm/s, the keyhole was formed even for the reduced reflectance levels, and the behavior of the keyhole during the welding process was similar. A keyhole was formed only on the patterned specimens at speed above 150 mm/s. Although a keyhole formation was observed at three speed levels (150, 200, and 300 mm/s), welding proceeded in conduction mode at high reflectance levels using a speed of 300 mm/s. At 400 mm/s, the conduction mode welding process was also observed at all reflectance levels due to the low energy input due to the high speed. Therefore, the maximum speed at which a keyhole was formed was 300 mm/s, which is three times faster than the speed of 100 mm/s at which a keyhole was formed on the bare copper surface.

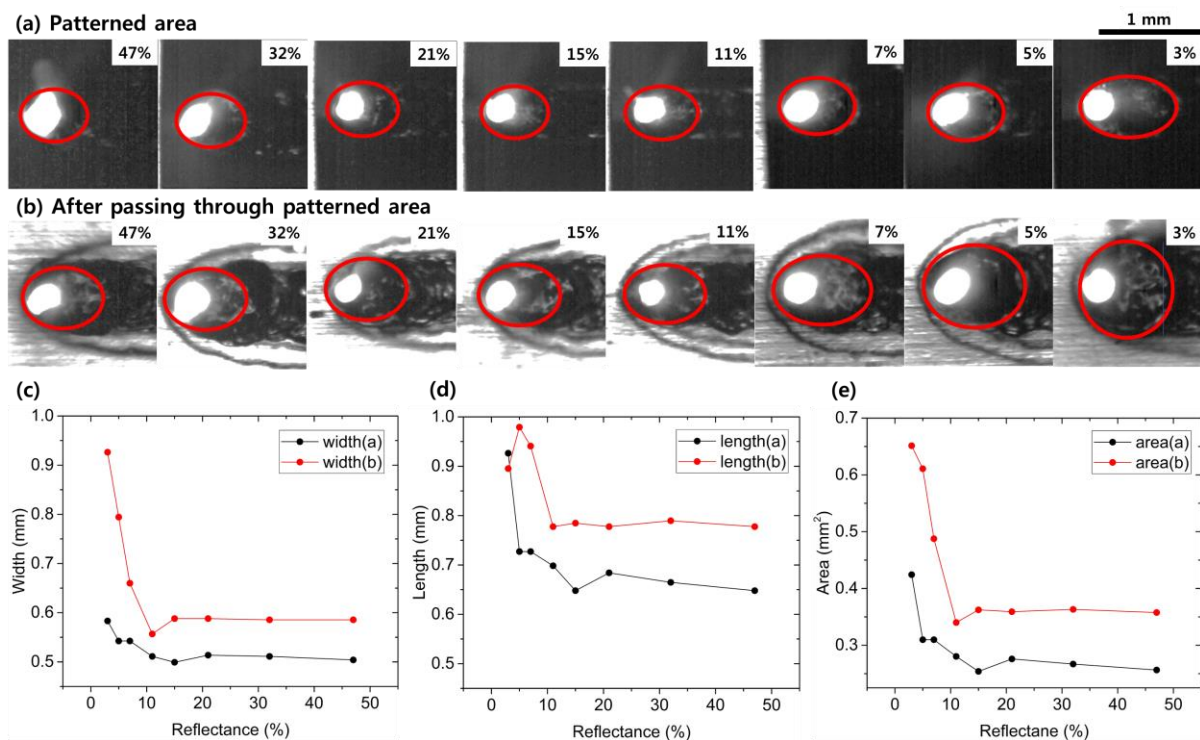


Figure 34. High-speed camera images of (a) a patterned surface and (b) a surface after passing through patterned area for seven reflectance levels (3, 5, 7, 11, 15, 21, 32 and 47%) at 1800 W and 150 mm/s (c) Relationship between reflectance and dimensions ((c) width, (d) length and (e) area) of melt pool in (a) and (b).

To investigate the relationship between a reflectance and a keyhole, high-speed camera images were compared at 150 mm/s, which is the condition where a keyhole occurred at all reflectance levels. Figure 34(a) is a set of images of the surface coupled with the laser on the patterned surface, and Figure 34(b) is a set of images when the laser is irradiated on the bare copper surface after passing through the patterned surface. The red ellipses shown in Figure 34(a) and (b) represent the boundaries of the melt

pool. The white part in the ellipse is the point where the laser beam is irradiated. Using the images of the high-speed camera in Figure 34(a) and (b), the width, length and area of melt pool were obtained, and graphs of the relationship between the dimensions and reflectance is shown in Figure 34(c), (d), and (e). The relationship between the melt pool width and the reduced reflectance is shown in Figure 34(c). The black line is the width of the melt pool in Figure 34(a) and the red line is the width of melt pool in Figure 34(b). In both cases, the width tended to increase with decreasing reflectance with similar trends, but the values of the melt pool width after passing through the pattern were greater at all reflectance condition and the width increased significantly below 10% reflectance. Figure 34(b) and (c) are graphs of length and area, respectively, and indicates that larger melt pools area formed at less than 10% reflectance. Since the size of the melt pool is proportional to the amount of energy absorbed, the fabrication of a copper surface with a reflectance of less than 10% is a very beneficial method for increasing energy efficiency in laser welding of copper.

In Figure 34 (c), (d) and (e), there was a difference in the size of the melt pool for the patterned and unpatterned areas. In the patterned part, the smaller melt pool was thin and long, but on the surface after passing through the pattern, the melt pool widened in all directions. Since the laser and copper have already been coupled in patterned part, the melt pool was still present after the pattern has passed, but the size was larger due to a high thermal conductivity of copper. The expansion of the melt pool did not occur on the pattern because the laser beam penetrated deeper due to the high absorption rate, so that more energy was transferred in the depth direction than in width direction.

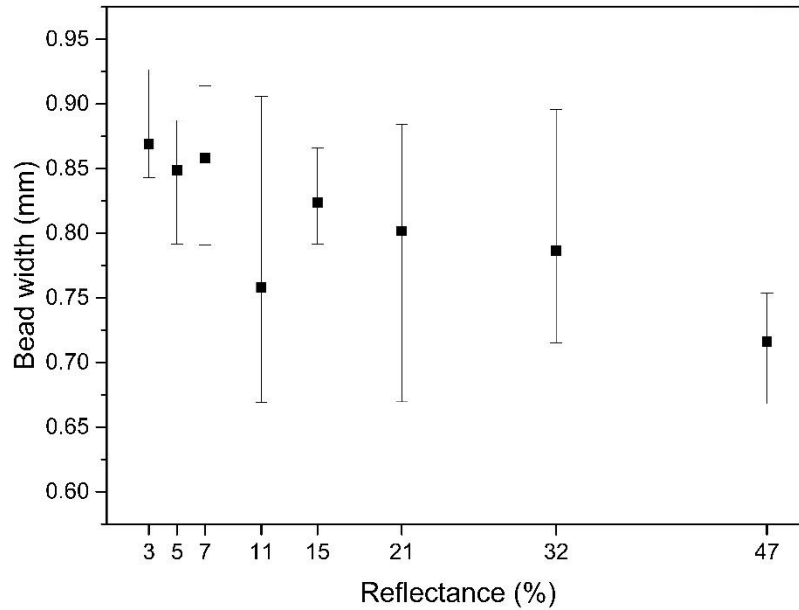


Figure 35. Variation of bead width according to reflectance of pattern. ($P = 1800\text{W}$, $v = 150\text{ mm/s}$)

Figure 35 shows variation in bead width corresponding each reflectance level. An average of the bead widths measured in five different locations for each condition. In addition, the highest value in the error bar is the measured maximum value and the minimum value is the measured minimum value. In general, the higher laser power and slower the weld speed are irradiated on the surface, the more bead width increases. As shown in Figure 35, the width of bead decreased as the reflectance increased. The change in bead width tended to be similar to the change of melt pool size, but the increase was not significant at less than 10% reflectance. This is because the instability of the bead width due to the fluctuation of melt pool. In this experiment, since the shielding gas was not used during the welding process, the surface tension of the melt pool was lowered. Therefore, the shape of bead was unstable.

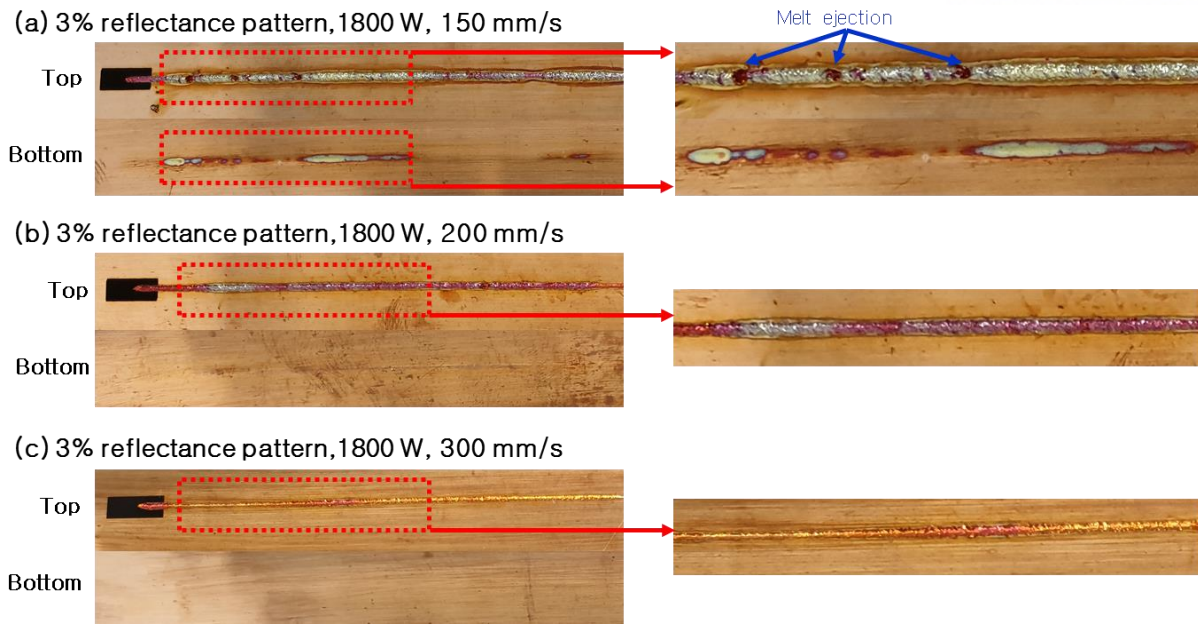


Figure 36. Top and bottom view of welded copper surface using 3% of reflectance pattern and power of 1800 W and scanning speed of (a) 150 mm/s, (b) 200 mm/s and (c) 300 mm/s

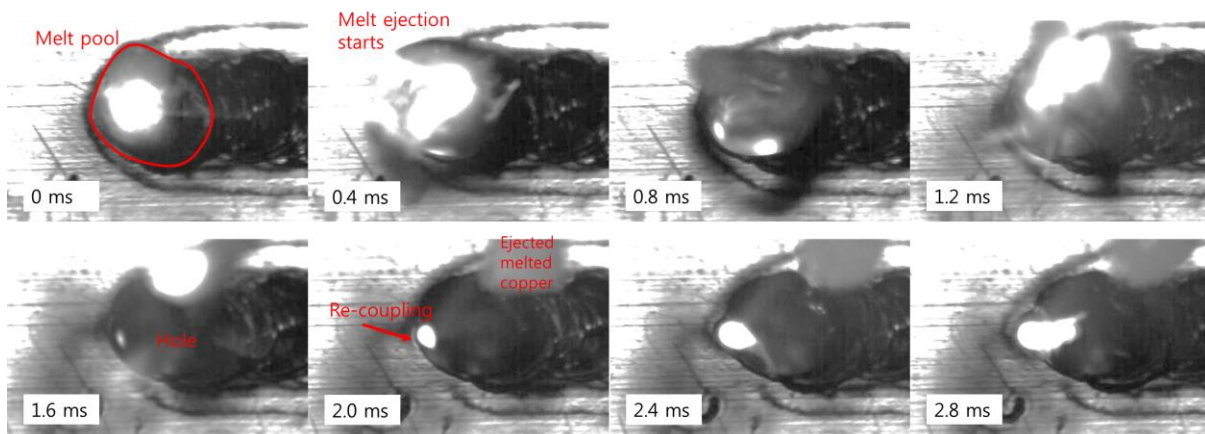


Figure 37. High-speed camera images taken at intervals of 0.4 ms from the area where melt ejection occurs

Figure 36 shows images of the top and bottom surfaces irradiated with a power of 1800 W and three speed levels (150, 200 and 300 mm/s) on a copper specimen using fiber laser. Results using a power of 1800 W and a speed of 150 mm/s showed some holes in the welded bead on the upper surface. The holes were created by melt ejection. Melt ejection phenomenon is described as caused by a vapor bubble [87, 88]. The general keyhole was observed at the beginning of weld processing, but vapor bubbles were formed inside the melt pool by the bending of the keyhole at a specific speed. This vapor

bubble made the melt pool unstable, pushing it out gradually. When the vapor bubbles have more pressure than the surface tension of the melt pool, the molten liquid part is released. Figure 36(a) shows a few defects in the bead, and there were three holes. Figure 37 shows high-speed camera images of the melt ejection at 0.4 ms intervals for first hole in Figure 36(a). After the weld pool was shaken, the entire weld pool came out. In Figure 36(b) and (c), no melt ejection occurred in the welding results using the speed levels of 200 and 300 mm / s.

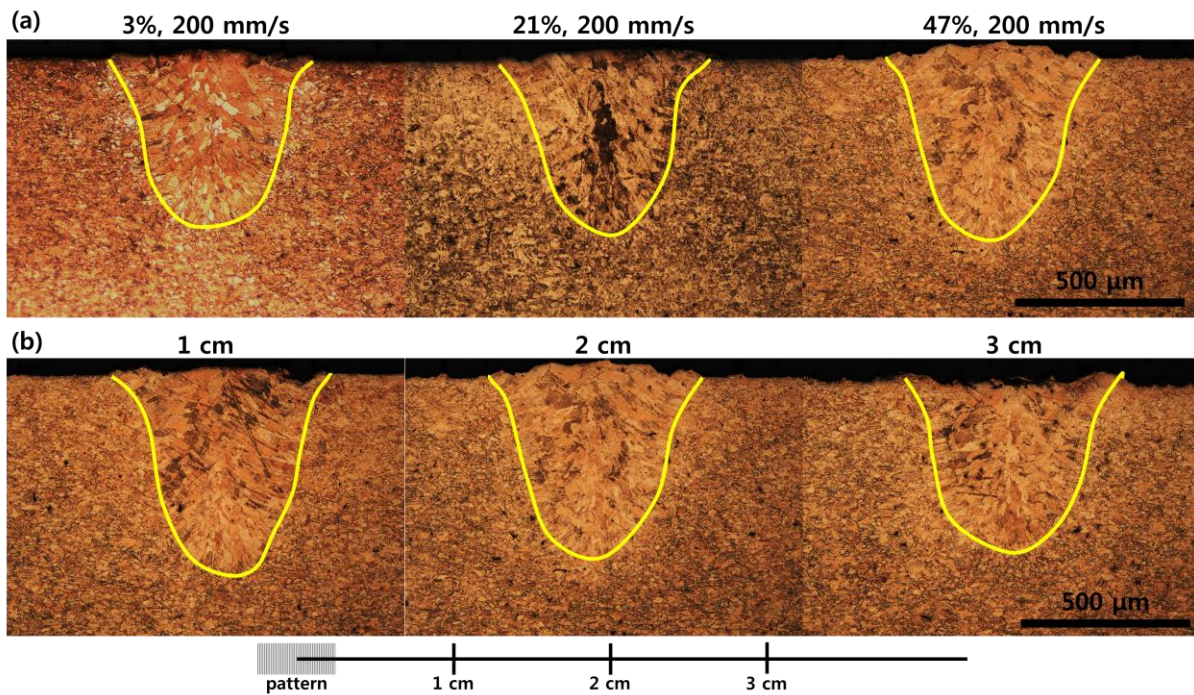


Figure 38. (a) cross-section image of the results using different reflectance values (3%, 21%, and 47%) under the same process conditions (1800 W, 200 mm/s) (b) cross-section images at different positions (1 cm, 2 cm, and 3 cm) under the same reflectance (47%) and process conditions (1800W, 200 mm/s)

Figure 38 shows cross-sectional images of the results tested at a power of 1800 W with scanning speeds of 200 mm/s. In copper welding, the cross-section of the weld has three distinct area depending on the temperature [88]. There is a fusion zone (FZ) in the center of the weld seam with a large grain size. The yellow lines in Figure 38 are the boundaries of FZ. In FZ, there are two areas with different grains directions. The longitudinal columnar (LC) grains are in the center of the weld seam, and the horizontal columnar (HC) grains are on both sides. There is a heat affected zone (HAZ) on the outside of the FZ. Due to the high thermal conductivity of copper, the HAZ cools quickly and has grains that have smaller size than the grain size of the FZ. The base material, located on the outermost side, has the

finest grain. There is also a difference in the size of the grain in the FZ. The base material, located on the outermost side, has the finest grain. Figure 38(a) shows cross-sectional images of results using patterns with different reflectance values (3%, 21%, and 47%) under the same process conditions (1800 W and 200 mm/s). As the reflectance of the pattern was decreased, the penetration depth and width were expected to increase, but the changes were very irregular, and tendency was not clear. However, as shown in Figure 38(b) there was a difference in penetration depth at different positions of the same result. A result of using the process conditions (1800 W and 200 mm/s) on the pattern with 47% reflectance showed that the depth decreased as the distance from the pattern increased. This is thought to be caused by the heat of the melt pool being rapidly dissipated by the high thermal conductivity of copper. To better understand the trends in Figure 38(a) and (b), measurements were made under different conditions and the measurements are shown in the graph in Figure 39.

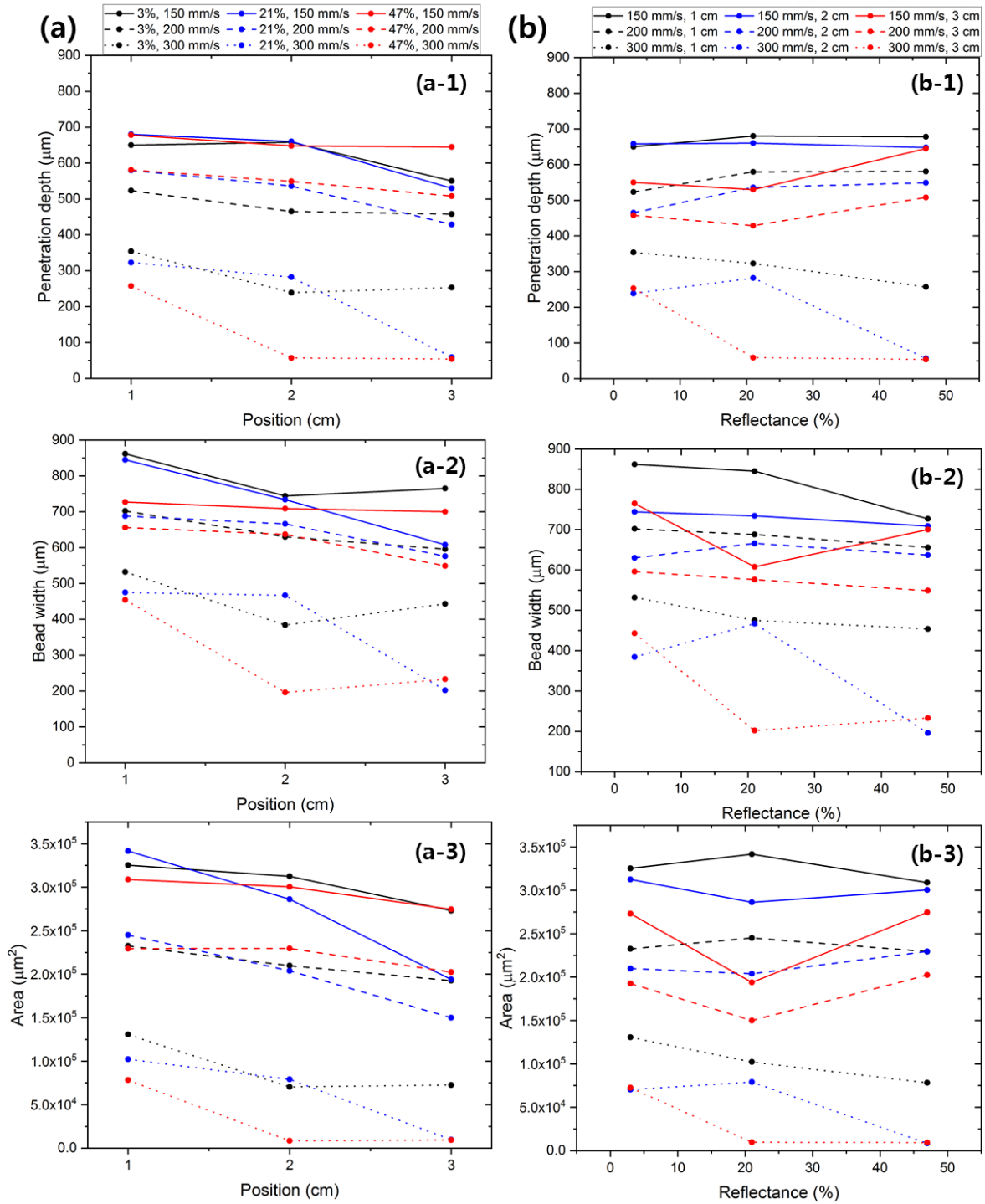


Figure 39. (a) graphs showing measurements of (a-1) bead width, (a-2) penetration depth and (a-3) area over distance from pattern. (b) graphs showing changes in (b-1) bead width, (b-2) penetration depth, (b-3) area as the reflectance of patterns changes.

Figure 39 shows graphs of changes in the bead width, penetration depth, and area of the weld under different conditions. In Figure 39(a), the black line shows the patterns of 3% reflectance, the blue line shows the pattern of 21% reflectance, and the red line shows the pattern of 47% reflectance. The

shape of the line represents the welding speed, the solid line represents 150 mm/s, the dashed line represents 200 mm/s, and the dotted line represents 300 mm/s. Figure 39(a-1) is a graph showing the change of penetration depth according to the distance from the patterns. As the distance from the pattern increases, the depth generally decreases. The average difference between the depth at 1 cm and the depth at 2 cm was about 60 μm . The average difference between the depth at 1 cm and the depth at 3 cm was about 130 μm . Figure 39(a-2) is a graph showing the width values according to the distance. Like penetration depth, bead width also decreased with distance. Therefore, as shown in Figure 39(a-3), the area is also reduced overall. At speeds of 300 mm/s, the amount of reduction with distance was much greater than for other speed conditions. Excluding these values, the depth of the 2 cm point was reduced by 5% and the width decreased by about 8% for the depth of the 1 cm point. However, at 3 cm, both values decreased by about 15%. Therefore, if a new pattern is created and connected at the 2 cm point, the welding may proceed while maintaining a size difference of less than about 10%. Fig. 10 (b) shows the change of dimensions of welded area according to reflectance. The values of penetration depth of 150 mm / s and 200 mm / s increased slightly as reflectance increased, and decreased at 300 mm / s. In the case of width, the width decreased as the overall reflectivity increased. Therefore, in case of area, the area of 150 mm / s and 200 mm / s was maintained to be similar, and in the case of 300 mm / s, the area was clearly reduced. At 200 mm / s, appropriate dimensions and changes were confirmed, and uniform welding was attempted through the pattern of 2 cm intervals.

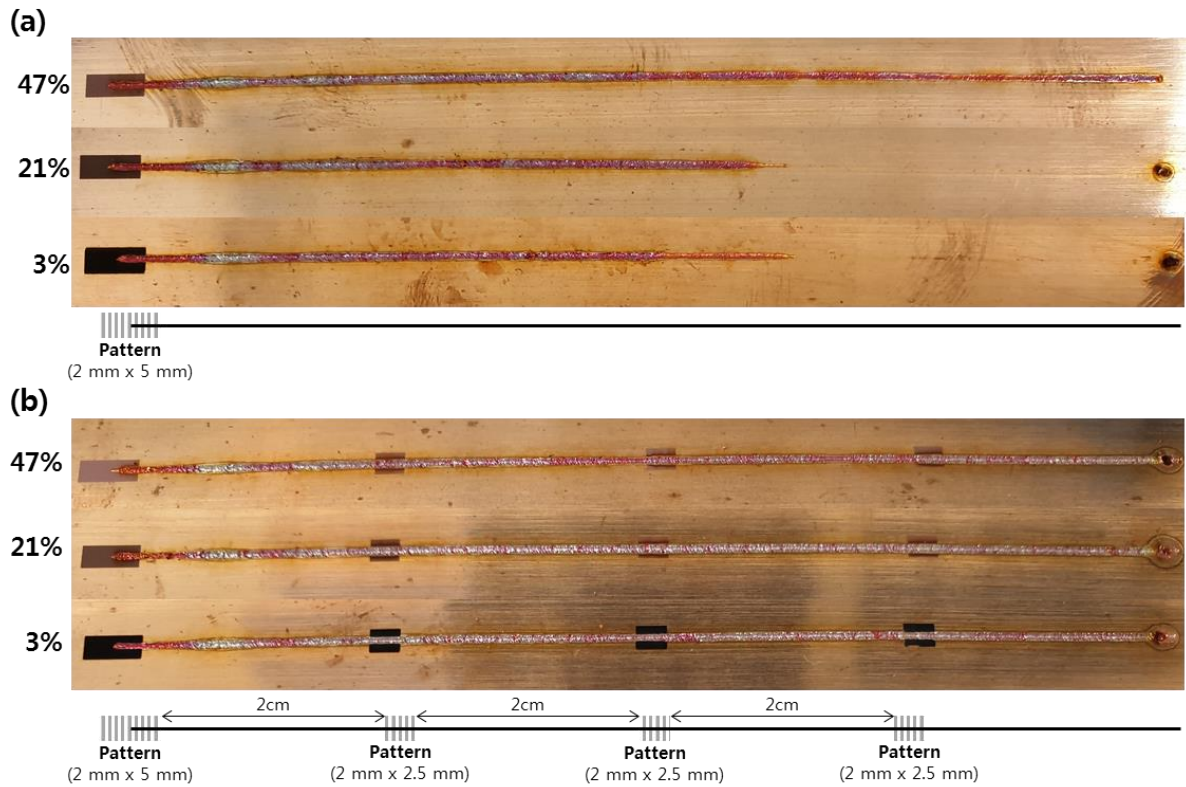


Figure 40. . A Top view of results using welding process conditions of 1800 W and 200 mm / s. (a) welding results obtained by fabricating patterns with reflectance of 3%, 21% and 47% only at the beginning of the weld. (b) welding results obtained by machining patterns with reflectances of 3%, 21%, and 47% at 2 cm intervals.

Figure 40 is a top view of the weld results using a power of 1800 W and a scan speed of 200 mm / s. Figure 40(a) shows the results of fabricating the pattern only at the beginning of welding. The patterns which has 3%, 21%, and 47% of reflectance were used and the total length of welding was 9 cm. As mentioned in Figure 40, as the distance from the pattern increases, the depth becomes shallower and the keyholes disappear. Using the patterns of 3% and 21% reflectivity, the keyhole disappeared at about 6 cm, and the result of the 47% reflectivity pattern continued to the end but became thinner. Therefore, in order to prevent this phenomenon, the pattern was fabricated every intermediate part on the welding progress line. In Figure 39, the distance between the patterns is 2 cm, so the depth reduction is small, so the pattern spacing is set to 2 cm. Figure 40(b) shows the welding result of pattern processing at 2 cm intervals. For all reflectance conditions the weld proceeded to the 9 cm long end.

5.4. Conclusions

In this study, the method of changing the surface reflectance of pure copper using femtosecond laser patterning, which improves laser beam coupling to copper surface for keyhole formation in laser welding of copper, was introduced. By precisely controlling the surface reflectivity, the pattern with a reflectivity of 3% was easily made within 30 seconds of the copper surface, and the weld speed needed to form the keyhole in the pattern was 300mm/s, three times faster than the bare surface. However, stable keyhole formation and depth retention were 200 mm / s speed conditions, and the pattern was processed at 2 cm intervals to increase the stability of the weld. This method will increase the efficiency of the laser welding process of copper and it is also expected to be readily applicable to laser welding of other highly reflective materials such as aluminum.

VI. CONCLUSIONS AND FUTURE WORK

6.1. Conclusions

In this dissertation, laser surface modification was used for optical and joining applications. The first chapter described the motivation for this work and the processes associated with laser surface treatment used in the next chapters, and also included the basic background. Chapter 2 described the graphenization of DLC film using laser annealing and PLD process. Using PLD, DLC film was deposited on glass, and deposited DLC film is changed thermally. The internal structure of the film has changed. It was confirmed that the sp^2 bonding content was increased after annealing. By measuring the transmittance and sheet resistance of annealed film, we found the possibility of being used as a transparent conductive film. Although the change to a complete graphene was not achieved, it was approached to specifications that could be used for transparent conductive electrodes. Chapter 3 describes how to improve the results obtained in chapter 2. Picosecond laser was used for patterning. Only the thin film of the surface was removed with certain pattern, increasing the transmittance. The increased sheet resistance with patterning was reduced by the etching process. It was confirmed that the sheet resistance and transmittance were improved, and the simple calculation based on the map showed predictability. This method is thought to be applicable to a variety of transparent conductive films, and if patterning and etching are optimized, the film's performance will be further improved. Chapter 4 showed the change of the reflectance of surfaces using LIPSS. LIPSS was fabricated using the stainless steel, and the reflectance of fabricated structures, including LIPSS, was also measured according to the process conditions. Reflectance was controllable according to process parameters and, using measured results, a sphere was represented on the stainless-steel surface. Chapter 5 shows the joining application of copper materials through the change of surface reflectance. The pattern was fabricated on the copper surface using femtosecond laser to reduce the reflectance so that the absorption rate for the laser beam could be increased. As a result, coupling could occur in lower energy than on a general copper surface.

6.2. Future work

The studies in this paper were still a basic process. In the case of transparent conductive film, the carbon structure was changed by laser annealing using DLC film deposited at room temperature and 900 °C. For DLC film, the contents of the internal sp^2 and sp^3 bonds will vary depending on the surround temperature when depositing. It is thought that if the original DLC film has relatively high sp^2 content, it might be possible to make graphenization of film with smaller heat during laser annealing. The deposition temperature also needs to be optimized. The second topic, improvement of the performance of the film through patterning and etching, requires optimizing it. Although we increased transparency by using two basic types, square and circular patterns, we believe that using optimized patterns will minimize the decrease in electrical conductivity when increasing transparency. In the LIPSS study, the reflectance was controlled by constant patterns obtained when laser was irradiated in a straight line. However, using the phenomenon of LIPSS being made, it is thought that more different results could be obtained if various machining directions and angles were applied to the surface of the material with a shorter wavelength of laser. For example, a surface with unique properties, such as meta-surface, may be obtained.

REFERENCES

- [1] K. Lee and H. Ki, "Rapid fabrication of transparent conductive films with controllable sheet resistance on glass substrates by laser annealing of diamond-like carbon films," *Acta Materialia*, vol. 111, pp. 315-320, Jun 1 2016.
- [2] K. Lee and H. Ki, "Fabrication and optimization of transparent conductive films using laser annealing and picosecond laser patterning," *Applied Surface Science*, vol. 420, pp. 886-895, 2017/10/31/ 2017.
- [3] K. Lee and H. Ki, "Femtosecond laser patterning based on the control of surface reflectance," *Applied Surface Science*, vol. 494, pp. 187-195, 2019/11/15/ 2019.
- [4] M. Qian *et al.*, "Formation of graphene sheets through laser exfoliation of highly ordered pyrolytic graphite," *Applied Physics Letters*, vol. 98, no. 17, Apr 25 2011, Art. no. 173108.
- [5] J. B. Park *et al.*, "Fast growth of graphene patterns by laser direct writing," *Applied Physics Letters*, vol. 98, no. 12, p. 123109, 2011/03/21 2011.
- [6] L. Fan *et al.*, *Laser direct writing of graphene patterns on SiO₂/Si substrates* (SPIE LASE). SPIE, 2013.
- [7] W. Xiong *et al.*, "Direct writing of graphene patterns on insulating substrates under ambient conditions," *Scientific Reports*, vol. 4, no. 1, p. 4892, 2014/05/08 2014.
- [8] D. Wei and X. Xu, "Laser direct growth of graphene on silicon substrate," *Applied Physics Letters*, vol. 100, no. 2, Jan 9 2012, Art. no. 023110.
- [9] D. Wei *et al.*, "Laser direct synthesis of graphene on quartz," *Carbon*, vol. 53, pp. 374-379, Mar 2013.
- [10] A.-S. Al-Sherbini, M. Bakr, I. Ghoneim, and M. Saad, "Exfoliation of graphene sheets via high energy wet milling of graphite in 2-ethylhexanol and kerosene," *Journal of Advanced Research*, vol. 8, no. 3, pp. 209-215, 2017/05/01/ 2017.
- [11] H. Kabir *et al.*, "The sp²-sp³ carbon hybridization content of nanocrystalline graphite from pyrolyzed vegetable oil, comparison of electrochemistry and physical properties with other carbon forms and allotropes," *Carbon*, vol. 144, pp. 831-840, 2019/04/01/ 2019.
- [12] A. Y. Vorobyev and C. Guoa, "Colorizing metals with femtosecond laser pulses," *Applied Physics Letters*, vol. 92, no. 4, Jan 28 2008, Art. no. 041914.
- [13] A. Y. Vorobyev and C. Guo, "Femtosecond laser blackening of platinum," (in English), *Journal of Applied Physics*, Article vol. 104, no. 5, p. 4, Sep 2008, Art. no. 053516.
- [14] B. Dusser *et al.*, "Controlled nanostructures formation by ultra fast laser pulses for color marking," (in English), *Optics Express*, Article vol. 18, no. 3, pp. 2913-2924, Feb 2010.
- [15] M. S. Ahsan, F. Ahmed, Y. G. Kim, M. S. Lee, and M. B. G. Jun, "Colorizing stainless steel

- surface by femtosecond laser induced micro/nano-structures," (in English), *Applied Surface Science*, Article vol. 257, no. 17, pp. 7771-7777, Jun 2011.
- [16] V. P. Korolkov *et al.*, "Surface nanostructuring of Ni/Cu foils by femtosecond laser pulses," (in English), *Quantum Electronics*, Article vol. 41, no. 4, pp. 387-392, 2011.
- [17] C. Z. Yao *et al.*, "Polarization and fluence effects in femtosecond laser induced micro/nano structures on stainless steel with antireflection property," (in English), *Applied Surface Science*, Article vol. 425, pp. 1118-1124, Dec 2017.
- [18] A. A. Ionin *et al.*, "Femtosecond laser color marking of metal and semiconductor surfaces," (in English), *Applied Physics a-Materials Science & Processing*, Article vol. 107, no. 2, pp. 301-305, May 2012.
- [19] G. Q. Li *et al.*, "Evolution of aluminum surface irradiated by femtosecond laser pulses with different pulse overlaps," (in English), *Applied Surface Science*, Article vol. 276, pp. 203-209, Jul 2013.
- [20] Z. Ou, M. Huang, and F. Zhao, "Colorizing pure copper surface by ultrafast laser-induced near-subwavelength ripples," *Optics Express*, vol. 22, no. 14, pp. 17254-17265, Jul 14 2014.
- [21] G. Li *et al.*, "Femtosecond laser color marking stainless steel surface with different wavelengths," *Applied Physics a-Materials Science & Processing*, vol. 118, no. 4, pp. 1189-1196, Mar 2015.
- [22] J. Long, P. Fan, M. Zhong, H. Zhang, Y. Xie, and C. Lin, "Superhydrophobic and colorful copper surfaces fabricated by picosecond laser induced periodic nanostructures," *Applied Surface Science*, vol. 311, pp. 461-467, Aug 30 2014.
- [23] P. Calvani *et al.*, "Optical properties of femtosecond laser-treated diamond," (in English), *Applied Physics a-Materials Science & Processing*, Article vol. 117, no. 1, pp. 25-29, Oct 2014.
- [24] E. Granados, M. Martinez-Calderon, M. Gomez, A. Rodriguez, and S. M. Olaizola, "Photonic structures in diamond based on femtosecond UV laser induced periodic surface structuring (LIPSS)," (in English), *Optics Express*, Article vol. 25, no. 13, pp. 15330-15335, Jun 2017.
- [25] S. Hohm, M. Herzlieb, A. Rosenfeld, J. Kruger, and J. Bonse, "Laser-induced periodic surface structures on fused silica upon cross-polarized two-color double-fs-pulse irradiation," (in English), *Applied Surface Science*, Article; Proceedings Paper vol. 336, pp. 39-42, May 2015.
- [26] X. L. He, A. Datta, W. Nam, L. M. Traverso, and X. F. Xu, "Sub-Diffraction Limited Writing based on Laser Induced Periodic Surface Structures (LIPSS)," (in English), *Scientific Reports*, Article vol. 6, p. 8, Oct 2016, Art. no. 35035.
- [27] A. K. Geim and K. S. Novoselov, "The rise of graphene," *Nature Materials*, vol. 6, no. 3, pp. 183-191, 2007/03/01 2007.
- [28] K. S. Novoselov *et al.*, "Electric Field Effect in Atomically Thin Carbon Films," *Science*, vol.

- 306, no. 5696, p. 666, 2004.
- [29] C. Lee, X. Wei, J. W. Kysar, and J. Hone, "Measurement of the Elastic Properties and Intrinsic Strength of Monolayer Graphene," *Science*, vol. 321, no. 5887, p. 385, 2008.
- [30] R. R. Nair *et al.*, "Fine structure constant defines visual transparency of graphene," *Science*, vol. 320, no. 5881, pp. 1308-1308, Jun 6 2008.
- [31] S. Bae *et al.*, "Roll-to-roll production of 30-inch graphene films for transparent electrodes," *Nature Nanotechnology*, vol. 5, no. 8, pp. 574-578, Aug 2010.
- [32] G. Eda, G. Fanchini, and M. Chhowalla, "Large-area ultrathin films of reduced graphene oxide as a transparent and flexible electronic material," *Nature Nanotechnology*, vol. 3, no. 5, pp. 270-274, May 2008.
- [33] X. Wang, L. Zhi, and K. Muellen, "Transparent, conductive graphene electrodes for dye-sensitized solar cells," *Nano Letters*, vol. 8, no. 1, pp. 323-327, Jan 2008.
- [34] X. Li *et al.*, "Large-Area Synthesis of High-Quality and Uniform Graphene Films on Copper Foils," *Science*, vol. 324, no. 5932, pp. 1312-1314, Jun 5 2009.
- [35] K. S. Kim *et al.*, "Large-scale pattern growth of graphene films for stretchable transparent electrodes," *Nature*, vol. 457, no. 7230, pp. 706-710, Feb 5 2009.
- [36] W. Cai, Y. Zhu, X. Li, R. D. Piner, and R. S. Ruoff, "Large area few-layer graphene/graphite films as transparent thin conducting electrodes," *Applied Physics Letters*, vol. 95, no. 12, Sep 21 2009, Art. no. 123115.
- [37] H. Yu *et al.*, "Large Energy Pulse Generation Modulated by Graphene Epitaxially Grown on Silicon Carbide," *Acs Nano*, vol. 4, no. 12, pp. 7582-7586, Dec 2010.
- [38] J. B. Park *et al.*, "Transparent interconnections formed by rapid single-step fabrication of graphene patterns," *Applied Physics Letters*, vol. 99, no. 5, Aug 1 2011, Art. no. 053103.
- [39] J. Lin *et al.*, "Laser-induced porous graphene films from commercial polymers," *Nature Communications*, vol. 5, Dec 2014.
- [40] M. A. Pimenta, G. Dresselhaus, M. S. Dresselhaus, L. G. Cancado, A. Jorio, and R. Saito, "Studying disorder in graphite-based systems by Raman spectroscopy," *Physical Chemistry Chemical Physics*, vol. 9, no. 11, pp. 1276-1291, 2007 2007.
- [41] A. C. Ferrari *et al.*, "Raman spectrum of graphene and graphene layers," *Physical Review Letters*, vol. 97, no. 18, Nov 3 2006, Art. no. 187401.
- [42] J. Kim and H. Ki, "Scaling law for penetration depth in laser welding," *Journal of Materials Processing Technology*, vol. 214, no. 12, pp. 2908-2914, Dec 2014.
- [43] L. G. Cancado *et al.*, "General equation for the determination of the crystallite size L-a of nanographite by Raman spectroscopy," *Applied Physics Letters*, vol. 88, no. 16, Apr 17 2006, Art. no. 163106.

- [44] D. Choi *et al.*, "Unusually High Optical Transparency in Hexagonal Nanopatterned Graphene with Enhanced Conductivity by Chemical Doping," *Small*, vol. 11, no. 26, pp. 3143-3152, Jul 8 2015.
- [45] K. K. Kim *et al.*, "Enhancing the conductivity of transparent graphene films via doping," *Nanotechnology*, vol. 21, no. 28, p. 285205, 2010/06/28 2010.
- [46] F. Gunes *et al.*, "Layer-by-Layer Doping of Few-Layer Graphene Film," *Acs Nano*, vol. 4, no. 8, pp. 4595-4600, Aug 2010.
- [47] Y. Zhu, Z. Sun, Z. Yan, Z. Jin, and J. M. Tour, "Rational Design of Hybrid Graphene Films for High-Performance Transparent Electrodes," *Acs Nano*, vol. 5, no. 8, pp. 6472-6479, Aug 2011.
- [48] M.-S. Lee *et al.*, "High-Performance, Transparent, and Stretchable Electrodes Using Graphene-Metal Nanowire Hybrid Structures," *Nano Letters*, vol. 13, no. 6, pp. 2814-2821, Jun 2013.
- [49] C. Li *et al.*, "Graphene Nano-"patches" on a Carbon Nanotube Network for Highly Transparent/Conductive Thin Film Applications," *Journal of Physical Chemistry C*, vol. 114, no. 33, pp. 14008-14012, Aug 26 2010.
- [50] A. L. Gorkina *et al.*, "Transparent and conductive hybrid graphene/carbon nanotube films," *Carbon*, vol. 100, pp. 501-507, Apr 2016.
- [51] D. Voiry *et al.*, "High-quality graphene via microwave reduction of solution-exfoliated graphene oxide," *Science*, vol. 353, no. 6306, pp. 1413-1416, Sep 23 2016.
- [52] A. Richter, H. J. Scheibe, W. Pompe, K. W. Brzezinka, and I. Muhling, "ABOUT THE STRUCTURE AND BONDING OF LASER GENERATED CARBON-FILMS BY RAMAN AND ELECTRON-ENERGY LOSS SPECTROSCOPY," *Journal of Non-Crystalline Solids*, vol. 88, no. 1, pp. 131-144, Nov 1986.
- [53] S. De and J. N. Coleman, "Are There Fundamental Limitations on the Sheet Resistance and Transmittance of Thin Graphene Films?," *Acs Nano*, vol. 4, no. 5, pp. 2713-2720, May 2010.
- [54] S. Chattopadhyay, Y. F. Huang, Y. J. Jen, A. Ganguly, K. H. Chen, and L. C. Chen, "Anti-reflecting and photonic nanostructures," (in English), *Materials Science & Engineering R-Reports*, Review vol. 69, no. 1-3, pp. 1-35, Jun 2010.
- [55] C. David, P. Haberling, M. Schnieper, J. Sochtig, and C. Aschokke, "Nano-structured anti-reflective surfaces replicated by hot embossing," (in English), *Microelectronic Engineering*, Article; Proceedings Paper vol. 61-2, pp. 435-440, Jul 2002, Art. no. Pii s0167-9317(02)00425-2.
- [56] Y. Kanamori, E. Roy, and Y. Chen, "Antireflection sub-wavelength gratings fabricated by spin-coating replication," (in English), *Microelectronic Engineering*, Article; Proceedings Paper vol. 78-79, pp. 287-293, Mar 2005.
- [57] Y. Kanamori, M. Sasaki, and K. Hane, "Broadband antireflection gratings fabricated upon

- silicon substrates," (in English), *Optics Letters*, Article vol. 24, no. 20, pp. 1422-1424, Oct 1999.
- [58] T. Jwad, S. A. Deng, H. Butt, and S. DimovSchool, "Laser induced single spot oxidation of titanium," (in English), *Applied Surface Science*, Article vol. 387, pp. 617-624, Nov 2016.
- [59] V. Veiko *et al.*, "Metal surface coloration by oxide periodic structures formed with nanosecond laser pulses," (in English), *Optics and Lasers in Engineering*, Article vol. 96, pp. 63-67, Sep 2017.
- [60] D. Zhang and K. Sugioka, "Hierarchical microstructures with high spatial frequency laser induced periodic surface structures possessing different orientations created by femtosecond laser ablation of silicon in liquids," *Opto-Electronic Advances*, vol. 2, no. 3, p. 190002, 2019.
- [61] R. Buividas, M. Mikutis, and S. Juodkazis, "Surface and bulk structuring of materials by ripples with long and short laser pulses: Recent advances," *Progress in Quantum Electronics*, vol. 38, no. 3, pp. 119-156, May 2014.
- [62] J. C. Wang and C. L. Guo, "Ultrafast dynamics of femtosecond laser-induced periodic surface pattern formation on metals," *Applied Physics Letters*, vol. 87, no. 25, Dec 19 2005, Art. no. 251914.
- [63] A. Borowiec and H. K. Haugen, "Subwavelength ripple formation on the surfaces of compound semiconductors irradiated with femtosecond laser pulses," *Applied Physics Letters*, vol. 82, no. 25, pp. 4462-4464, 2003.
- [64] S. Hohm, A. Rosenfeld, J. Kruger, and J. Bonse, "Femtosecond laser-induced periodic surface structures on silica," (in English), *Journal of Applied Physics*, Article vol. 112, no. 1, p. 9, Jul 2012, Art. no. 014901.
- [65] J. Y. Long, P. X. Fan, M. L. Zhong, H. J. Zhang, Y. D. Xie, and C. Lin, "Superhydrophobic and colorful copper surfaces fabricated by picosecond laser induced periodic nanostructures," (in English), *Applied Surface Science*, Article vol. 311, pp. 461-467, Aug 2014.
- [66] G. Li *et al.*, "Evolution of aluminum surface irradiated by femtosecond laser pulses with different pulse overlaps," *Applied Surface Science*, vol. 276, pp. 203-209, Jul 1 2013.
- [67] J. W. Yao *et al.*, "Selective appearance of several laser-induced periodic surface structure patterns on a metal surface using structural colors produced by femtosecond laser pulses," (in English), *Applied Surface Science*, Article vol. 258, no. 19, pp. 7625-7632, Jul 2012.
- [68] Z. G. Ou, M. Huang, and F. L. Zhao, "Colorizing pure copper surface by ultrafast laser-induced near-subwavelength ripples," (in English), *Optics Express*, Article vol. 22, no. 14, pp. 17254-17265, Jul 2014.
- [69] H. Iwase, S. Kokubo, S. Juodkazis, and H. Misawa, "Suppression of ripples on ablated Ni surface via a polarization grating," (in English), *Optics Express*, Article vol. 17, no. 6, pp. 4388-4396, Mar 2009.

- [70] G. Q. Li *et al.*, "Femtosecond laser color marking stainless steel surface with different wavelengths," (in English), *Applied Physics a-Materials Science & Processing*, Article vol. 118, no. 4, pp. 1189-1196, Mar 2015.
- [71] M. Oron and G. Sorensen, "NEW EXPERIMENTAL-EVIDENCE OF THE PERIODIC SURFACE-STRUCTURE IN LASER ANNEALING," *Applied Physics Letters*, vol. 35, no. 10, pp. 782-784, 1979 1979.
- [72] I. Horn and D. Gunther, "The influence of ablation carrier gasses Ar, He and Ne on the particle size distribution and transport efficiencies of laser ablation-induced aerosols: implications for LA-ICP-MS," (in English), *Applied Surface Science*, Article vol. 207, no. 1-4, pp. 144-157, Feb 2003, Art. no. Pii s0169-4332(02)01324-7.
- [73] J. Koch, S. Schlamp, T. Rosgen, D. Fliegel, and D. Gunther, "Visualization of aerosol particles generated by near infrared nano- and femtosecond laser ablation," (in English), *Spectrochimica Acta Part B-Atomic Spectroscopy*, Article vol. 62, no. 1, pp. 20-29, Jan 2007.
- [74] T. Yamashita and P. Hayes, "Analysis of XPS spectra of Fe²⁺ and Fe³⁺ ions in oxide materials," (in English), *Applied Surface Science*, Article vol. 254, no. 8, pp. 2441-2449, Feb 2008.
- [75] A. P. Grosvenor, B. A. Kobe, M. C. Biesinger, and N. S. McIntyre, "Investigation of multiplet splitting of Fe 2p XPS spectra and bonding in iron compounds," (in English), *Surface and Interface Analysis*, Article vol. 36, no. 12, pp. 1564-1574, Dec 2004.
- [76] L. Wang *et al.*, "Plasmonic nano-printing: large-area nanoscale energy deposition for efficient surface texturing," *Light: Science & Applications*, vol. 6, no. 12, pp. e17112-e17112, 2017/12/01 2017.
- [77] R. A. Kerr, "The Coming Copper Peak," *Science*, vol. 343, no. 6172, p. 722, 2014.
- [78] Y. T. You and J. W. Kim, "Fiber Laser Welding Properties of Copper Materials for Secondary Batteries," *Materials Science-Medziagotyra*, vol. 23, no. 4, pp. 398-403, 2017.
- [79] J. Ning, L. J. Zhang, X. Q. Yin, J. X. Zhang, and S. J. Na, "Mechanism study on the effects of power modulation on energy coupling efficiency in infrared laser welding of highly-reflective materials," (in English), *Materials & Design*, Article vol. 178, p. 16, Sep 2019, Art. no. 107871.
- [80] A. Heider, P. Stritt, A. Hess, R. Weber, and T. Graf, "Process Stabilization at welding Copper by Laser Power Modulation," *Physics Procedia*, vol. 12, pp. 81-87, 2011/01/01/ 2011.
- [81] P. Heinen, A. Haeusler, B. Mehlmann, and A. Olowinsky, "Laser Beam Microwelding of Lithium-ion Battery Cells with Copper Connectors for Electrical Connections in Energy Storage Devices," (in English), *Lasers in Engineering*, Article vol. 36, no. 1-3, pp. 147-167, 2017.
- [82] S. Engler, R. Ramsayer, and R. Poprawe, "Process Studies on Laser Welding of Copper with Brilliant Green and Infrared Lasers," *Physics Procedia*, vol. 12, pp. 339-346, 2011/01/01/ 2011.

- [83] H. C. Chen, G. J. Bi, M. L. S. Nai, and J. Wei, "Enhanced welding efficiency in laser welding of highly reflective pure copper," (in English), *Journal of Materials Processing Technology*, Article vol. 216, pp. 287-293, Feb 2015.
- [84] S. Kaierle, L. Overmeyer, C. Hoff, P. Herzog, and J. Hermsdorf, "Conditioning of copper material surfaces increasing the efficiency of continuous wave laser microwelding," (in English), *Cirp Journal of Manufacturing Science and Technology*, Article vol. 14, pp. 66-70, Aug 2016.
- [85] E. Biro, D. C. Weckman, and Y. Zhou, "Pulsed Nd:YAG laser welding of copper using oxygenated assist gases," *Metallurgical and Materials Transactions A*, vol. 33, no. 7, pp. 2019-2030, 2002/07/01 2002.
- [86] G. Daurelio and G. Giorleo, "EXPERIMENTAL TECHNIQUES TO CUT AND WELD COPPER BY LASER - A REVIEW," *Materials and Manufacturing Processes*, vol. 6, no. 4, pp. 577-603, 1991/01/01 1991.
- [87] A. Heider, J. Sollinger, F. Abt, M. Boley, R. Weber, and T. Graf, "High-Speed X-Ray Analysis of Spatter Formation in Laser Welding of Copper," *Physics Procedia*, vol. 41, pp. 112-118, 2013/01/01/ 2013.
- [88] L.-J. Zhang, G.-F. Zhang, J. Ning, X.-J. Zhang, and J.-X. Zhang, "Microstructure and properties of the laser butt welded 1.5-mm thick T2 copper joint achieved at high welding speed," *Materials & Design*, vol. 88, pp. 720-736, 2015/12/25/ 2015.

ACKNOWLEDGEMENTS

First, I would like to express my deepest thanks to my advisor, Professor Hyungson Ki. He was a very good mentor. His generous advice and research guidance helped me complete my doctoral program. And he gave me many good words about my life, which helped me a lot outside of research.

Besides my advisor, I would like to thank the rest of the committees, Professor Heungjoo Shin, Professor Jaesung Jang, Professor Jaeson Lee, and Dr. Jun Choi. They listened carefully to my research and helped me improve my doctoral thesis with a lot of advice.

I would also like to thank Laser Processing and Multiphysics System Laboratory members. They were very pleasant and helped me to study in a good mood. Since I was with them, I think I was able to finish my PhD. In particular, I would like to thank members who are currently in graduate school : Chun Deng, Haram Yeo, Sehyeok Oh, Hyeongwon Kim, Hyung Kook Jin and Myeong Gyun Son. I also thank our former members who previously graduated : Hongrae Cho, Yoo Jai Won, Sanseo Kim, Sangwoo So and Jaehun Kim.

Lastly, I would like to thank my family. Through long periods of continuous encouragement, I was able to finish the doctoral program. Every hard moment, I could overcome with the love of my parents. I am grateful for the support of my father, the care of my lovely mother and my cute little sister.

